Structural Health Assessment through Vibration Monitoring on FPSOs

Konstantinos Tatsis

Structural Health Assessment through Vibration Monitoring on FPSOs

by

Konstantinos Tatsis

to obtain the degree of Master of Science (MSc)
at the Delft University of Technology,
to be defended publicly on Tuesday August 30, 2016 at 11:00 AM.

Student number:	4422317	
Thesis committee:	Prof. dr. A. V. Metrikine	TU Delft
	Dr. E. Lourens	TU Delft
	Ir. R. Hageman	MARIN
	Prof. dr. ir. M. L. Kaminski	TU Delft

An electronic version of this thesis is available at: http://repository.tudelft.nl/

Abstract

In offshore industry, gas and oil production takes place at more and more remote locations with Floating Production Storage Offloading units (FPSOs) being often selected for field development. These units may remain on station during their entire lifetime while operating under adverse weather conditions. Thus, inspections, which have to be performed on site, are becoming a challenging and risky operation. Within this context, various Structural Health Monitoring (SHM) schemes are being explored in an attempt to ensure integrity of floating offshore units.

The goal of this project is to study the feasibility of structural health assessment on FPSOs using vibration-based monitoring techniques with the ultimate aim to minimize inspections of confined spaces. To this end, a typical panel structure on an FPSO hull is considered and modelled using the Finite Element (FE) method. As part of a ballast tank, the considered stiffened panel is inevitably subject to structural degradation, with corrosion and fatigue cracks constituting the main mechanisms among others. The constructed FE model is therefore appropriately parametrized in order to accommodate the simulation of the aforementioned damage conditions.

The first part of this study, referred to as the forward problem, consists in modelling the dominant degradation mechanisms experienced by hull structures of FPSOs, namely uniform corrosion, pitting corrosion and fatigue cracks. These are introduced with varying degree of deterioration into the reference FE model of the said stiffened panel and the sensitivity of vibrational characteristics, i.e. natural frequencies, mode shapes and damping ratios, to these changes is investigated. The aim of this part is to extract the identifiable damage scenarios that will serve as the basis for the structural health assessment through the implementation of Operational Modal Analysis (OMA).

In the second part of the study, the so-called inverse process, the stiffened panel is assumed to be monitored during normal operation using a conventional monitoring system (i.e. accelerometers). The latter is configured in such a way that observability of all modes is accomplished and robustness of the identified properties is ensured. Excitation of the structure is assumed to be sloshing-induced impulsive loads and the measured noisy signals are processed with a set of Stochastic Subspace Identification (SSI) algorithms, upon enhancement with a cluster analysis in order to enable automatic system identification. For each one of the damage scenarios, the dynamic properties are identified and cross-compared with those of the reference model. The feasibility of damage detection through vibration monitoring, along with the existing restrictions, is finally determined and a possible extension of the proposed formulation is discussed.

Contents

List of Figures

List of Tables

List of Acronyms

AE	Acoustic Emissions
AHMS	Advisory Hull Monitoring System
DNV	Det Norske Veritas
DOP	Degree of Pitting
EMA	Experimental Modal Analysis
FDD	Frequency Domain Decomposition
FDS	Fatigue Damage Sensor
FE	Finite Element
FPSO	Floating Production Storage Offloading unit
GPS	Global Positioning System
HRMS	Hull Response Monitoring System
IMO	International Maritime Organization
JIP	Joint Industry Project
LBSG	Long-Based Strain Gauges
LNG	Liquefied Natural Gas
LS	Least Squares
MAC	Modal Assurance Criterion
MonitAS	Monitoring Advisory System
OMA	Operational Modal Analysis
PP	Peak Picking
SHM	Structural Health Monitoring
SSI	Stochastic Subspace Identification
SSI-Cov	Covariance-driven Stochastic Subspace Identification
SSI-Data	Data-driven Stochastic Subspace Identification
SVD	Singular Value Decomposition

Nomenclature

$(\bullet)^{\dagger}$	Moore-Penrose pseudo-inverse operator
H, W	Height and width of ballast tank
$\mathrm{N}_i^{\mathrm{e}}$	Element shape function of node i
Δ	Delay operator
Δt	Time step
β, γ	Parameters of Newmark method
δ	Noise level
δ_{pq}	Kronecker delta
δt	Duration of sloshing-induced impact load
$\hat{\mathbf{Z}}_i$	Kalman filter state sequence
$\hat{\boldsymbol{\zeta}}_k^-$, $\hat{\boldsymbol{\zeta}}_k$	*A priori* and *a posteriori* estimates of the modal state vector
λ_k	Eigenvalues of the discrete-time system matrix $\mathbf{A}$
λ_{ck}	Eigenvector of the continuous-time system matrix $\mathbf{A}_{\mathrm{c}}$
$(\bullet)^{\mathrm{H}}$	Hermitian transpose operator
$\mathbb{E}[\bullet]$	Expected value operator
$\mathbb{R}^{\mathrm{m}\times\mathrm{n}}$	Vector space of m × n dimensional real matrices
$\mathbb{R}^{\mathrm{m}}$	Vector space of m-dimensional real vectors
$\mathscr{P}_i$	Projection of the future outputs $\mathbf{Y}_{\mathrm{f}}$ into the row space of the past outputs $\mathbf{Y}_{\mathrm{p}}$
$\mathscr{P}_{i-1}$	Projection of the shifted future outputs $\mathbf{Y}_{\mathrm{f}}^-$ into the row space of the past outputs $\mathbf{Y}_{\mathrm{p}}^+$
$\mathrm{Re}(\bullet)$	Real part operator
A, B, G, J	State-space matrices in discrete-time domain
$\mathbf{A}_{\mathrm{c}}$, $\mathbf{B}_{\mathrm{c}}$, $\mathbf{G}_{\mathrm{c}}$, $\mathbf{J}_{\mathrm{c}}$	State-space matrices in continuous-time domain
$\mathbf{B}^{\mathrm{e}}$	Element deformation matrix
$\mathbf{C}^{\mathrm{r}}$, **O**	Extended observability and reversed extended controllability matrices
$\mathbf{C}_{\mathrm{mm}}$, $\mathbf{C}_{\mathrm{ss}}$	Submatrices of the damping matrix $\mathbf{C}$
D	Partial derivative operator
E	Material constitutive matrix

$\mathbf{F}$	State-output covariance matrix
$\mathbf{I}$	Identity matrix
$\mathbf{J}_{\mathrm{N}}$	Jacobian matrix
$\mathbf{K}^{\mathrm{e}}, \mathbf{M}^{\mathrm{e}}$	Element stiffness and mass matrices
$\mathbf{K}_k$	Kalman gain at time instant k
$\mathbf{K}_{\mathrm{mm}}, \mathbf{K}_{\mathrm{ss}}$	Submatrices of stiffness matrix $\mathbf{K}$
$\mathbf{L}_{1\|i}$	Block Toeplitz matrix of output covariances
$\mathbf{MAC}_{k,k+1}$	Modal Assurance Criterion between mode shape vectors k and $k+1$
$\mathbf{M}, \mathbf{C}, \mathbf{K}$	Mass, damping and stiffness matrices
$\mathbf{M}_{\mathrm{c}}, \mathbf{C}_{\mathrm{c}}, \mathbf{K}_{\mathrm{c}}$	Reduced mass, damping and stiffness matrices
$\mathbf{M}_{\mathrm{mm}}, \mathbf{M}_{\mathrm{ss}}$	Submatrices of the mass matrix $\mathbf{M}$
$\mathbf{N}^{\mathrm{e}}$	Shape function matrix
$\mathbf{P}_k^-, \mathbf{P}_k$	*A priori* and *a posteriori* error covariance estimates at time instant k
$\mathbf{Q}, \mathbf{R}, \mathbf{S}$	Covariance matrices of measurement and process noise
$\mathbf{R}_{\mathrm{c}}$	Condensation matrix for Guyan reduction
$\mathbf{S}_{\mathrm{d}}, \mathbf{S}_{\mathrm{v}}, \mathbf{S}_{\mathrm{a}}$	Displacement, velocity and acceleration selection matrices
$\mathbf{S}_{\mathrm{p}}, \mathbf{S}_{\mathrm{y}}$	Input and output selection matrices
$\mathbf{T}_{\mathrm{c}}$	Transformation matrix for Guyan reduction
$\mathbf{U}, \mathbf{S}, \mathbf{V}$	Matrices of singular value decomposition
$\mathbf{U}_1, \mathbf{S}_1, \mathbf{V}_1$	Submatrices of singular value decomposition corresponding to non-zero singular values
$\mathbf{Y}_{0\|2i-1}$	Output block Hankel matrix
$\mathbf{Y}_{0\|i-1}, \mathbf{Y}_{i\|2i-1}$	Past and future submatrices of the block Hankel matrix $\mathbf{Y}_{0\|2i-1}$
$\mathbf{Y}_{0\|i}, \mathbf{Y}_{i+1\|2i-1}$	Shifted past and future submatrices of the block Hankel matrix $\mathbf{Y}_{0\|2i-1}$
$\mathbf{Y}_{\mathrm{p}}, \mathbf{Y}_{\mathrm{f}}$	Past and future submatrices of the block Hankel matrix $\mathbf{Y}_{0\|2i-1}$
$\mathbf{Y}_{\mathrm{p}}^+, \mathbf{Y}_{\mathrm{f}}^-$	Shifted past and future submatrices of the block Hankel matrix $\mathbf{Y}_{0\|2i-1}$
$\mathbf{c}_1, \mathbf{c}_2, \mathbf{c}_3$	Coefficient matrices of Newmark method
$\mathbf{e}_k^-, \mathbf{e}_k$	*A priori* and *a posteriori* error estimates at time instant k
$\mathbf{f}(t)$	Continuous-time nodal force vector
$\mathbf{f}_{\mathrm{c}}(t)$	Reduced nodal force vector
$\mathbf{f}_{\mathrm{m}}(t), \mathbf{f}_{\mathrm{s}}(t)$	Partitions of the continuous-time nodal force vector $\mathbf{f}(t)$
$\mathbf{p}(t)$	Continuous-time input vector
$\mathbf{p}_k$	Discrete-time input vector at time instant k
$\mathbf{r}_k$	Vector of random values from the standard normal distribution
$\mathbf{u}(t), \dot{\mathbf{u}}(t), \ddot{\mathbf{u}}(t)$	Continuous-time displacement, velocity and acceleration vectors
$\mathbf{u}^{\mathrm{e}}$	Element nodal displacement vector
$\mathbf{u}_k, \dot{\mathbf{u}}_k, \ddot{\mathbf{u}}_k$	Discrete-time displacement, velocity and acceleration vectors

$\mathbf{w}_k, \mathbf{v}_k$	Process and output noise vectors at time instant k
$\mathbf{x}_k$	Full-order state vector at time instant k
$\mathbf{y}_k, \hat{\mathbf{y}}_k$	Actual measurement and measurement prediction vectors at time instant k
$\mathbf{z}(t), \dot{\mathbf{z}}(t), \ddot{\mathbf{z}}(t)$	Continuous-time modal displacement, velocity and acceleration vectors
$\mathbf{z}_k, \dot{\mathbf{z}}_k, \ddot{\mathbf{z}}_k$	Discrete-time modal displacement, velocity and acceleration vectors
$\mathbf{\Gamma}, \mathbf{\Omega}$	Modal damping and stiffness matrices
$\mathbf{\Lambda}_l$	Output covariance matrix for time lag $l\Delta t$
$\mathbf{\Phi}$	Modal matrix
$\mathbf{\Sigma}$	State covariance matrix
$\boldsymbol{\epsilon}$	Strain vector
$\boldsymbol{\phi}_k$	Mode shape vector of mode k
$\boldsymbol{\phi}_\mathrm{m}, \boldsymbol{\phi}_\mathrm{s}$	Partitions of the mode shape vector
$\boldsymbol{\psi}_k$	Eigenvector of the discrete-time system matrix $\mathbf{A}$
$\boldsymbol{\psi}_{ck}$	Eigenvector of the continuous-time system matrix $\mathbf{A}_\mathrm{c}$
$\boldsymbol{\sigma}_\mathrm{y}$	Standard deviation matrix of output measurements
$\boldsymbol{\zeta}_k$	Modal state vector at time instant k
ω_k	Eigenfrequency of mode k
$\omega_{fn}, \mathrm{T}_{fn}$	Fluid-free-surface natural frequency and natural period
$\overline{\mathbf{O}}, \underline{\mathbf{O}}$	Up-shifted and down-shifted extended observability matrices
ρ	Material density
ρ_w	Water density
$\tilde{\mathbf{Q}}, \tilde{\mathbf{R}}$	Matrices of QR-factorisation
$\tilde{\mathbf{y}}_k$	Noisy output vector at time instant k
d_{jk}	Proximity criterion between modes j and k
$f_k, \hat{f}_k, \xi_k$	Frequency, frequency estimate and damping ratio of mode k
h	Fill height of ballast tank
i, j	Number of block rows and columns of the block Hankel matrix $\mathbf{Y}_{0\|2i-1}$
n_dof	Number of degrees of freedom
$n_\mathrm{d}, n_\mathrm{v}, n_\mathrm{a}$	Number of displacement, velocity and acceleration outputs
n_m	Number of modes
$n_\mathrm{p}, n_\mathrm{y}$	Number of input forces and output measurements
$n_\mathrm{r}, n_\mathrm{c}$	Number of master and slave degrees of freedom
n_s	Number of states of state-space model
p, q, r	Element natural coordinates
p_w	Water pressure
s	Number of available measurements
u, v, w	Nodal displacements in x, y and z axes
w_i	Integration weight of the Gauss quadrature rule

1 Introduction

Structural integrity is a major factor in assets management of offshore and ship structures, as well as land-based structural systems such as pipelines. Present-day approaches for integrity assessment require implementation of quantitative techniques which are subject to major uncertainties, stemming from their input elements - the loads acting on the structure and the resistance parameters.

In marine structures, the loads principally include wave-induced forces, as a function of the sea-state, wind-induced forces and forces due to ship motion. These may be imposed globally, resulting in hull girder bending, or locally, such as those acting at the side and bottom panels, introducing an inevitable degree of uncertainty in the structure due to their stochastic nature. However, the key element in order to ensure structural integrity is the set of variables describing the resistance of the structure to the imposed loading. Being typically random variables, they change with time due to deterioration, rendering therefore the strength of the structure a time-dependent variable.

When dealing with ships in general, and Floating Production Storage Offloading unit (FPSO) units in particular, which constitute a common practice in oil and gas production at sea due to their storage capacity and simplicity of installation process, a set of typical degradation mechanisms pertains to ship collision, storm-induced slamming, ice impact, fire and blast, corrosion and fatigue fracture. These last two components are prominently associated with the strength of the structure and consequently with asset integrity. Additionally, considering that FPSOs operate at more and more remote locations and remain on station during their entire lifetime, inspections have to be performed on site and may often become challenging and potentially risky. In limiting this risk of maintenance intervention and ensuring safe operation, Structural Health Monitoring (SHM) is receiving growing attention, towards the identification of structural vibration characteristics and subsequently of degradation mechanisms. The main goals of a SHM strategy, as stated by Wang et al. (2014a), comprise:

- Evaluation of structural degradation and degrading conditions
- Verification of design assumptions referring to loads and responses
- Assessment of potential failures due to gross errors in the design, fabrication, and operation
- Assessment of operational response.

Within this context, it is of crucial importance that a SHM system is able to furnish reduced inspection costs, minimization of preventive maintenance and extension of structural life.

Figure 1.1: Bonga FPSO, Gulf of Guinea, Nigeria

Regarding FPSOs, and setting aside the accidental limit states such as ship collision and fire, a SHM system should aim at providing a robust monitoring strategy for the detection and diagnosis of the hull-related damage states which according to statistics are ranked the top causes leading to total vessel loss, as underlined by a ISSC (2009) report.

From this perspective, the present work constitutes an attempt to establish an identification scheme for the degradation mechanisms experienced by hull structures of FPSOs as well as the investigation of applicability of vibration-based analysis methods for SHM in the offshore industry. In order to set a solid basis for such an approach, the following lines are introducing an overall description of the problem at hand and provide an overview of the guidelines to be followed within the adopted working frame.

1.1 Classes of damage on FPSOs

The progressive deterioration of ship structures as a consequence of normal operation and environmental influences, may be assigned as the definition of structural aging. This deterioration may appear in various forms including coating damage, changes in material properties, corrosion and cracking with the last two being the most pervasive classes of damage.

1.1.1 Corrosion

Corrosion is defined as the deterioration process of a material due to chemical reactions with its environment. Depending on the surroundings, corrosion processes may refer to either chemical or electrochemical reactions, with the latter occurring in a large variety of natural electrolytes and industrial applications. A distinctive example of this is the rusting of steel due to exposure to water or humid air, leading to the formation of iron oxides and eventually the material damage.

As shown by empirical evidence and highlighted by a report of ISSC (2009), corrosion is one of the five causes of damage which may lead to the loss of ships, considering that right after commissioning ships are inevitably exposed to highly corrosive conditions. The corrosion process starts with thinning of the material, variations in its mechanical properties and finally a reduction in strength capacity. According to DNV (2013), in maritime engineering corrosion may be divided into four types:

General corrosion

The most common and harmless form of corrosion, wherein degradation is uniformly distributed on the exposed surface. Although it is called uniform, the corroded area exhibits a sort of waviness and roughness. It may cause by far the largest amount of material losses and is a common occurrence in many industrial applications. In maritime engineering, as underlined by Howarth (2011), such a type of corrosion is found under deck areas in cargo oil holds due to the presence of volatile gases from the crude oil, as well as in uncoated parts of bulk carriers, according to Gardiner and Melchers (2003).

Pitting corrosion

A form of localized corrosion characterized by the development of small cavities usually on openly exposed surfaces of a metal. The diameter of these cavities is of the same order of magnitude of the depth. Various shapes may however be observed depending on the environmental conditions and the metal or alloy. In marine structures and specifically in ships, pitting usually occurs as a result of the breakdown of protective coating (Nakai et al., 2004) or due to ineffective cathodic protection systems, with the bottom plating of cargo oil tanks and some horizontal surfaces in ballast tanks being the most likely places.

Grooving and edge corrosion

Grooving corrosion may be found in the base material where the coating has been scratched or the metal itself has been mechanically damaged. Damage due to grooving corrosion may also be accelerated due to lack of maintenance on the protective coating or the sacrificial anodes. In a ship structure, it is most likely that grooving corrosion appears at stiffener connections close to a weld (Wang et al., 2014c). On the other hand, in terms of the edges of structural members, geometrical complexities may lead to a thinner coating layer, making these areas more susceptible to corrosion. In this sense, edge corrosion is more likely to be found at the free end of stiffeners or around cut outs.

1.1.2 Fatigue

Apart from corrosion, fatigue cracking constitutes another substantial factor associated with structural degradation appearing in aging structures. Being a primary source of costly repair work, its development may render a structure marginal or even lead it to a failure state, since it can result in a significant reduction of ultimate strength under certain circumstances.

In the presence of repeated or cyclic loading, cracks due to fatigue are most likely to initiate in the regions of the structure subjected to stress concentrations. However, it is also conceivable that initial cracks or defects may be inserted in structures during the fabrication process, and remain undetectable throughout their lifetime. Crack propagation may also be caused not only under cyclic loading but in the presence of monotonically increasing loads as well. This event is of course usually mitigated by stress redistribution over the structure or due to material ductility and therefore it seldom appears.

Regarding marine structures, fatigue cracking may often be observed in a stiffened panel along the weld intersection between the plates and the stiffeners. These cracks may have a varying orientation, depending on the loading history, and can be classified into three types - vertical, horizontal and angular. Moreover, while in thick plated structures the crack depth may be small compared to the plate thickness, in relatively thin plates, as commonly used in ship structures, cracking usually appears as through-thickness cracks.

1.2 Monitoring techniques

The significance of monitoring and mitigating degradation has been recognized by several partners of the offshore industry among which ship owners, classification societies and International Maritime Organizations (IMOs). Regarding the aforementioned types of degradation problems experienced by ship structures, various monitoring approaches have been implemented within the framework of SHM strategies, both locally and globally. A common practice is the Hull Response Monitoring System (HRMS), which constitutes the state-of-the-art monitoring technique for ships, measuring and displaying ship motions and hull responses in key locations.

A HRMS is a global monitoring approach based on a series of sensors including strain gauges, namely Long-Based Strain Gauges (LBSG), temperature sensors and accelerometers, placed in certain locations on ships, as well as some additional devices such as Global Positioning System (GPS) and sensors for hydrostatic pressure and motion prediction. HRMSs provide real-time information on all relevant responses of the ship to the operator and operational guidance in case of severe weather conditions. A distinctive instance of such a monitoring framework, referred to as the Advisory Hull Monitoring System (AHMS), is the Monitoring Advisory System (MonitAS) developed as a part of the MonitAS Joint Industry Project (JIP), which will be introduced in the following sections.

Regarding local monitoring techniques, a wide range of them is available for monitoring of corrosion damage (Yang, 2008), including electrochemical polarization, galvanic sensors, multielectrode systems, radioactivity methods, electrical resistance techniques as well as Acoustic Emissions (AE). The latter is a widely applied identification method in many industrial fields and may be an appropriate solution for monitoring corrosion in onshore tanks. Its applicability on FPSOs is however subject to high noise disturbance due to the low level emissions (Boller et al., 2009).

Nevertheless, as highlighted by Boller et al. (2009), AE is a promising technique for crack detection, providing real-time information for crack initiation and propagation, and can be combined with strain gauges in order to yield the stress level correlation. Alternatively, Fatigue Damage Sensors (FDSs), referred to as fatigue gauges, are also commonly employed for fatigue crack-growth identification. These small sensors consist of thin metal pieces and are usually placed on structural areas with high stress-concentration factors. Their function is based on a crack propagating through the surface of the sensor whose length is proportional to the fatigue consumption of the structure, providing in this sense a quantitative assessment of lifetime consumption.

A more universal approach for damage assessment, which is mainly employed in civil and aerospace structures, is vibration-based monitoring. The basis of this approach is the

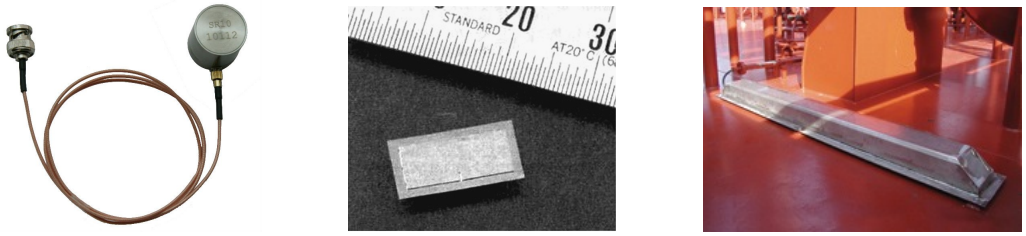

(a) AE sensor (b) FDS (c) LBSG

Figure 1.2: Typical monitoring sensors

investigation of changes in the dynamic characteristics of a system, such as natural frequencies, mode shapes and mode shape curvatures, reflected by the presence of damage. The method, which will be the subject of study in the present project, typically makes use of acceleration measurements or strain gauges and is supposed to be sufficiently accurate for the detection of a 0.5% change in natural frequencies (Wang et al., 2014b).

1.3 Current state of research

Various studies have been proposed for structural integrity assessment on FPSOs and offshore structures in general, examining different approaches and degradation mechanisms or damage states. A first family of these studies is concentrated on the simulation of damage states and the investigation of their influence on the structural response and the strength of the structure, while the second category comprises those studies dealing with monitoring strategies and processing of inspection data towards the identification of degradation mechanisms. In their turn, these categories may be classified into global approaches where integrity is assessed on the structure as an entity and local ones where special structural components are investigated under certain structural threats.

A review of the corrosion effect on structural strength capacity of stiffened panels may be found in Wang et al. (2014c), including predictions for corrosion development in marine conditions. Regarding the latter, a wide range of studies exists in the literature using statistical methods in combination with measurement data (Qin et al., 2015, Qin and Cui, 2003) and models based on physical principles. In terms of reliability analysis accounting for general and pitting corrosion, Melchers (2005) studied the effect of corrosion on the structural reliability of steel offshore structures whereas Yamamoto and Ikegami (1998) proposed a probabilistic approach for corrosion modelling on ship's hull. In a more general framework, Akpan et al. (2002) developed an approach for risk assessment of aged ship hull structures in the presence of both corrosion and fatigue.

A number of Finite Element (FE) analyses has also been performed in order to examine the sensitivity of strength capacity to corrosion (Dunbar et al., 2004, Huang et al., 2010, Silva et al., 2014). To this end, Wang et al. (2015b) carried out a sensitivity analysis on the ultimate strength of aged structures subjected to grooving corrosion while Sultana et al. (2015) investigated the influence of corrosion on the ultimate compressive strength of steel plates and stiffened panels.

Without considering fatigue crack growth and propagation processes, which pertain to fracture mechanics field and have been investigated in ship-structure applications by Okawa et al. (2006), crack effects on structural integrity have also been studied recently. Within this context, Wang et al. (2015a) focused on the influence of cracks on the structural behaviour through an investigation of the ultimate shear strength of intact and cracked stiffened panels. In a similar investigation, Paik et al. (2005) worked on an experimental and numerical study of the ultimate strength of cracked steel plates subjected to compression or tension. Accounting for varying size and location of cracks and implementing a series of non-linear FE analyses, they investigated the ultimate strength reduction characteristics of plate elements. In a more universal approach, Vafai and Estekanchi (1999) carried out a parametric FE study on the impact of cracks in the overall behaviour of plates and shells.

From a dynamic point of view, the problem of crack influence on structural behaviour is receiving growing attention as well, given the extensive literature existing thereupon. In an early study, Stahl and Keer (1972) developed and demonstrated a method for determining the dynamic properties, that is natural frequencies, of cracked rectangular plates. More recently,

Qian et al. (1991) focused on the vibrational behaviour of cracked plates using a FE model through the investigation of changes in eigenfrequencies for different crack lengths and Alinia et al. (2007) dealt with numerical modelling for buckling analysis of shear panels. In a more sophisticated approach, Tran et al. (2015) worked on the free vibration analysis of cracked Functionally Graded Material (FGM) using eXtended IsoGeometric Approach (XIGA) and high-order shear deformation theory.

In modal testing approaches by means of vibration monitoring, two main categories may be distinguished, namely Experimental Modal Analysis (EMA) and Operational Modal Analysis (OMA). In EMA, a structural model is excited in laboratory conditions by one or more measured forces and its modal parameters are then extracted from the measured structural response. A typical method within this framework is the Peak Picking (PP) method. Although, well-established and often-used method in mechanical engineering, it is not the appropriate one for large civil structures and structures that need be tested in operational rather than laboratory conditions. On the other hand, OMA, also known as output-only modal analysis, is an identification process that derives the modal information from structural response during operation.

There has been a large increase of research activity around OMA during the last years, with applications in a wide range of projects. Among others, the results served by OMA may be utilized for model updating of new structures, for tuning of vibration control devices, as well as for system identification as such. An overview of the OMA methods with discussions on the major developments and references to both time and frequency domain approaches is presented by Zhang et al. (2005). Although there exist a lot of recently-developed alternative algorithms for OMA, they are all based on a few basic principles. Among others, the ones with high accuracy in civil engineering applications are: the Frequency Domain Decomposition (FDD) (Brincker et al., 2001), the Stochastic Subspace Identification (SSI) algorithms (Van Overschee and De Moore, 1996) and the poly-Least Squares Complex Frequency (p-LSCF) (Magalhaes and Cunha, 2011). An explanation of these three methods is provided by Magalhaes and Cunha (2011) while a thorough study of OMA methods with reference to civil engineering structures is summarized by Peeters (2000).

1.4 The MonitAS project

Of particular interest among the studies towards a unified strategy for monitoring of structural degradation is the MonitAS JIP, which started in 2008 following a long term monitoring period on board FPSO *Glas Dowr*. The aim of this project was to develop an AHMS for FPSOs using *Glas Dowr* as a test bed, while it was operating offshore South Africa (Aalberts et al., 2010). In its turn, the AHMS was aiming to estimate the fatigue lifetime consumption by means of a blend of monitored quantities, including stress and wave measurements as well as information on loading conditions. Within this context, the system calculates the fatigue lifetime consumption rate and provides a comparison with the design calculations, indicating at the same time preventive actions for the achievement of reduced rates.

Aiming to provide insight on the uncertainties dominating the fatigue accumulation process (Hageman et al., 2013), the said AHMS is mainly based on three different methods. Making use of the fatigue design procedure, which generates the "predicted fatigue", in combination with measured environmental and operational conditions, the first method calculates the lifetime consumption of the structure, referred to as the "calculated fatigue". Implementation of a second method, referred to as the "measured fatigue", allows for the estimation of the lifetime consumption through processing of available strain measurements. The assessment

of lifetime consumption with the third method is performed using an analogue FDS.

A comparison of these three variables provided by the AHMS, indicates the reason why measured lifetime consumption may deviate from design predictions. This is achieved by following the design process upon substitution of the input parameters with the measured values in order to determine whether deviations from design values are due to environmental conditions, operational conditions or discrepancies between hydrodynamic or structural design processes and real phenomena. Following the first successful stage on FPSO *Glas Dowr*, the continuation of the project in 2010 aimed at installing a second monitoring system on a new-built FPSO, to be placed in the Gulf of Guinea. An overview of the latest phase of this project is supplied by Hostis et al. (2013).

1.5 Aims and scope

In an attempt to ensure safe operation and minimize inspections of confined spaces in FPSOs, the present project deals with the feasibility of structural health assessment on FPSOs using vibration-based monitoring techniques. Such a need stems from the fact that FPSOs are often selected for the development of marginal fields while operating under adverse weather conditions. Besides, the absence of dry-docking during their entire lifetime, renders inspections a challenging and potentially risky task. Within this context, a typical panel structure on an FPSO hull is addressed, and the viability of vibration-based techniques for damage identification through OMA is examined.

The main objectives of this project may be summarized in the following points:

- Modelling of the dominant degradation mechanisms experienced by hull structures of FPSOs.
- Development of a parametric numerical model for a typical stiffened panel on an FPSO hull, capable of accommodating a wide series of possible damage conditions.
- Investigation of the sensitivity of the vibrational characteristics of stiffened panels to varying degrees and types of damage.
- Study on the feasibility of damage detection through vibration monitoring using conventional monitoring systems (e.g., strain gauges, accelerometers).
- Proposal of a monitoring paradigm so that online function in a semi-continuous way is possible.

1.6 Outline

The present Chapter constitutes a brief introduction to the core concepts that will be discussed within the following pages. As a matter of structural integrity, a short description of the prevailing degradation mechanisms was first described along with an overview of the current monitoring approaches used in FPSOs. The review of the current state of research in this discipline was then followed by the presentation of the MonitAS project and finally the aims of the project were addressed. A short outline of the present thesis is schematically represented in Fig. 1.3.

Chapter 2 constitutes the basis for the numerical modelling of stiffened panels using the FE method. The numerical simulations carried out herein are all coded in Python environment and the mathematical formulations of the developed tools are presented. These

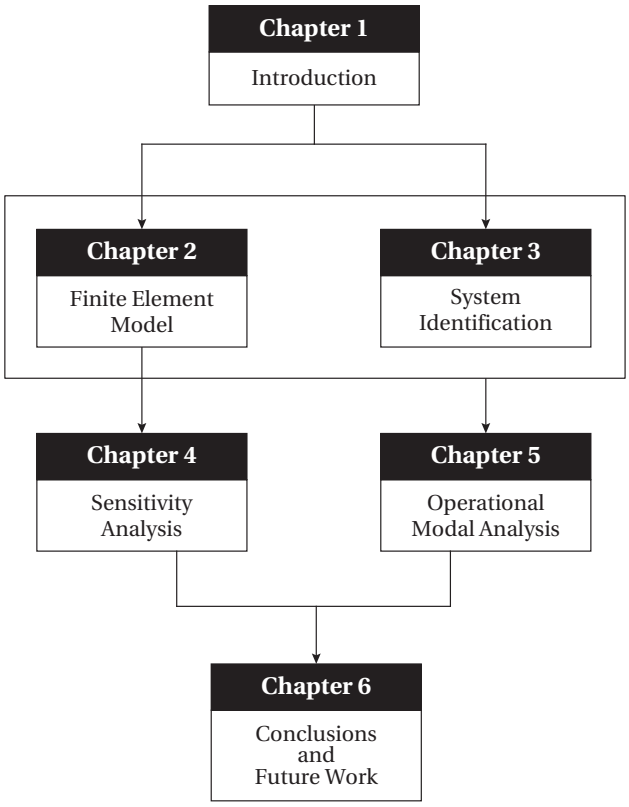

Figure 1.3: Outline of the project

may be divided into three classes where the first is concentrated on the displacement-based formulation of the employed 20-node isoparametric solid element and the construction of its mass and stiffness matrices. The second part, which aims at mitigating the computational cost of eigenvalue analysis, deals with model order reduction techniques in order to achieve time-affordable solutions for the extraction of modal properties, given the large number of degrees of freedom contained in the implemented models. Finally, the third section of this chapter is focused on the dynamic analysis of multi-degree-of-freedom modal-based systems. Within this context the Newmark method is implemented and its general scheme is presented for the two versions of constant-average and linear acceleration.

Chapter 3 presents the theoretical background of OMA. Using the dynamic equations of motion of a linear system in the continuous-time domain as a starting point, the reduced-order state-space model in discrete-time domain is derived in order to set the basis for the formulation of the SSI scheme. The latter, derived upon description of the properties of stochastic state-space models, includes the Covariance-driven Stochastic Subspace Identification (SSI-Cov) and Data-driven Stochastic Subspace Identification (SSI-Data) algorithms and is followed by the retrieval of the modal characteristics of the continuous-time model when the corresponding discrete-time is identified. Additionally, a discussion on the key-points of the two algorithms is given and the basic concepts of their implementation in terms of the so-called stabilization diagrams are presented. Thereafter, a brief discussion on agglomerative cluster analysis is presented, in order to allow for automatic identification by means of the SSI algorithms.

In **Chapter 4**, the sensitivity analysis of the structural model is carried out. The numerical model of the undamaged structure is first constructed and its modal properties are extracted.

The sensitivity of the stiffened panel to the dominant degradation mechanisms of corrosion and fatigue cracks is studied by means of changes in the natural frequencies and the corresponding mode shapes. In so doing, three main damage states are considered. The first one pertains to uniform corrosion on both the plate and the stiffeners of the panel with five distinct percentages of wastage. The second deals with pitting corrosion on the plate for various degrees of pitting while the last one refers to fatigue cracks on several possible locations over the structure. Finally, the observability of each damage condition on the modes is assessed and the requirements for vibration-based monitoring are listed.

Chapter 5 deals with the OMA of the examined structure. Considering the stiffened panel as part of a ballast tank, its operational response is generated by applying a sloshing-induced impulsive pressure as input signal. Subsequently, the sensor network configuration is determined and a first implementation and cross-comparison of the SSI algorithms is presented for the reference model, in accordance with the existing performance restrictions. Likewise, the OMA is employed for all damaged models in order to investigate identifiability of structural degradation. The generated results are then presented in terms of tables, clusters and stabilization diagrams, followed by a discussion on the feasibility of damage identification.

Finally, **Chapter 6** provides an overview of the work in terms of conclusions with respect to the obtained results and a short discussion on possible future research for the enhancement of the current formulation.

2 Finite Element Model

The present chapter deals with the theoretical description of the methods used within the framework of the FE analyses. All these methods, which are divided into three sections, are coded in Python and validated using the ANSYS Workbench Verification Manual. The first one refers to the formulation of the 20-node isoparametric solid element which is used for the modelling of stiffened panels. The validation of the code referring to this part is performed using the test case *VMMECH001: Statically Indeterminate Reaction Force Analysis* of ANSYS (2013). In the second section, the method for model order reduction is presented while the last section is focused on the dynamic analysis of modally reduced multi-degree-of-freedom systems using the Newmark method. These two parts are jointly validated through the test cases *VMMECH024: Harmonic Response of a Single Degree od Freedom System for Beams* and *VMMECH080: Transient Response of a Spring-mass System* of the aforementioned manual.

2.1 Hexahedral element

For the implementation of the FE method, towards the numerical modelling of stiffened panels, the 20-node isoparametric hexahedral element is employed (Bathe, 1996). Although costly in terms of computational time and mesh generation, the option of brick elements, and especially of high order, enables the modelling of solid bodies without the need of geometric simplifications, while it can appropriately accommodate the detailed and localized modelling of the desired degradation mechanisms.

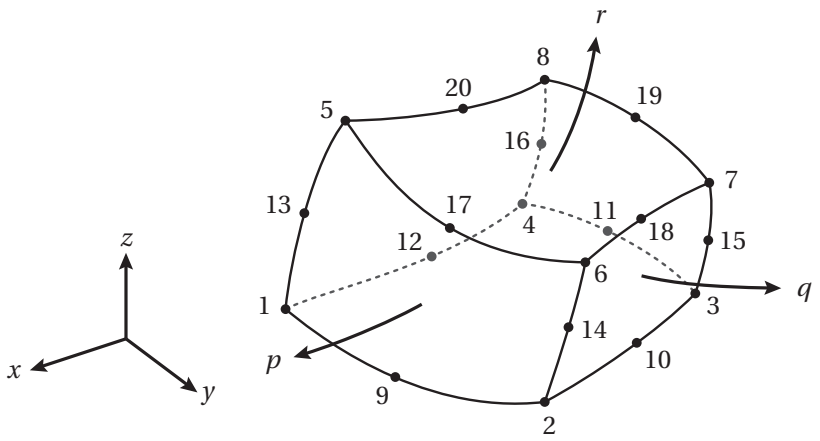

Figure 2.1: The 20-node hexahedron element

In formulating the stiffness and mass matrix of a 20-node isoparametric hexahedron element, which is schematically represented in Fig. 2.1, the natural coordinate system is introduced with coordinates p, q and r ranging from -1 to 1.

Within the isoparametric and displacement-based formulation of the FE method, the displacement field of an element is interpolated in the same way as the geometry. Namely, the cartesian coordinates x, y and z at any point of the element are expressed as function of the corresponding nodal coordinates:

$$x = \sum_{i=1}^{n} \mathrm{N}_i^{\mathrm{e}}(p,q,r)\, x_i, \qquad y = \sum_{i=1}^{n} \mathrm{N}_i^{\mathrm{e}}(p,q,r)\, y_i, \qquad z = \sum_{i=1}^{n} \mathrm{N}_i^{\mathrm{e}}(p,q,r)\, z_i \tag{2.1}$$

while in the same fashion, the displacements u, v and w at any point of the element are obtained by interpolating the displacements at its nodes:

$$u = \sum_{i=1}^{n} \mathrm{N}_i^{\mathrm{e}}(p,q,r)\, u_i, \qquad v = \sum_{i=1}^{n} \mathrm{N}_i^{\mathrm{e}}(p,q,r)\, v_i, \qquad w = \sum_{i=1}^{n} \mathrm{N}_i^{\mathrm{e}}(p,q,r)\, w_i \tag{2.2}$$

In the above formulas, $\mathrm{N}_i^{\mathrm{e}}(p,q,r)$ denotes the interpolation functions, defined in the natural coordinate system of the element with variables p, q and r ranging from -1 to 1, while x_i, y_i, z_i and u_i, v_i, w_i express the nodal coordinates and nodal displacements respectively. The number of summation terms n represents the order of the element in terms of nodes which in this particular case is equal to 20.

The shape functions of the 20-node solid element, which belongs in the family of serendipity elements without internal nodes, may be divided into four groups according to their reference nodes. Hence, for the corner nodes $i = 1, 2, ..., 8$:

$$\mathrm{N}_i^{\mathrm{e}}(p,q,r) = \frac{1}{8}\left(1 + p\,p_i\right)\left(1 + q\,q_i\right)\left(1 + r\,r_i\right)\left(p\,p_i + q\,q_i + r\,r_i - 2\right) \tag{2.3}$$

for the mid-side nodes with $q_i = 0$, for $i = 9, 11, 17, 19$:

$$\mathrm{N}_i^{\mathrm{e}}(p,q,r) = \frac{1}{4}\left(1 - q^2\right)\left(1 + r\,r_i\right)\left(1 + p\,p_i\right) \tag{2.4}$$

for the mid-side nodes with $p_i = 0$, for $i = 10, 12, 18, 20$:

$$\mathrm{N}_i^{\mathrm{e}}(p,q,r) = \frac{1}{4}\left(1 - p^2\right)\left(1 + q\,q_i\right)\left(1 + r\,r_i\right) \tag{2.5}$$

and for the mid-side nodes with $r_i = 0$, for $i = 13, 14, 15, 16$:

$$\mathrm{N}_i^{\mathrm{e}}(p,q,r) = \frac{1}{4}\left(1 - r^2\right)\left(1 + p\,p_i\right)\left(1 + q\,q_i\right) \tag{2.6}$$

with p_i, q_i and r_i denoting the coordinates of node i in the natural coordinate system. It should be noticed that the following formulation is based on the node-numbering pattern illustrated in Fig. 2.1, which guarantees a positive volume, and therefore any change in this rule should be accordingly accounted for in the following derivations.

2.1.1 Deformation matrix

In order for an element stiffness matrix to be constructed, the strain-displacement deformation matrix $\mathbf{B}^{\mathrm{e}} \in \mathbb{R}^{6\times n}$ should be first evaluated. In doing so, the derivatives $\partial/\partial x$, $\partial/\partial y$ and $\partial/\partial z$ of the displacement field represented by Eqs. (2.2) are required. Considering that the displacement field is defined in natural coordinates, the corresponding partial derivatives may be then expressed through the following chain rule:

$$\frac{\partial}{\partial x} = \frac{\partial}{\partial p}\frac{\partial p}{\partial x} + \frac{\partial}{\partial q}\frac{\partial q}{\partial x} + \frac{\partial}{\partial r}\frac{\partial r}{\partial x} \tag{2.7}$$

However, use of the said chain rule is not straightforward since calculation of $\partial p/\partial x$, $\partial q/\partial x$ and $\partial r/\partial x$ implies that the explicit inverse formulas of Eqs. (2.2) are known. Therefore, using the chain rule for the derivatives with respect to the natural coordinates, it can be written:

$$\begin{bmatrix} \dfrac{\partial}{\partial p} \\ \dfrac{\partial}{\partial q} \\ \dfrac{\partial}{\partial r} \end{bmatrix} = \begin{bmatrix} \dfrac{\partial x}{\partial p} & \dfrac{\partial y}{\partial p} & \dfrac{\partial z}{\partial p} \\ \dfrac{\partial x}{\partial q} & \dfrac{\partial y}{\partial q} & \dfrac{\partial z}{\partial q} \\ \dfrac{\partial x}{\partial r} & \dfrac{\partial y}{\partial r} & \dfrac{\partial z}{\partial r} \end{bmatrix} \begin{bmatrix} \dfrac{\partial}{\partial x} \\ \dfrac{\partial}{\partial y} \\ \dfrac{\partial}{\partial z} \end{bmatrix} \tag{2.8}$$

or in matrix notation

$$\frac{\partial}{\partial \mathbf{p}} = \mathbf{J_N}\frac{\partial}{\partial \mathbf{x}} \tag{2.9}$$

where $\mathbf{J_N} \in \mathbb{R}^{3\times 3}$ is the Jacobian operator connecting the natural coordinate derivatives to the cartesian coordinate derivatives. This can be readily obtained from Eqs. (2.1) and the sought for derivatives may be obtained through the inverse of the Jacobian matrix according to:

$$\frac{\partial}{\partial \mathbf{x}} = \mathbf{J_N}^{-1}\frac{\partial}{\partial \mathbf{p}} \tag{2.10}$$

This operation requires of course that the inverse of $\mathbf{J_N}$ exists which is always ensured when the correspondence between the natural and the cartesian coordinates is a one-to-one correspondence.

Since the derivatives $\partial u/\partial x$, $\partial u/\partial y$, $\partial u/\partial z$, $\partial v/\partial x$,..., $\partial w/\partial z$ can be evaluated through Eq. (2.10), the strain-displacement transformation matrix $\mathbf{B}^{\mathrm{e}}$ may also be constructed, with the strain vector related to it by the formula:

$$\boldsymbol{\epsilon} = \mathbf{B}^{\mathrm{e}}(p,q,r)\,\mathbf{u}^{\mathrm{e}} \quad \text{where} \quad \mathbf{B}^{\mathrm{e}}(p,q,r) = \mathbf{D}\,\mathbf{N}^{\mathrm{e}}(p,q,r) \tag{2.11}$$

where $\mathbf{u}^{\mathrm{e}} \in \mathbb{R}^{3n}$ is a vector collecting the nodal displacements of Eqs. (2.2). Additionally, matrix $\mathbf{D} \in \mathbb{R}^{6\times 3}$ denotes the partial derivative operator which is derived from the inverse Jacobian matrix and expressed by the following relation:

$$\mathbf{D}^{\mathrm{T}} = \begin{bmatrix} \dfrac{\partial}{\partial x} & 0 & 0 & \dfrac{\partial}{\partial y} & 0 & \dfrac{\partial}{\partial z} \\ 0 & \dfrac{\partial}{\partial y} & 0 & \dfrac{\partial}{\partial x} & \dfrac{\partial}{\partial z} & 0 \\ 0 & 0 & \dfrac{\partial}{\partial z} & 0 & \dfrac{\partial}{\partial y} & \dfrac{\partial}{\partial x} \end{bmatrix} \tag{2.12}$$

while $\mathbf{N}^{\mathrm{e}} \in \mathbb{R}^{3\times 3n}$ is the shape function matrix which for the 20-node element is given by:

$$\mathbf{N}^{\mathrm{e}} = \begin{bmatrix} \mathrm{N}_1^{\mathrm{e}} & 0 & 0 & \mathrm{N}_2^{\mathrm{e}} & 0 & 0 & \cdots & \mathrm{N}_{20}^{\mathrm{e}} & 0 & 0 \\ 0 & \mathrm{N}_1^{\mathrm{e}} & 0 & 0 & \mathrm{N}_2^{\mathrm{e}} & 0 & \cdots & 0 & \mathrm{N}_{20}^{\mathrm{e}} & 0 \\ 0 & 0 & \mathrm{N}_1^{\mathrm{e}} & 0 & 0 & \mathrm{N}_2^{\mathrm{e}} & \cdots & 0 & 0 & \mathrm{N}_{20}^{\mathrm{e}} \end{bmatrix} \tag{2.13}$$

It is visible that matrix $\mathbf{D}$ operates on the shape function matrix and therefore the partial derivatives of $\mathrm{N}_i^{\mathrm{e}}$ for $i = 1,2,...,20$ are evaluated upon utilization of Eq. (2.10).

2.1.2 Stiffness matrix

The element stiffness matrix referring to the local degrees of freedom may be obtained through the principle of virtual work as a function of the deformation matrix and the constitutive matrix $\mathbf{E} \in \mathbb{R}^{6\times 6}$ according to :

$$\mathbf{K}^{\mathrm{e}} = \int_{\mathrm{V}^{\mathrm{e}}} \left(\mathbf{B}^{\mathrm{e}}\right)^{\mathrm{T}} \mathbf{E}\mathbf{B}^{\mathrm{e}}\, d\mathrm{V}^{\mathrm{e}} \tag{2.14}$$

The volume integral in the above relation is expressed in natural coordinates and therefore the volume differential $d\mathrm{V}^{\mathrm{e}}$ should be also written in terms of p, q and r. Hence, this is carried out by:

$$d\mathrm{V}^{\mathrm{e}} = \det\left(\mathbf{J}_{\mathbf{N}}\right) dp\, dq\, dr \tag{2.15}$$

with $\det\left(\mathbf{J}_{\mathbf{N}}\right)$ being the determinant of the Jacobian operator.

2.1.3 Mass matrix

Within the context of a variational formulation, the construction of mass matrix is based on the kinetic energy T^{e} contained by an element of mass density ρ which occupies a domain V^{e} and moves with velocity $\mathbf{v}^{\mathrm{e}}$:

$$\mathrm{T}^{\mathrm{e}} = \frac{1}{2} \int_{\mathrm{V}^{\mathrm{e}}} \rho \left(\mathbf{v}^{\mathrm{e}}\right)^{\mathrm{T}} \mathbf{v}^{\mathrm{e}}\, d\mathrm{V}^{\mathrm{e}} \tag{2.16}$$

Additionally, in the framework of the FE method, the velocity field is interpolated by the shape functions, so that $\mathbf{v}^{\mathrm{e}} = \mathbf{N}^{\mathrm{e}}\dot{\mathbf{u}}^{\mathrm{e}}$ with $\dot{\mathbf{u}}^{\mathrm{e}}$ denoting the nodal velocities. Hence, substitution of the interpolation relation into Eq. (2.16) yields:

$$\mathrm{T}^{\mathrm{e}} = \frac{1}{2}\left(\dot{\mathbf{u}}^{\mathrm{e}}\right)^{\mathrm{T}} \left(\int_{\mathrm{V}^{\mathrm{e}}} \rho \left(\mathbf{N}^{\mathrm{e}}\right)^{\mathrm{T}} \mathbf{N}^{\mathrm{e}}\, d\mathrm{V}^{\mathrm{e}} \right) \dot{\mathbf{u}}^{\mathrm{e}} = \frac{1}{2}\left(\dot{\mathbf{u}}^{\mathrm{e}}\right)^{\mathrm{T}} \mathbf{M}^{\mathrm{e}}\, \dot{\mathbf{u}}^{\mathrm{e}} \tag{2.17}$$

where the mass matrix $\mathbf{M}^{\mathrm{e}}$ is the Hessian of kinetic energy T^{e}. Analytically, the mass matrix can be then obtained from the following expression:

$$\mathbf{M}^{\mathrm{e}} = \int_{\mathrm{V}^{\mathrm{e}}} \rho \left(\mathbf{N}^{\mathrm{e}}\right)^{\mathrm{T}} \mathbf{N}^{\mathrm{e}} \, d\mathrm{V}^{\mathrm{e}} \tag{2.18}$$

where the integration volume $d\mathrm{V}^{\mathrm{e}}$ should be also substituted by Eq. (2.15) so that the integral is expressed in natural coordinates.

2.1.4 Numerical integration

It can be seen that explicit evaluation of the volume integrals described by Eqs. (2.14) and (2.18) is not in general computationally effective and especially when high interpolation order is employed. Therefore, the required integrals are numerically evaluated using the well-known Gauss quadrature rules, with the stiffness matrix expression reading:

$$\mathbf{K}^{\mathrm{e}} = \sum_{i=1}^{s_1} \sum_{j=1}^{s_2} \sum_{k=1}^{s_3} w_i w_j w_k \left(\mathbf{B}^{\mathrm{e}}_{ijk}\right)^{\mathrm{T}} \mathbf{E} \mathbf{B}^{\mathrm{e}}_{ijk} \det\left(\mathbf{J}_{\mathbf{N}ijk}\right) \tag{2.19}$$

and the corresponding relation for the mass matrix:

$$\mathbf{M}^{\mathrm{e}} = \sum_{i=1}^{s_1} \sum_{j=1}^{s_2} \sum_{k=1}^{s_3} w_i w_j w_k \, \rho \left(\mathbf{N}^{\mathrm{e}}_{ijk}\right)^{\mathrm{T}} \mathbf{N}^{\mathrm{e}}_{ijk} \det\left(\mathbf{J}_{\mathbf{N}ijk}\right) \tag{2.20}$$

where s_1, s_2 and s_3 are the number of Gauss integration points along the natural coordinate axes p, q and r respectively. Similarly, w_1, w_2 and w_3 denote the integration weights along the natural axes while $\mathbf{B}^{\mathrm{e}}_{ijk}$, $\det\left(\mathbf{J}_{\mathbf{N}ijk}\right)$ and $\mathbf{N}^{\mathrm{e}}_{ijk}$ are abbreviations for the following formulas:

$$\mathbf{B}^{\mathrm{e}}_{ijk} = \mathbf{B}^{\mathrm{e}}\left(p_i, q_j, r_k\right), \quad \det\left(\mathbf{J}_{\mathbf{N}ijk}\right) = \det\left(\mathbf{J}_{\mathbf{N}}(p_i, q_j, r_k)\right), \quad \mathbf{N}^{\mathrm{e}}_{ijk} = \mathbf{N}^{\mathrm{e}}\left(p_i, q_j, r_k\right) \tag{2.21}$$

It should be noticed that, generally, the number of integration points is chosen the same in all directions: $s_1 = s_2 = s_3 = s$ with the total number of Gauss points being equal to s^3. In the case of the 20-node hexahedral element, the minimum rank-sufficient rule comprises three integration points in each direction, with $s = 3$.

2.2 Model order reduction

In this section, the techniques used for the reduction of large-sized models are presented with ultimate aim to create accurate low-order and computationally effective dynamic models. Such a need stems from the requirement of detailed modelling of stiffened panels with high-order solid elements, leading to large-sized eigenvalue problems which become significantly demanding in terms of computational resources. In achieving this order reduction, the Guyan condensation method is implemented along with a scheme for the selection of the reduced degrees of freedom.

2.2.1 Dynamic condensation

In reducing the size of a dynamic system described by the following governing equations of motion:

$$\mathbf{M}\ddot{\mathbf{u}}(t) + \mathbf{C}\dot{\mathbf{u}}(t) + \mathbf{K}\mathbf{u}(t) = \mathbf{f}(t) = \mathbf{S}_\mathrm{p}\,\mathbf{p}(t) \tag{2.22}$$

a partition scheme is adopted so that the considered degrees of freedom in Eq. (2.22) are divided into masters and slaves. As denoted by the notation, upon condensation, the reduced-order equations will constitute an expression with respect to the master degrees of freedom while the slave degrees of freedom will be the ones to be condensed. Assuming that a division between masters and slaves is available, Eq. (2.22) can be thus partitioned as follows:

$$\begin{bmatrix} \mathbf{M}_\mathrm{mm} & \mathbf{M}_\mathrm{ms} \\ \mathbf{M}_\mathrm{sm} & \mathbf{M}_\mathrm{ss} \end{bmatrix} \begin{bmatrix} \ddot{\mathbf{u}}_\mathrm{m}(t) \\ \ddot{\mathbf{u}}_\mathrm{s}(t) \end{bmatrix} + \begin{bmatrix} \mathbf{C}_\mathrm{mm} & \mathbf{C}_\mathrm{ms} \\ \mathbf{C}_\mathrm{sm} & \mathbf{C}_\mathrm{ss} \end{bmatrix} \begin{bmatrix} \dot{\mathbf{u}}_\mathrm{m}(t) \\ \dot{\mathbf{u}}_\mathrm{s}(t) \end{bmatrix} + \begin{bmatrix} \mathbf{K}_\mathrm{mm} & \mathbf{K}_\mathrm{ms} \\ \mathbf{K}_\mathrm{sm} & \mathbf{K}_\mathrm{ss} \end{bmatrix} \begin{bmatrix} \mathbf{u}_\mathrm{m}(t) \\ \mathbf{u}_\mathrm{s}(t) \end{bmatrix} = \begin{bmatrix} \mathbf{f}_\mathrm{m}(t) \\ \mathbf{f}_\mathrm{s}(t) \end{bmatrix}$$

with the indices "m" and "s" denoting the master and slave degrees of freedom respectively. Assuming that the force vector $\mathbf{f}_\mathrm{s}(t)$ referring to the slave degrees of freedom is equal to zero, the second equation of Eq. (2.2.1) may be written as:

$$\mathbf{M}_\mathrm{sm}\ddot{\mathbf{u}}_\mathrm{m}(t) + \mathbf{M}_\mathrm{ss}\ddot{\mathbf{u}}_\mathrm{s}(t) + \mathbf{C}_\mathrm{sm}\dot{\mathbf{u}}_\mathrm{m}(t) + \mathbf{C}_\mathrm{ss}\dot{\mathbf{u}}_\mathrm{s}(t) + \mathbf{K}_\mathrm{sm}\mathbf{u}_\mathrm{m}(t) + \mathbf{K}_\mathrm{ss}\mathbf{u}_\mathrm{s}(t) = 0 \tag{2.23}$$

It can be seen that the extraction of a relation between masters and slaves is not possible through Eq. (2.23) since all derivatives of the displacement field are present. The main assumption of the Guyan reduction scheme within the framework of a dynamic problem consists in ignoring the dynamic effects so that both velocity and acceleration at masters and slaves is assumed to be zero. Hence, substitution into Eq. (2.23) leads to the relation between masters and slaves which can be subsequently used for the transformation of the full displacement vector:

$$\mathbf{u}(t) = \mathbf{T}_\mathrm{c}\,\mathbf{u}_\mathrm{m}(t) = \begin{bmatrix} \mathbf{I} \\ \mathbf{R}_\mathrm{c} \end{bmatrix} \mathbf{u}_\mathrm{m}(t), \quad \text{where} \quad \mathbf{R}_\mathrm{c} = -\mathbf{K}_\mathrm{ss}^{-1}\mathbf{K}_\mathrm{sm} \tag{2.24}$$

in which $\mathbf{R}_\mathrm{c} \in \mathbb{R}^{n_\mathrm{c} \times n_\mathrm{r}}$ is called the condensation matrix relating masters and slaves, while n_r and n_c denote the number of master and slave degrees of freedom respectively. Substituting then Eq. (2.24) into the equation of motion an premultiplying with the transpose of the transformation matrix $\mathbf{T}_\mathrm{c}$, results in the expressions of the reduced mass, damping and stiffness matrices as well as the equivalent force vector:

$$\mathbf{M}_\mathrm{c} = \mathbf{T}_\mathrm{c}^\mathrm{T}\mathbf{M}\mathbf{T}_\mathrm{c}, \quad \mathbf{C}_\mathrm{c} = \mathbf{T}_\mathrm{c}^\mathrm{T}\mathbf{C}\mathbf{T}_\mathrm{c}, \quad \mathbf{K}_\mathrm{c} = \mathbf{T}_\mathrm{c}^\mathrm{T}\mathbf{K}\mathbf{T}_\mathrm{c}, \quad \mathbf{f}_\mathrm{c}(t) = \mathbf{T}_\mathrm{c}^\mathrm{T}\mathbf{f}(t) \tag{2.25}$$

Within the context of an eigenvalue problem, the dynamic properties are obtained in terms of the undamped system where only the stiffness and mass matrices are of interest. Therefore, the analytical reduced-order expressions for the stiffness and mass matrix derived from Eqs. (2.25) read:

$$\mathbf{K}_c = \mathbf{K}_{mm} - \mathbf{K}_{ms}\mathbf{K}_{ss}^{-1}\mathbf{K}_{sm} \tag{2.26}$$

$$\mathbf{M}_c = \mathbf{M}_{mm} + \mathbf{K}_{ms}\mathbf{K}_{ss}^{-1}\mathbf{M}_{ss}\mathbf{K}_{ss}^{-1}\mathbf{K}_{sm} - \mathbf{K}_{ms}\mathbf{K}_{ss}^{-1}\mathbf{M}_{sm} - \mathbf{M}_{ms}\mathbf{K}_{ss}^{-1}\mathbf{K}_{sm} \tag{2.27}$$

Following the same partition scheme as for the dynamic problem of Eq. (2.22), the undamped eigenvalue problem may be written in partitioned matrix notation as:

$$\left(\begin{bmatrix}\mathbf{K}_{mm} & \mathbf{K}_{ms}\\ \mathbf{K}_{sm} & \mathbf{K}_{ss}\end{bmatrix} - \lambda\begin{bmatrix}\mathbf{M}_{mm} & \mathbf{M}_{ms}\\ \mathbf{M}_{sm} & \mathbf{M}_{ss}\end{bmatrix}\right)\begin{bmatrix}\boldsymbol{\phi}_m\\ \boldsymbol{\phi}_s\end{bmatrix} = \begin{bmatrix}\mathbf{0}\\ \mathbf{0}\end{bmatrix} \tag{2.28}$$

which can be equivalently rewritten into the following set of equations:

$$\left(\mathbf{K}_{mm} - \lambda\mathbf{M}_{mm}\right)\boldsymbol{\phi}_m + \left(\mathbf{K}_{ms} - \lambda\mathbf{M}_{ms}\right)\boldsymbol{\phi}_s = 0 \tag{2.29}$$

$$\left(\mathbf{K}_{sm} - \lambda\mathbf{M}_{sm}\right)\boldsymbol{\phi}_m + \left(\mathbf{K}_{ss} - \lambda\mathbf{M}_{ss}\right)\boldsymbol{\phi}_s = 0 \tag{2.30}$$

Solution of the second equation with respect to the slave degrees of freedom yields the corresponding relation between the mode shape vector referring to the slaves and the one referring to the masters:

$$\boldsymbol{\phi}_s = \mathbf{R}(\lambda)\boldsymbol{\phi}_m \tag{2.31}$$

in which the condensation matrix $\mathbf{R}(\lambda)$ is now a nonlinear function of the unknown eigenvalue λ given by the following equation:

$$\mathbf{R}_c(\lambda) = -\left(\mathbf{K}_{ss} - \lambda\mathbf{M}_{ss}\right)^{-1}\left(\mathbf{K}_{sm} - \lambda\mathbf{M}_{sm}\right) \tag{2.32}$$

Considering the condensation matrix for a zero eigenvalue λ, leads to the Guyan condensation matrix provided by Eq. (2.24) and accordingly to the same transformation matrix $\mathbf{T}_c$, so that the full mode shape vector is related to the master vector by:

$$\boldsymbol{\phi} = \mathbf{T}_c\boldsymbol{\phi}_m \tag{2.33}$$

Finally, introducing Eq. (2.33) into the eigenproblem equation and premultiplying by the transpose of the coordinate transformation matrix results in the reduced eigenproblem:

$$\left(\mathbf{K}_c - \lambda\mathbf{M}_c\right)\boldsymbol{\phi}_m = 0 \tag{2.34}$$

where $\mathbf{K}_c$ and $\mathbf{M}_c$ denote the reduced stiffness and mass matrices, defined by Eqs. (2.27). It should be noticed that for the derivation of the Guyan condensation scheme for eigenproblems, the eigenvalue is considered to be zero. Such an assumption implies that the dynamic effects are not accounted for in the condensation matrix and constitutes therefore a static reduction method. In this sense, the ignored effects become more and more significant as the

neglected eigenvalues increase and subsequently the method is becoming less accurate.

2.2.2 Selection of reduced degrees of freedom

The selection of the degrees of freedom to be condensed is based on the scheme proposed by Shah and Raymund (1982), where for further details the reader is referred to Qu (2004). Within this scheme, a cut-off frequency ω_c for the eigenvalues $\lambda_1 \leq \lambda_2 \leq ... \leq \lambda_{n_{dof}}$ of a full-order model is defined. This frequency should be significantly higher than the frequency range of interest and as suggested by Shah and Raymund it should be approximately three times larger than the highest significant frequency.

The idea behind this scheme consists in sequentially finding and eliminating the degree of freedom with the highest ratio $r_1^2 = k_{ii}/m_{ii}$, provided that $r_1 > \omega_c$. Then for the reduced eigenproblem of size $(n_{dof}-1) \times (n_{dof}-1)$ with eigenvalues $\lambda_{11} \leq \lambda_{12} \leq ... \leq \lambda_{1(n_{dof}-1)}$, it can be stated that the eigenvalue λ_{1i} is an upper bound of the full-order eigenvalue λ_i, so that:

$$\lambda_1 \leq \lambda_{11} \leq \lambda_2 \leq \lambda_{12} \leq \lambda_3 \leq ... \leq \lambda_{(n_{dof}-1)} \leq \lambda_{1(n_{dof}-1)} \leq \lambda_{(n_{dof}-1)} \tag{2.35}$$

Subsequently, the elimination process is applied to the reduced order model and the next slave degree of freedom is condensed. The procedure is repeated for the elimination of n_c degrees of freedom until the highest ratio $r_{n_c}^2$ is smaller than the cut-off frequency ω_c. Hence, the remaining $(n_{dof} - n_c)$ degrees of freedom of the reduced order representation constitute the master degrees of freedom while the eliminated ones are the slaves. Hence, the entire process may be summarized in the following four steps:

a. Discover the degree of freedom with the largest ratio k_{ii}/m_{ii}. In case more than one degrees of freedom share the same ratio, the one with the smallest index is chosen.

b. If the ratio k_{ii}/m_{ii} is greater than ω_c^2, condensate the selected degree of freedom using the Guyan method.

c. Repeat steps a. and b. to the matrices obtained at step b.

d. Repeat steps a. b. and c. until the largest ratio k_{ii}/m_{ii} of step a. is equal to ω_c^2

2.3 Dynamic analysis

The objective of this section is to describe the employed numerical scheme for the solution of the system of differential equations governing the dynamic response of multi-degree-of-freedom systems which is described by Eqs. (2.22) and subject to the initial conditions:

$$\mathbf{u}(0) = \mathbf{u}_0 \quad \text{and} \quad \dot{\mathbf{u}}(0) = \dot{\mathbf{u}}_0 \tag{2.36}$$

at $t = 0$. For systems with a few degrees of freedom, Eqs. (2.22) and (2.36) can be solved in their present form however, for large systems it is computationally effective to transform them in modal coordinates and express the nodal quantities in terms of the first few vibration modes. Therefore, the nodal displacements and accordingly velocities and accelerations may be approximated by a linear combination of the first n_m modes:

$$\mathbf{u}(t) \approx \sum_{i=1}^{n_m} \boldsymbol{\phi}_i \mathbf{z}_i(t) = \boldsymbol{\Phi}\mathbf{z}(t) \tag{2.37}$$

Using the above transformation, the full-order equation of motion may be also rewritten in modal form:

$$\ddot{\mathbf{z}}(t) + \boldsymbol{\Gamma}\dot{\mathbf{z}}(t) + \boldsymbol{\Omega}^2\mathbf{z}(t) = \boldsymbol{\Phi}^{\mathrm{T}}\mathbf{S}_{\mathrm{p}}\mathbf{p}(t) \tag{2.38}$$

where $\boldsymbol{\Gamma} = \boldsymbol{\Phi}^{\mathrm{T}}\mathbf{C}\boldsymbol{\Phi}$ and $\boldsymbol{\Omega}^2 = \boldsymbol{\Phi}^{\mathrm{T}}\mathbf{K}\boldsymbol{\Phi}$ are the modal damping and modal stiffness matrices respectively.

2.3.1 The Newmark method

Generally, within the context of a numerical integration scheme, the time scale is divided into a set of time steps, with duration Δt. In this sense, the excitation vector is evaluated at discrete time instants $t_k = k\Delta t$, denoted by $\mathbf{p}_k = \mathbf{p}(t_k)$. Accordingly, the response in terms of displacements, velocities and accelerations is determined at the same time instants, denoted by $\mathbf{z}_k = \mathbf{z}(t_k)$, $\dot{\mathbf{z}}_k = \dot{\mathbf{z}}(t_k)$ and $\ddot{\mathbf{z}}_k = \ddot{\mathbf{z}}(t_k)$ respectively.

In particular, the Newmark method which is to be employed within this project (Chopra, 2012), is based on an assumption with regard to the evolution of the acceleration during a time step. In imposing such assumption, the displacement and velocity vectors at time instant t_k are first approximated by a truncated Taylor series according to the following expressions:

$$\mathbf{z}_k = \mathbf{z}_{k-1} + \Delta t\,\dot{\mathbf{z}}_{k-1} + \frac{\Delta t^2}{2}\ddot{\mathbf{z}}_{k-1} + \frac{\Delta t^3}{6}\mathbf{z}^{(3)}_{k-1} \tag{2.39}$$

$$\dot{\mathbf{z}}_k = \dot{\mathbf{z}}_{k-1} + \Delta t\,\ddot{\mathbf{z}}_{k-1} + \frac{\Delta t^2}{2}\mathbf{z}^{(3)}_{k-1} \tag{2.40}$$

Thereafter, assuming that acceleration varies linearly within a time step, the third derivative may be written as:

$$\mathbf{z}^{(3)}_{k-1} = \frac{\ddot{\mathbf{z}}_k - \ddot{\mathbf{z}}_{k-1}}{\Delta t} \tag{2.41}$$

which upon substitution in Eqs. (2.39) and (2.40) yields the parametrized expressions for the displacement and velocity vectors at time t_k, in terms of the parameters β and γ:

$$\dot{\mathbf{z}}_k = \dot{\mathbf{z}}_{k-1} + (1-\gamma)\Delta t\,\ddot{\mathbf{z}}_{k-1} + \gamma\Delta t\,\ddot{\mathbf{z}}_k \tag{2.42}$$

$$\mathbf{z}_k = \mathbf{z}_{k-1} + \Delta t\,\dot{\mathbf{z}}_{k-1} + (0.5-\beta)\Delta t^2\ddot{\mathbf{z}}_{k-1} + \beta\Delta t^2\ddot{\mathbf{z}}_k \tag{2.43}$$

For $\beta = \frac{1}{4}$ and $\gamma = \frac{1}{2}$ the above formulas coincide with Eqs. (2.39) and (2.40) and express the average acceleration method while for $\beta = \frac{1}{6}$ and $\gamma = \frac{1}{2}$ the constant acceleration method is obtained. It is observed that Eq. (2.43) may be solved for $\ddot{\mathbf{z}}_k$ which upon substitution in Eq. (2.42) yields the expression of $\dot{\mathbf{z}}_k$, described by the following equations respectively:

$$\ddot{\mathbf{z}}_k = \frac{1}{\beta \Delta t^2}(\mathbf{z}_k - \mathbf{z}_{k-1}) - \frac{1}{\beta \Delta t}\dot{\mathbf{z}}_{k-1} - \left(\frac{1}{2\beta} - 1\right)\ddot{\mathbf{z}}_{k-1} \tag{2.44}$$

$$\dot{\mathbf{z}}_k = \frac{\gamma}{\Delta t}(\mathbf{z}_k - \mathbf{z}_{k-1}) + \left(1 - \frac{\gamma}{\beta}\right)\dot{\mathbf{z}}_{k-1} + \Delta t\left(1 - \frac{\gamma}{2\beta}\right)\ddot{\mathbf{z}}_{k-1} \tag{2.45}$$

Hereafter, substitution of Eqs. (2.44) and (2.45) into the modal-based equation of motion yields the sought for expression for $\mathbf{z}_k$:

$$\hat{\mathbf{\Omega}}\mathbf{z}_k = \hat{\mathbf{p}}_k \tag{2.46}$$

where $\hat{\mathbf{\Omega}}$ is the equivalent modal stiffness matrix given by:

Selection of parameters

Constant average acceleration method $\left(\gamma = \frac{1}{2},\ \beta = \frac{1}{4}\right)$

Linear acceleration method $\left(\gamma = \frac{1}{2},\ \beta = \frac{1}{6}\right)$

Initialization at time t_0:

$$\mathbf{z}_{i0} = \frac{\boldsymbol{\phi}_i^{\mathrm{T}}\mathbf{M}\mathbf{u}_0}{\boldsymbol{\phi}_i^{\mathrm{T}}\mathbf{M}\boldsymbol{\phi}_i}, \quad \dot{\mathbf{z}}_{i0} = \frac{\boldsymbol{\phi}_i^{\mathrm{T}}\mathbf{M}\dot{\mathbf{u}}_0}{\boldsymbol{\phi}_i^{\mathrm{T}}\mathbf{M}\boldsymbol{\phi}_i}$$

$$\ddot{\mathbf{z}}_0 = \mathbf{\Phi}^{\mathrm{T}}\mathbf{S}_{\mathrm{p}}\mathbf{p}_0 - \mathbf{\Gamma}\dot{\mathbf{z}}_0 - \mathbf{\Omega}^2\mathbf{z}_0$$

$$\mathbf{c}_1 = \frac{1}{\beta \Delta t^2}\mathbf{I} + \frac{\gamma}{\beta \Delta t}\mathbf{\Gamma}$$

$$\mathbf{c}_2 = \frac{1}{\beta \Delta t}\mathbf{I} + \left(\frac{\gamma}{\beta} - 1\right)\mathbf{\Gamma}$$

$$\mathbf{c}_3 = \left(\frac{1}{2\beta} - 1\right)\mathbf{I} + \Delta t\left(\frac{\gamma}{2\beta} - 1\right)\mathbf{\Gamma}$$

$$\hat{\mathbf{\Omega}} = \mathbf{\Omega}^2 + \mathbf{c}_1$$

At time t_k, for $k = 1, \ldots, \mathrm{N}_t$:

$$\hat{\mathbf{p}}_k = \mathbf{\Phi}^{\mathrm{T}}\mathbf{S}_{\mathrm{p}}\mathbf{p}_k + \mathbf{c}_1\mathbf{z}_{k-1} + \mathbf{c}_2\dot{\mathbf{z}}_{k-1} + \mathbf{c}_3\ddot{\mathbf{z}}_{k-1}$$

$$\mathbf{z}_k = \hat{\mathbf{\Omega}}^{-1}\hat{\mathbf{p}}_k$$

$$\dot{\mathbf{z}}_k = \frac{\gamma}{\beta \Delta t}(\mathbf{z}_k - \mathbf{z}_{k-1}) + \left(1 - \frac{\gamma}{\beta}\right)\dot{\mathbf{z}}_{k-1} + \Delta t\left(1 - \frac{\gamma}{2\beta}\right)\ddot{\mathbf{z}}_{k-1}$$

$$\ddot{\mathbf{z}}_k = \frac{1}{\beta \Delta t^2}(\mathbf{z}_k - \mathbf{z}_{k-1}) - \frac{1}{\beta \Delta t}\dot{\mathbf{z}}_{k-1} - \left(\frac{1}{2\beta} - 1\right)\ddot{\mathbf{z}}_{k-1}$$

$$\mathbf{u}_k = \mathbf{\Phi}\mathbf{z}_k, \quad \dot{\mathbf{u}}_k = \mathbf{\Phi}\dot{\mathbf{z}}_k, \quad \ddot{\mathbf{u}}_k = \mathbf{\Phi}\ddot{\mathbf{z}}_k$$

Table 2.1: The general scheme for Newmark's method

$$\hat{\mathbf{\Omega}} = \mathbf{\Omega}^2 + \mathbf{c}_1 \tag{2.47}$$

and $\hat{\mathbf{p}}$ denotes the equivalent modal force vector which reads:

$$\hat{\mathbf{p}}_k = \mathbf{\Phi}^{\mathrm{T}} \mathbf{S}_{\mathrm{p}} \mathbf{p}_k + \mathbf{c}_1 \mathbf{z}_{k-1} + \mathbf{c}_2 \dot{\mathbf{z}}_{k-1} + \mathbf{c}_3 \ddot{\mathbf{z}}_{k-1} \tag{2.48}$$

with the coefficient matrices $\mathbf{c}_1$, $\mathbf{c}_2$ and $\mathbf{c}_3$ being given by the following expressions:

$$\mathbf{c}_1 = \frac{1}{\beta \Delta t^2} \mathbf{I} + \frac{\gamma}{\beta \Delta t} \mathbf{\Gamma} \tag{2.49}$$

$$\mathbf{c}_2 = \frac{1}{\beta \Delta t} \mathbf{I} + \left(\frac{\gamma}{\beta} - 1 \right) \mathbf{\Gamma} \tag{2.50}$$

$$\mathbf{c}_3 = \left(\frac{1}{2\beta} - 1 \right) \mathbf{I} + \Delta t \left(\frac{\gamma}{2\beta} - 1 \right) \mathbf{\Gamma} \tag{2.51}$$

It should be noticed at this point that Newmark's method is unconditionally stable for the constant average acceleration assumption while it becomes conditionally stable when the linear acceleration assumption is adopted. In this case, the time step Δt should be small enough in order to achieve an accurate solution for each one of the modes for $i = 1, 2, ..., n_{\mathrm{m}}$. Such requirement is ensured when $\Delta t \leq 0.551 \mathrm{T}_{n_{\mathrm{m}}}$ with $\mathrm{T}_{n_{\mathrm{m}}}$ denoting the natural period of the n_{m}th mode. In Table 2.1 the general scheme for the time-stepping solution of Newmark's method is presented for both versions of constant average and linear acceleration.

3 System Identification

3.1 Equations of motion

As already described in Chapter 2, the equations of motion in the continuous-time domain for a space-discretized linear system may be written in compact form as follows

$$\mathbf{M}\ddot{\mathbf{u}}(t) + \mathbf{C}\dot{\mathbf{u}}(t) + \mathbf{K}\mathbf{u}(t) = \mathbf{f}(t) = \mathbf{S}_\mathrm{p}\,\mathbf{p}(t) \tag{3.1}$$

where $\mathbf{M}$, $\mathbf{C}$ and $\mathbf{K} \in \mathbb{R}^{n_\mathrm{dof} \times n_\mathrm{dof}}$ are the mass, damping and stiffness matrices while $\ddot{\mathbf{u}}(t)$, $\dot{\mathbf{u}}(t)$ and $\mathbf{u}(t) \in \mathbb{R}^{n_\mathrm{dof}}$ denote the acceleration, velocity and displacement vectors respectively. The excitation vector $\mathbf{f}(t) \in \mathbb{R}^{n_\mathrm{dof}}$ on the right-hand side of the equation of motion may be factorized into the force selection matrix $\mathbf{S}_\mathrm{p} \in \mathbb{R}^{n_\mathrm{dof} \times n_\mathrm{p}}$ and the input force vector $\mathbf{p}(t) \in \mathbb{R}^{n_\mathrm{p}}$ with n_p denoting the number of input forces.

The coupled equations of motion described by Eq. (3.1) are separated upon introduction of the coordinate transformation

$$\mathbf{u}(t) = \mathbf{\Phi}\,\mathbf{z}(t) \tag{3.2}$$

where $\mathbf{z}(t) \in \mathbb{R}^{n_\mathrm{m}}$ is the modal displacement vector and $\mathbf{\Phi} \in \mathbb{R}^{n_\mathrm{dof} \times n_\mathrm{m}}$ is the matrix of eigenmodes obtained by the undamped eigenvalue problem

$$\mathbf{K}\mathbf{\Phi} = \mathbf{M}\mathbf{\Phi}\mathbf{\Omega}^2 \tag{3.3}$$

which contains the eigenvectors $\mathbf{\Phi}_j$ for $j = 1, 2, ..., n_\mathrm{m}$. Substituting Eq. (3.2) into the equation of motion and pre multiplying with $\mathbf{\Phi}^\mathrm{T}$ yields the transformed equation of motion in modal coordinates

$$\ddot{\mathbf{z}}(t) + \mathbf{\Gamma}\dot{\mathbf{z}}(t) + \mathbf{\Omega}^2\,\mathbf{z}(t) = \mathbf{\Phi}^\mathrm{T}\mathbf{S}_\mathrm{p}\,\mathbf{p}(t) \tag{3.4}$$

whereby it is implied that the mode shapes are mass-normalized $\mathbf{\Phi}^\mathrm{T}\mathbf{M}\mathbf{\Phi} = \mathbf{I}$ and the damping is assumed to be proportional $\mathbf{\Phi}^\mathrm{T}\mathbf{C}\mathbf{\Phi} = \mathbf{\Gamma}$. The diagonal matrix $\mathbf{\Omega} \in \mathbb{R}^{n_\mathrm{m} \times n_\mathrm{m}}$ contains the eigenfrequencies ω_j and the modal damping matrix $\mathbf{\Gamma} \in \mathbb{R}^{n_\mathrm{m} \times n_\mathrm{m}}$, which is also diagonal, collects the terms $2\xi_j\omega_j$ with ξ denoting the modal damping ratio.

3.2 State-space models

3.2.1 Continuous-time domain

The formation of the continuous-time state-space model is based on the introduction of the state vector $\mathbf{x}(t) \in \mathbb{R}^{n_s \times n_s}$ in Eq. (3.1), which reads:

$$\mathbf{x}(t) = \begin{bmatrix} \mathbf{u}(t) \\ \dot{\mathbf{u}}(t) \end{bmatrix} \tag{3.5}$$

with $n_s = 2n_{dof}$. The equation of motion can be thus rewritten in the following form:

$$\dot{\mathbf{x}}(t) = \mathbf{A}_c \mathbf{x}(t) + \mathbf{B}_c \mathbf{p}(t) \tag{3.6}$$

in which the system matrices $\mathbf{A}_c \in \mathbb{R}^{n_s \times n_s}$ and $\mathbf{B}_s \in \mathbb{R}^{n_s \times n_p}$ are given by:

$$\mathbf{A}_c = \begin{bmatrix} \mathbf{0} & \mathbf{I} \\ -\mathbf{M}^{-1}\mathbf{K} & -\mathbf{M}^{-1}\mathbf{C} \end{bmatrix}, \quad \mathbf{B}_c = \begin{bmatrix} \mathbf{0} \\ \mathbf{M}^{-1}\mathbf{S}_p \end{bmatrix}$$

With respect to the measurement equation, it is assumed in the general case that a set of combined displacements, velocities and accelerations may be measured, obtained by the following equation:

$$\mathbf{y}(t) = \mathbf{S}_y \begin{bmatrix} \mathbf{u}(t) \\ \dot{\mathbf{u}}(t) \\ \ddot{\mathbf{u}}(t) \end{bmatrix} = \begin{bmatrix} \mathbf{S}_d & \mathbf{0} & \mathbf{0} \\ \mathbf{0} & \mathbf{S}_v & \mathbf{0} \\ \mathbf{0} & \mathbf{0} & \mathbf{S}_a \end{bmatrix} \begin{bmatrix} \mathbf{u}(t) \\ \dot{\mathbf{u}}(t) \\ \ddot{\mathbf{u}}(t) \end{bmatrix} \tag{3.7}$$

in which $\mathbf{S}_d \in \mathbb{R}^{n_d \times n_{dof}}$, $\mathbf{S}_v \in \mathbb{R}^{n_v \times n_{dof}}$ and $\mathbf{S}_a \in \mathbb{R}^{n_a \times n_{dof}}$ are the selection matrices for displacements, velocities and accelerations respectively, concentrated in the output selection matrix $\mathbf{S}_y \in \mathbb{R}^{n_y \times 3n_{dof}}$. Making use of the equation of motion in nodal coordinates and the definition of the state vector $\mathbf{x}(t)$, the measurement vector can be rewritten into state-space form:

$$\mathbf{y}(t) = \mathbf{G}_c \mathbf{x}(t) + \mathbf{J}_c \mathbf{p}(t) \tag{3.8}$$

where the output influence matrix $\mathbf{G}_c \in \mathbb{R}^{n_y \times n_s}$ and the direct transmission matrix $\mathbf{J}_c \in \mathbb{R}^{n_y \times n_p}$ are defined as:

$$\mathbf{G}_c = \begin{bmatrix} \mathbf{S}_d & \mathbf{0} \\ \mathbf{0} & \mathbf{S}_v \\ -\mathbf{S}_a\mathbf{M}^{-1}\mathbf{K} & -\mathbf{S}_a\mathbf{M}^{-1}\mathbf{C} \end{bmatrix}, \quad \mathbf{J}_c = \begin{bmatrix} \mathbf{0} \\ \mathbf{0} \\ \mathbf{S}_a\mathbf{M}^{-1}\mathbf{S}_p \end{bmatrix}$$

Eqs. (3.6) and (3.8) together constitute the full-order state-space equations in the continuous-time domain. In the case of a reduced order model, the dynamics of the system may be represented by a reduced number n_m of modal coordinates $\mathbf{z}(t)$, so that the state vector can be written as:

$$\mathbf{x}(t) = \begin{bmatrix} \boldsymbol{\Phi} & \mathbf{0} \\ \mathbf{0} & \boldsymbol{\Phi} \end{bmatrix} \boldsymbol{\zeta}(t) \tag{3.9}$$

in which $\boldsymbol{\zeta}(t) \in \mathbb{R}^{2n_m}$ is the modal state vector:

$$\boldsymbol{\zeta}(t) = \begin{bmatrix} \mathbf{z}(t) \\ \dot{\mathbf{z}}(t) \end{bmatrix} \tag{3.10}$$

Accordingly, the full order state-space model is transformed to the modal state-space model of reduced order:

$$\dot{\boldsymbol{\zeta}}(t) = \mathbf{A}_\mathrm{c}\boldsymbol{\zeta}(t) + \mathbf{B}_\mathrm{c}\mathbf{p}(t) \tag{3.11}$$

$$\mathbf{y}(t) = \mathbf{G}_\mathrm{c}\boldsymbol{\zeta}(t) + \mathbf{J}_\mathrm{c}\mathbf{p}(t) \tag{3.12}$$

where the corresponding system matrices $\mathbf{A}_\mathrm{c} \in \mathbb{R}^{2n_\mathrm{m}\times 2n_\mathrm{m}}$, $\mathbf{B}_\mathrm{c} \in \mathbb{R}^{2n_\mathrm{m}\times n_\mathrm{p}}$, $\mathbf{G}_\mathrm{c} \in \mathbb{R}^{n_\mathrm{y}\times 2n_\mathrm{m}}$ and $\mathbf{J}_\mathrm{c} \in \mathbb{R}^{n_\mathrm{y}\times n_\mathrm{p}}$ are now defined as:

$$\mathbf{A}_\mathrm{c} = \begin{bmatrix} \mathbf{0} & \mathbf{I} \\ -\boldsymbol{\Omega}^2 & -\boldsymbol{\Gamma} \end{bmatrix}, \quad \mathbf{B}_\mathrm{c} = \begin{bmatrix} \mathbf{0} \\ \boldsymbol{\Phi}^\mathrm{T}\mathbf{S}_\mathrm{p} \end{bmatrix}, \quad \mathbf{G}_\mathrm{c} = \begin{bmatrix} \mathbf{S}_\mathrm{d}\boldsymbol{\Phi} & \mathbf{0} \\ \mathbf{0} & \mathbf{S}_\mathrm{v}\boldsymbol{\Phi} \\ -\mathbf{S}_\mathrm{a}\boldsymbol{\Phi}\boldsymbol{\Omega}^2 & -\mathbf{S}_\mathrm{a}\boldsymbol{\Phi}\boldsymbol{\Gamma} \end{bmatrix}, \quad \mathbf{J}_\mathrm{c} = \begin{bmatrix} \mathbf{0} \\ \mathbf{0} \\ \mathbf{S}_\mathrm{a}\boldsymbol{\Phi}\,\boldsymbol{\Phi}^\mathrm{T}\mathbf{S}_\mathrm{p} \end{bmatrix}$$

3.2.2 Discrete-time domain

For a sampling rate of $1/\Delta t$, the modal state-space model of Eqs. (3.11) and (3.12) can be transformed to its equivalent discrete-time model:

$$\boldsymbol{\zeta}_{k+1} = \mathbf{A}\boldsymbol{\zeta}_k + \mathbf{B}\mathbf{p}_k \tag{3.13}$$

$$\mathbf{y}_k = \mathbf{G}\boldsymbol{\zeta}_k + \mathbf{J}\mathbf{p}_k \tag{3.14}$$

where $\boldsymbol{\zeta}_k = \boldsymbol{\zeta}(k\Delta t)$, $\mathbf{p}_k = \mathbf{p}(k\Delta t)$, $\mathbf{y}_k = \mathbf{y}(k\Delta t)$ for $k = 1, 2, ..., \mathrm{N}_t$ and

$$\mathbf{A} = e^{\mathbf{A}_\mathrm{c}\Delta t}, \quad \mathbf{B} = [\mathbf{A} - \mathbf{I}]\,\mathbf{A}_\mathrm{c}^{-1}\mathbf{B}_\mathrm{c}, \quad \mathbf{G} = \mathbf{G}_\mathrm{c}, \quad \mathbf{J} = \mathbf{J}_\mathrm{c}$$

3.3 Stochastic Subspace Identification

3.3.1 Problem description

The discretized in time state-space model of Eqs. (3.13) and (3.14) constitutes the starting point for OMA by means of the subspace identification algorithms. Within this context, the only available information is the set of outputs $\mathbf{y}_k$ which is though contaminated with a measurement error. In this sense, the state-space model under consideration may be extended to the following form:

$$\boldsymbol{\zeta}_{k+1} = \mathbf{A}\boldsymbol{\zeta}_k + \mathbf{B}\mathbf{p}_k \tag{3.15}$$

$$\mathbf{y}_k = \mathbf{G}\boldsymbol{\zeta}_k + \mathbf{J}\mathbf{p}_k + \mathbf{e}_k \tag{3.16}$$

in which $\mathbf{e}_k \in \mathbb{R}^{n_\mathrm{y}}$ denotes the measurement error. Considering that little information with respect to the latter and the loading $\mathbf{p}_k$ is available, they can be both modelled as white noise random processes. It should be mentioned though that such an assumption may be violated when the excitation spectrum is dominated by certain frequency components.

With these considerations, the state-space model given by Eqs. (3.15) and (3.16) can be now reformulated as:

$$\boldsymbol{\zeta}_{k+1} = \mathbf{A}\boldsymbol{\zeta}_k + \mathbf{w}_k \tag{3.17}$$

$$\mathbf{y}_k = \mathbf{G}\boldsymbol{\zeta}_k + \mathbf{v}_k \tag{3.18}$$

where $\mathbf{w}_k = \mathbf{B}\mathbf{p}_k$ and $\mathbf{v}_k = \mathbf{J}\mathbf{p}_k + \mathbf{e}_k$ denote the process noise and the output noise, respectively. The corresponding covariance matrices are defined:

$$\mathbb{E}\left[\begin{bmatrix}\mathbf{w}_p \\ \mathbf{v}_p\end{bmatrix}\begin{bmatrix}\mathbf{w}_q^{\mathrm{T}} & \mathbf{v}_q^{\mathrm{T}}\end{bmatrix}\right] = \begin{bmatrix}\mathbf{Q} & \mathbf{S} \\ \mathbf{S}^{\mathrm{T}} & \mathbf{R}\end{bmatrix}\delta_{pq} \tag{3.19}$$

where $\mathbf{Q} \in \mathbb{R}^{2n_\mathrm{m}\times 2n_\mathrm{m}}$, $\mathbf{S} \in \mathbb{R}^{2n_\mathrm{m}\times n_y}$ and $\mathbf{R} \in \mathbb{R}^{n_y\times n_y}$ are time-invariant and δ_{pq} denotes the Kronecker delta. A graphical representation of the stochastic system described by Eqs. (3.17) and (3.18) is shown in Figure 3.1.

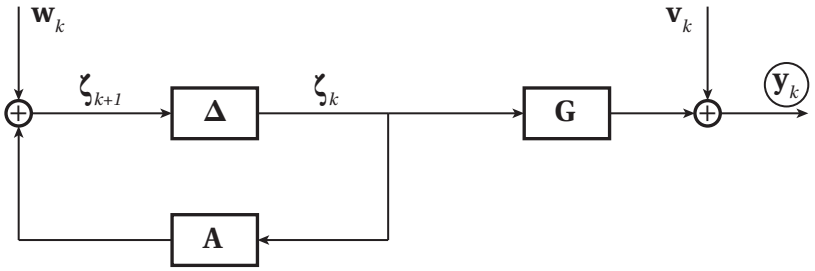

Figure 3.1: Linear time-invariant stochastic system with the output $\mathbf{y}_k$ being the only measured quantity and with symbol Δ denoting the time delay

Now that all aspects of the models under consideration are described, the SSI problem can be formulated as follows: Given s measurements of the output vector $\mathbf{y}_k$ produced by the sought for stochastic system of order $2n_\mathrm{m}$ described by Eqs. (3.17), (3.18) and (3.19), determine:

- The order $2n_\mathrm{m}$ of the unknown system
- The system matrices $\mathbf{A} \in \mathbb{R}^{2n_\mathrm{m}\times 2n_\mathrm{m}}$, $\mathbf{G} \in \mathbb{R}^{n_y\times 2n_\mathrm{m}}$ up to within a similarity transformation and $\mathbf{Q} \in \mathbb{R}^{2n_\mathrm{m}\times 2n_\mathrm{m}}$, $\mathbf{S} \in \mathbb{R}^{2n_\mathrm{m}\times n_y}$, $\mathbf{R} \in \mathbb{R}^{n_y\times n_y}$ so that the second order statistics of the output of the model to be identified are equal to the observed output measurements.

3.3.2 Properties of stochastic state-space models

Apart from the statistical properties referring to the process and the output noise, the state-space model described by Eqs. (3.17) and (3.18) is assumed to be stationary, so that:

$$\mathbb{E}\left[\boldsymbol{\zeta}_k\right] = 0 \tag{3.20}$$

$$\mathbb{E}\left[\boldsymbol{\zeta}_k\boldsymbol{\zeta}_k^{\mathrm{T}}\right] = \boldsymbol{\Sigma} \tag{3.21}$$

where it should be noticed that the state covariance matrix $\mathbf{\Sigma} \in \mathbb{R}^{2n_\mathrm{m} \times 2n_\mathrm{m}}$ is not indexed due to its independence of time. It is implied therefore that matrix $\mathbf{A}$ is stable and as a consequence all of its poles are within the unit circle.

Considering that according to their definition, $\mathbf{w}_k$ and $\mathbf{v}_k$ are zero mean white noise processes, independent of the state vector $\boldsymbol{\zeta}_k$, two additional relations may be written:

$$\mathbb{E}\left[\boldsymbol{\zeta}_k \mathbf{v_k}^\mathrm{T}\right] = 0 \tag{3.22}$$

$$\mathbb{E}\left[\boldsymbol{\zeta}_k \mathbf{w_k}^\mathrm{T}\right] = 0 \tag{3.23}$$

The Lyapunov equation for the state covariance $\mathbf{\Sigma}$ of Eq. (3.21) is then written as:

$$\begin{aligned}
\mathbf{\Sigma} &= \mathbb{E}\left[\boldsymbol{\zeta}_{k+1}\boldsymbol{\zeta}_{k+1}^\mathrm{T}\right] \\
&= \mathbb{E}\left[\left(\mathbf{A}\boldsymbol{\zeta}_k + \mathbf{w}_k\right)\left(\mathbf{A}\boldsymbol{\zeta}_k + \mathbf{w}_k\right)^\mathrm{T}\right] \\
&= \mathbf{A}\mathbb{E}\left[\boldsymbol{\zeta}_k\boldsymbol{\zeta}_k^\mathrm{T}\right]\mathbf{A}^\mathrm{T} + \mathbb{E}\left[\mathbf{w}_k\mathbf{w}_k^\mathrm{T}\right] \\
&= \mathbf{A}\mathbf{\Sigma}\mathbf{A}^\mathrm{T} + \mathbf{Q}
\end{aligned} \tag{3.24}$$

while the state-output covariance matrix $\mathbf{F} \in \mathbb{R}^{2n_\mathrm{m} \times n_\mathrm{y}}$ is given by definition from:

$$\begin{aligned}
\mathbf{F} &= \mathbb{E}\left[\boldsymbol{\zeta}_{k+1}\mathbf{y}_k{}^\mathrm{T}\right] \\
&= \mathbb{E}\left[\left(\mathbf{A}\boldsymbol{\zeta}_k + \mathbf{w}_k\right)\left(\mathbf{G}\boldsymbol{\zeta}_k + \mathbf{v}_k\right)^\mathrm{T}\right] \\
&= \mathbf{A}\mathbb{E}\left[\boldsymbol{\zeta}_k\boldsymbol{\zeta}_k^\mathrm{T}\right]\mathbf{G}^\mathrm{T} + \mathbb{E}\left[\mathbf{w}_k\mathbf{v}_k^\mathrm{T}\right] \\
&= \mathbf{A}\mathbf{\Sigma}\mathbf{G}^\mathrm{T} + \mathbf{S}
\end{aligned} \tag{3.25}$$

Finally, the output covariance $\mathbf{\Lambda}_l \in \mathbb{R}^{n_\mathrm{y} \times n_\mathrm{y}}$ for $l = 1, 2, \ldots$ is defined as:

$$\mathbf{\Lambda}_l = \mathbb{E}\left[\mathbf{y}_{k+l}\mathbf{y}_k^\mathrm{T}\right] \tag{3.26}$$

which for $l = 0$ yields:

$$\begin{aligned}
\mathbf{\Lambda}_0 &= \mathbb{E}\left[\mathbf{y}_k\mathbf{y}_k^\mathrm{T}\right] \\
&= \mathbb{E}\left[\left(\mathbf{G}\boldsymbol{\zeta}_k + \mathbf{v}_k\right)\left(\mathbf{G}\boldsymbol{\zeta}_k + \mathbf{v}_k\right)^\mathrm{T}\right] \\
&= \mathbf{G}\mathbb{E}\left[\boldsymbol{\zeta}_k\boldsymbol{\zeta}_k^\mathrm{T}\right]\mathbf{G}^\mathrm{T} + \mathbb{E}\left[\mathbf{v}_k\mathbf{v}_k^\mathrm{T}\right] \\
&= \mathbf{G}\mathbf{\Sigma}\mathbf{G}^\mathrm{T} + \mathbf{R}
\end{aligned} \tag{3.27}$$

It can then be proven by induction that $\mathbf{\Lambda}_l$ for $l = 1, 2, \ldots$ is given by:

$$\mathbf{\Lambda}_l = \mathbf{G}\mathbf{A}^{l-1}\mathbf{F} \tag{3.28}$$

The starting point for the implementation of the subspace identification algorithms for stochastic state-space models is the concentration of the output measurements in a block

Hankel matrix (a matrix in which each ascending skew-diagonal from left to right is constant):

$$\mathbf{Y}_{0|2i-1} = \frac{1}{\sqrt{j}} \left[\begin{array}{cccc} \mathbf{y}_0 & \mathbf{y}_1 & \cdots & \mathbf{y}_{j-1} \\ \mathbf{y}_1 & \mathbf{y}_2 & \cdots & \mathbf{y}_j \\ \vdots & \vdots & \ddots & \vdots \\ \mathbf{y}_{i-1} & \mathbf{y}_i & \cdots & \mathbf{y}_{i+j-2} \\ \hline \mathbf{y}_i & \mathbf{y}_{i+1} & \cdots & \mathbf{y}_{i+j-1} \\ \mathbf{y}_{i+1} & \mathbf{y}_{i+2} & \cdots & \mathbf{y}_{i+j} \\ \vdots & \vdots & \ddots & \vdots \\ \mathbf{y}_{2i-1} & \mathbf{y}_{2i} & \cdots & \mathbf{y}_{2i+j-2} \end{array}\right] = \left[\begin{array}{c} \mathbf{Y}_{0|i-1} \\ \hline \mathbf{Y}_{i|2i-1} \end{array}\right] = \left[\begin{array}{c} \mathbf{Y}_\mathrm{p} \\ \hline \mathbf{Y}_\mathrm{f} \end{array}\right] \begin{array}{c} \text{"past"} \\ \hline \text{"future"} \end{array} \in \mathbb{R}^{2n_\mathrm{y} i \times j} \tag{3.29}$$

The index i which determines the number of block rows is a user-defined variable and should be equal to or greater than the maximum expected order of the system to be identified. Statistically, the number of columns j and the number of samples s should tend to infinity. However, considering the computational restrictions and in order to make use of all available measurement data, j is chosen to be equal to $s-2i+1$. Furthermore, it should be noticed that the subscripts of the block Hankel matrices $\mathbf{Y}_{0|2i-1}$, $\mathbf{Y}_{0|i-1}$ and $\mathbf{Y}_{i|2i-1}$ represent the first and the last block-element of the first column of the matrix they pertain to.

Accordingly, the shifted block Hankel matrix of the output measurements is obtained by shifting the border between past and future downwards by one block row. Therefore, Eq. (3.29) may be rewritten as:

$$\mathbf{Y}_{0|2i-1} = \frac{1}{\sqrt{j}} \left[\begin{array}{cccc} \mathbf{y}_0 & \mathbf{y}_1 & \cdots & \mathbf{y}_{j-1} \\ \mathbf{y}_1 & \mathbf{y}_2 & \cdots & \mathbf{y}_j \\ \vdots & \vdots & \ddots & \vdots \\ \mathbf{y}_{i-1} & \mathbf{y}_i & \cdots & \mathbf{y}_{i+j-2} \\ \mathbf{y}_i & \mathbf{y}_{i+1} & \cdots & \mathbf{y}_{i+j-1} \\ \hline \mathbf{y}_{i+1} & \mathbf{y}_{i+2} & \cdots & \mathbf{y}_{i+j} \\ \vdots & \vdots & \ddots & \vdots \\ \mathbf{y}_{2i-1} & \mathbf{y}_{2i} & \cdots & \mathbf{y}_{2i+j-2} \end{array}\right] = \left[\begin{array}{c} \mathbf{Y}_{0|i} \\ \hline \mathbf{Y}_{i+1|2i-1} \end{array}\right] = \left[\begin{array}{c} \mathbf{Y}_\mathrm{p}^+ \\ \hline \mathbf{Y}_\mathrm{f}^- \end{array}\right] \begin{array}{c} \text{"past"} \\ \hline \text{"future"} \end{array} \in \mathbb{R}^{2n_\mathrm{y} i \times j} \tag{3.30}$$

where $\mathbf{Y}_\mathrm{p}^+ \in \mathbb{R}^{n_\mathrm{y}(i+1)\times j}$ and $\mathbf{Y}_\mathrm{f}^- \in \mathbb{R}^{n_\mathrm{y}(i-1)\times j}$ are the corresponding shifted block Hankel matrices for the "past" and "future" outputs, with the subscript "+" denoting "add one block row" and the subscript "-" standing for "eliminate one block row".

3.3.3 Covariance-driven algorithm

As denoted by its name, the SSI-Cov algorithm utilizes the output covariance matrix in order to identify the sought for stochastic state-space model. Namely, the output covariance matrices $\mathbf{\Lambda}_l$ for time lags between Δt and $(2i-1)\Delta t$, or equally for $l = 1, 2, ..., 2i-1$, are evaluated and organized in a $n_\mathrm{y} i \times n_\mathrm{y} i$ block Toeplitz matrix:

$$\mathbf{L}_{1|i} = \begin{bmatrix} \mathbf{\Lambda}_i & \mathbf{\Lambda}_{i-1} & \cdots & \mathbf{\Lambda}_1 \\ \mathbf{\Lambda}_{i+1} & \mathbf{\Lambda}_i & \cdots & \mathbf{\Lambda}_2 \\ \vdots & \vdots & \ddots & \vdots \\ \mathbf{\Lambda}_{2i-1} & \mathbf{\Lambda}_{2i-2} & \cdots & \mathbf{\Lambda}_i \end{bmatrix} \in \mathbb{R}^{n_\mathrm{y} i \times n_\mathrm{y} i} \tag{3.31}$$

which, under the assumption of ergodicity, can be readily obtained, by making use of Eq. (3.29) from the following relation:

$$\mathbf{L}_{1|i} = \mathbf{Y}_\mathrm{f} \mathbf{Y}_\mathrm{p}^\mathrm{T} \tag{3.32}$$

Alternatively, the output covariance matrices can be evaluated separately from the following formula:

$$\mathbf{\Lambda}_l = \frac{1}{s-l} \sum_{k=0}^{s-l-1} \mathbf{y}_{k+l} \mathbf{y}_k^\mathrm{T} \tag{3.33}$$

in which s denotes the number of points of the time series and they can be then assigned to the corresponding positions of the Toeplitz matrix. An illustration of this process is presented in Fig. 3.2 where the $n_\mathrm{y} \times n_\mathrm{y}$ covariance matrices (Fig. 3.2(a)) are stored in the $n_\mathrm{y} i \times n_\mathrm{y} i$ block Toeplitz matrix (Fig. 3.2(b)). It should be noticed at this point that a Toeplitz matrix is matrix in which each descending diagonal from left to right is constant.

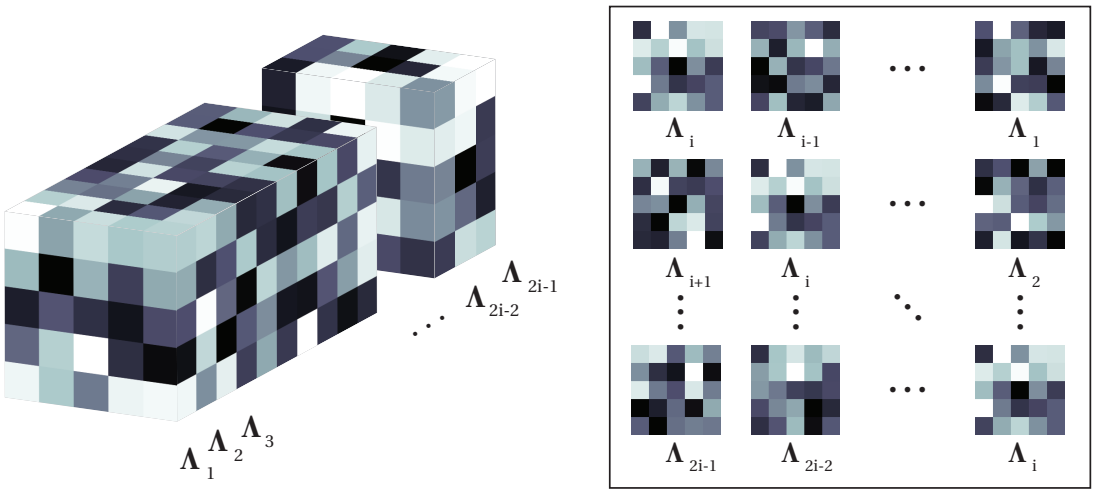

(a) Covariance matrix (b) Block Toeplitz matrix

Figure 3.2: Construction of the block Toeplitz matrix

The block Toeplitz matrix $\mathbf{L}_{1|i}$ can be decomposed, upon utilization of Eq. (3.28) for the output covariance matrix, in the product of the following matrices:

$$\mathbf{L}_{1|i} = \begin{bmatrix} \mathbf{G} \\ \mathbf{GA} \\ \vdots \\ \mathbf{GA}^{i-1} \end{bmatrix} \begin{bmatrix} \mathbf{A}^{i-1}\mathbf{F} & \cdots & \mathbf{AF} & \mathbf{F} \end{bmatrix} = \mathbf{O}\,\mathbf{C}_\mathrm{r} \tag{3.34}$$

with $\mathbf{O} \in \mathbb{R}^{n_\mathrm{y} i \times 2n_\mathrm{m}}$ and $\mathbf{C}_\mathrm{r} \in \mathbb{R}^{2n_\mathrm{m} \times n_\mathrm{y} i}$ denoting the extended observability matrix and the

reversed extended controllability matrix respectively. These can be retrieved by applying the Singular Value Decomposition (SVD) to the block Toeplitz matrix:

$$\mathbf{L}_{1|i} = \mathbf{U}\mathbf{S}\mathbf{V}^{\mathrm{T}} = \begin{bmatrix}\mathbf{U}_1 & \mathbf{U}_2\end{bmatrix}\begin{bmatrix}\mathbf{S}_1 & \mathbf{0}\\ \mathbf{0} & \mathbf{0}\end{bmatrix}\begin{bmatrix}\mathbf{V}_1^{\mathrm{T}}\\ \mathbf{V}_2^{\mathrm{T}}\end{bmatrix} = \mathbf{U}_1\mathbf{S}_1\mathbf{V}_1^{\mathrm{T}} \tag{3.35}$$

where $\mathbf{U} \in \mathbb{R}^{n_y i \times n_y i}$ and $\mathbf{U} \in \mathbb{R}^{n_y i \times n_y i}$ are orthonormal matrices, with $\mathbf{U}^{\mathrm{T}}\mathbf{U} = \mathbf{U}\mathbf{U}^{\mathrm{T}} = \mathbf{I} \in \mathbb{R}^{n_y i \times n_y i}$ and $\mathbf{V}^{\mathrm{T}}\mathbf{V} = \mathbf{V}\mathbf{V}^{\mathrm{T}} = \mathbf{I} \in \mathbb{R}^{n_y i \times n_y i}$, and $\mathbf{S} \in \mathbb{R}^{n_y i \times n_y i}$ is a diagonal matrix containing the singular values. It should be noticed at this point that the rank of matrix is indicated by the number of its non-zero singular values. Omitting thus the zero singular values of matrix $\mathbf{S}$, and collecting the non-zero ones in matrix $\mathbf{S}_1$ as illustrated in Eq. (3.35), the block Toeplitz matrix can be expressed as a function of $\mathbf{U}_1$, $\mathbf{S}_1$ and $\mathbf{V}_1$ and it can be stated that:

$$\mathbf{O} = \mathbf{U}_1\mathbf{S}_1^{1/2} \tag{3.36}$$

$$\mathbf{C}_{\mathrm{r}} = \mathbf{S}_1^{1/2}\mathbf{V}_1^{\mathrm{T}} \tag{3.37}$$

Once the observability and controllability matrices are obtained, the identification of the system matrices $\mathbf{A}$ and $\mathbf{G}$ is straightforward. Concretely, matrix $\mathbf{G}$ equals the first n_y rows of the observability matrix and matrix $\mathbf{A}$ is obtained by the solution of the Least Squares (LS) problem described by the following equation:

$$\begin{bmatrix}\mathbf{G}\\ \mathbf{G}\mathbf{A}\\ \vdots\\ \mathbf{G}\mathbf{A}^{i-2}\end{bmatrix}\mathbf{A} = \begin{bmatrix}\mathbf{G}\mathbf{A}\\ \mathbf{G}\mathbf{A}^2\\ \vdots\\ \mathbf{G}\mathbf{A}^{i-1}\end{bmatrix} \quad \Leftrightarrow \quad \mathbf{A} = \begin{bmatrix}\mathbf{G}\\ \mathbf{G}\mathbf{A}\\ \vdots\\ \mathbf{G}\mathbf{A}^{i-2}\end{bmatrix}^{\dagger}\begin{bmatrix}\mathbf{G}\mathbf{A}\\ \mathbf{G}\mathbf{A}^2\\ \vdots\\ \mathbf{G}\mathbf{A}^{i-1}\end{bmatrix} = \underline{\mathbf{O}}^{\dagger}\,\overline{\mathbf{O}} \tag{3.38}$$

where the symbol $(\bullet)^{\dagger}$ denotes the Moore-Penrose pseudo-inverse, which for a matrix $\mathbf{M}$ may be obtained by the expression $\mathbf{M}^{\dagger} = \left(\mathbf{M}^{\mathrm{T}}\mathbf{M}\right)^{-1}\mathbf{M}^{\mathrm{T}}$, while $\underline{\mathbf{O}}$ contains the first $n_y(i-1)$ rows of $\mathbf{O}$ and $\overline{\mathbf{O}}$ contains the last $n_y(i-1)$ rows of $\mathbf{O}$.

3.3.4 Data-driven algorithm

The main idea behind the SSI-Data algorithm is to retrieve the system matrices $\mathbf{A}$, $\mathbf{G}$, and subsequently the modal properties of the stochastic state-space model, using the raw time histories of the output block Hankel matrix (3.29). In doing so, it is essential that the notion of Kalman filter estimates is first introduced.

The problem addressed by the Kalman filter is to estimate the state $\hat{\boldsymbol{\zeta}}_k$ of the system described by Eq. (3.17) using the measurement vector $\mathbf{y}_k$ given by Eq. (3.18). Within this context, the *a priori* state estimate at step k given knowledge of the process prior to step k is defined as $\hat{\boldsymbol{\zeta}}_k^-$ and the *a posteriori* state estimate at step k given measurement $\mathbf{y}_k$ is denoted by $\hat{\boldsymbol{\zeta}}_k$. Accordingly, the *a priori* and *a posteriori* estimate errors are respectively defined as:

$$\mathbf{e}_k^- = \boldsymbol{\zeta}_k - \hat{\boldsymbol{\zeta}}_k^- \tag{3.39}$$

$$\mathbf{e}_k = \boldsymbol{\zeta}_k - \hat{\boldsymbol{\zeta}}_k \tag{3.40}$$

Likewise, the *a priori* and *a posteriori* estimate error covariances denoted by $\mathbf{P}_k^-$ and $\mathbf{P}_k$ are

given by the following equations:

$$\mathbf{P}_k^- = \mathbb{E}\left[\mathbf{e}_k^- \mathbf{e}_k^{\mathrm{T}}\right] = \mathbb{E}\left[\left(\boldsymbol{\zeta}_k - \hat{\boldsymbol{\zeta}}_k^-\right)\left(\boldsymbol{\zeta}_k - \hat{\boldsymbol{\zeta}}_k^-\right)^{\mathrm{T}}\right] \tag{3.41}$$

$$\mathbf{P}_k = \mathbb{E}\left[\mathbf{e}_k \mathbf{e}_k^{\mathrm{T}}\right] = \mathbb{E}\left[\left(\boldsymbol{\zeta}_k - \hat{\boldsymbol{\zeta}}_k\right)\left(\boldsymbol{\zeta}_k - \hat{\boldsymbol{\zeta}}_k\right)^{\mathrm{T}}\right] \tag{3.42}$$

Now, the derivation of the Kalman filter equations is based on finding an equation that computes an *a posteriori* state estimate $\hat{\boldsymbol{\zeta}}_k$ as a linear combination of an *a priori* estimate $\hat{\boldsymbol{\zeta}}_k^-$ and a weighted difference between the actual measurement $\mathbf{y}_k$ and the measurement prediction $\hat{\mathbf{y}}_k$. This is formulated by the equation:

$$\hat{\boldsymbol{\zeta}}_k = \hat{\boldsymbol{\zeta}}_k^- + \mathbf{K}_k\left(\mathbf{y}_k - \mathbf{G}\hat{\boldsymbol{\zeta}}_k^-\right) \tag{3.43}$$

where the term in parenthesis is called the measurement innovation, or the residual. The matrix $\mathbf{K}_k \in \mathbb{R}^{2n_{\mathrm{m}} \times n_{\mathrm{y}}}$ is the Kalman gain that minimizes the *a posteriori* error covariance, which reads:

$$\mathbf{K}_k = \mathbf{P}_k^- \mathbf{G}^{\mathrm{T}}\left(\mathbf{G}\mathbf{P}_k^- \mathbf{G}^{\mathrm{T}} + \mathbf{R}\right)^{-1} \tag{3.44}$$

As illustrated by Eqs. (3.43) and (3.44), the Kalman filter estimates a process by using a form of feedback control in terms of the estimation of the state at some time and the feedback in the form of noisy measurements. In this sense, the Kalman filter equations can be split into two groups, the time update equations and the measurement update equations. The first group is responsible for the forward projection of the current state and error covariance estimates in order to obtain the a priori estimates of the next time step. The latter group provides the feedback in terms of the incorporation of the new measurement into the a priori estimate in order to yield the improved a posteriori estimate.

Time update equations

$$\hat{\boldsymbol{\zeta}}_k^- = \mathbf{A}\hat{\boldsymbol{\zeta}}_{k-1} \tag{3.45}$$

$$\mathbf{P}_k^- = \mathbf{A}\mathbf{P}_{k-1}\mathbf{A}^{\mathrm{T}} + \mathbf{Q} \tag{3.46}$$

Measurement update equations

$$\mathbf{K}_k = \mathbf{P}_k^- \mathbf{G}^{\mathrm{T}}\left(\mathbf{G}\mathbf{P}_k^- \mathbf{G}^{\mathrm{T}} + \mathbf{R}\right)^{-1} \tag{3.47}$$

$$\hat{\boldsymbol{\zeta}}_k = \hat{\boldsymbol{\zeta}}_k^- + \mathbf{K}_k\left(\mathbf{y}_k - \mathbf{G}\hat{\boldsymbol{\zeta}}_k^-\right) \tag{3.48}$$

$$\mathbf{P}_k = \left(\mathbf{I} - \mathbf{K}_k\mathbf{G}\right)\mathbf{P}_k^- \tag{3.49}$$

In detail, the initialization of the process requires the initial state $\hat{\boldsymbol{\zeta}}_0$ and its variance $\mathbf{P}_0$. Hereafter, use of the time update equations, namely Eqs. (3.45) - (3.46), yields the *a priori* estimation $\hat{\boldsymbol{\zeta}}_1^-$ of the state and its variance $\mathbf{P}_1^-$ for $k = 1$, corresponding to the first time step. Once the first measurement data $\mathbf{y}_1$ is available, the second set of equations, (3.47), (3.48) and (3.49), is then used to produce an improved *a posteriori* estimation of both the state $\hat{\boldsymbol{\zeta}}_1^-$ and its variance $\mathbf{P}_1$. Hence, after each time and measurement update pair, the *a posteriori* estimates are used to project the new *a priori* estimates of the next step and so forth. Within the framework of the SSI-Data, the Kalman filter estimates, which are aimed to be recovered,

are collected in the Kalman filter sequence $\hat{\mathbf{Z}}_i$ which reads:

$$\hat{\mathbf{Z}}_i = \begin{bmatrix} \hat{\boldsymbol{\zeta}}_i & \hat{\boldsymbol{\zeta}}_{i+1} & \dots & \hat{\boldsymbol{\zeta}}_{i+j-1} \end{bmatrix} \in \mathbb{R}^{n_\mathrm{y} \times j} \tag{3.50}$$

For the computationally-efficient performance of the algorithm, the block Hankel matrix of Eq. (3.29) is decomposed through the QR-factorisation:

$$\mathbf{Y}_{0|2i-1} = \left[\frac{\mathbf{Y}_\mathrm{p}}{\mathbf{Y}_\mathrm{f}}\right] = \tilde{\mathbf{R}}\tilde{\mathbf{Q}}^\mathrm{T} \tag{3.51}$$

where $\tilde{\mathbf{Q}} \in \mathbb{R}^{j \times j}$ is an orthonormal matrix $\tilde{\mathbf{Q}}^\mathrm{T}\tilde{\mathbf{Q}} = \tilde{\mathbf{Q}}\tilde{\mathbf{Q}}^\mathrm{T} = \mathbf{I}$ and $\tilde{\mathbf{R}} \in \mathbb{R}^{2n_\mathrm{y} i}$ is a lower-triangular matrix. It should be noticed that the advantage of this factorisation consists in the orthonormality of the $\tilde{\mathbf{Q}}$ vectors which will lead to a significant data reduction. Moreover, in order to fit in the notation used for the "past" and "future" outputs, the factorised block Hankel matrix of Eq. (3.51) can be rewritten as:

$$\mathbf{Y}_{0|2i-1} = \begin{array}{c} \\ n_\mathrm{y} i \\ n_\mathrm{y} \\ n_\mathrm{y}(i-1) \end{array} \begin{array}{c} \begin{array}{cccc} n_\mathrm{y} i & n_\mathrm{y} & n_\mathrm{y}(i-1) & j \end{array} \\ \begin{bmatrix} \tilde{\mathbf{R}}_{11} & \mathbf{0} & \mathbf{0} \\ \tilde{\mathbf{R}}_{21} & \tilde{\mathbf{R}}_{22} & \mathbf{0} \\ \tilde{\mathbf{R}}_{31} & \tilde{\mathbf{R}}_{32} & \tilde{\mathbf{R}}_{33} \end{bmatrix} \end{array} \begin{array}{c} \\ \begin{bmatrix} \tilde{\mathbf{Q}}_1^\mathrm{T} \\ \tilde{\mathbf{Q}}_2^\mathrm{T} \\ \tilde{\mathbf{Q}}_3^\mathrm{T} \end{bmatrix} \end{array} \begin{array}{c} \\ n_\mathrm{y} i \\ n_\mathrm{y} \\ n_\mathrm{y}(i-1) \end{array} \tag{3.52}$$

Apart from the Kalman filter estimates, projections are the second key element of the SSI and the SSI-Data algorithm specifically. Hence, the projection of the row space of the future outputs into the row space of the past outputs reads:

$$\mathscr{P}_i = \mathbf{Y}_\mathrm{f} / \mathbf{Y}_\mathrm{p} = \mathbf{Y}_\mathrm{f} \mathbf{Y}_\mathrm{p}^\mathrm{T} \left(\mathbf{Y}_\mathrm{p} \mathbf{Y}_\mathrm{p}^\mathrm{T} \right)^\dagger \mathbf{Y}_\mathrm{p} \tag{3.53}$$

Upon introduction of the QR-factorisation of the output Hankel matrix into the above equation, the projection may be simplified to the following expression:

$$\mathscr{P}_i = \begin{bmatrix} \tilde{\mathbf{R}}_{21} \\ \tilde{\mathbf{R}}_{31} \end{bmatrix} \tilde{\mathbf{Q}}_1^\mathrm{T} \in \mathbb{R}^{n_\mathrm{y} i \times j} \tag{3.54}$$

Then according to the main theorem of the SSI stated by Van Overschee and De Moore (1996), the projection $\mathscr{P}_i$ of the future outputs into the row space of the past outputs can be decomposed into the product of the observability matrix $\mathbf{O} \in \mathbb{R}^{2n_\mathrm{y} i \times n_\mathrm{m}}$ and the Kalman filter sequence:

$$\mathscr{P}_i = \mathbf{O}\hat{\mathbf{Z}}_i = \begin{bmatrix} \mathbf{G} \\ \mathbf{GA} \\ \vdots \\ \mathbf{GA}^{i-1} \end{bmatrix} \begin{bmatrix} \hat{\boldsymbol{\zeta}}_i & \hat{\boldsymbol{\zeta}}_{i+1} & \dots & \hat{\boldsymbol{\zeta}}_{i+j-1} \end{bmatrix} \tag{3.55}$$

In this sense, both matrices can be retrieved by working in the same way as previously done for the covariance Toeplitz matrix $\mathbf{L}_{1|i}$, with application of the SVD to the already known

projection matrix:

$$\mathscr{P}_i = \mathbf{U}\mathbf{S}\mathbf{V}^{\mathrm{T}} = \begin{bmatrix}\mathbf{U}_1 & \mathbf{U}_2\end{bmatrix}\begin{bmatrix}\mathbf{S}_1 & \mathbf{0}\\ \mathbf{0} & \mathbf{0}\end{bmatrix}\begin{bmatrix}\mathbf{V}_1^{\mathrm{T}}\\ \mathbf{V}_2^{\mathrm{T}}\end{bmatrix} = \mathbf{U}_1\mathbf{S}_1\mathbf{V}_1^{\mathrm{T}} \tag{3.56}$$

Again, considering that the rank of the projection matrix is indicated by its non-zero singular values, the order of the sought-for stochastic state-space model is represented by the number of the diagonal entries that are contained in matrix $\mathbf{S}_1$. The observability matrix and the Kalman filter sequence can be therefore obtained by the following expression:

$$\mathbf{O} = \mathbf{U}_1\mathbf{S}_1^{1/2} \tag{3.57}$$

$$\hat{\mathbf{Z}}_i = \mathbf{O}^{\dagger}\mathscr{P}_i \tag{3.58}$$

Knowledge of the observability matrix and the Kalman filter sequence is sufficient for the determination of the system matrices **A** and **G** as well as the covariance matrices **Q**, **R** and **S**. This task is based on the projection of the row space of the shifted "future" outputs into the row space of the shifted "past" outputs:

$$\mathscr{P}_{i-1} = \mathbf{Y}_{\mathrm{f}}^{-} \,/\, \mathbf{Y}_{\mathrm{p}}^{+} = \begin{bmatrix}\tilde{\mathbf{R}}_{31} & \tilde{\mathbf{R}}_{32}\end{bmatrix}\begin{bmatrix}\tilde{\mathbf{Q}}_1^{\mathrm{T}}\\ \tilde{\mathbf{Q}}_2^{\mathrm{T}}\end{bmatrix} \in \mathbb{R}^{n_{\mathrm{y}}(i-1)\times j} \tag{3.59}$$

which can be accordingly factorised as the product of the shifted observability matrix $\underline{\mathbf{O}} \in \mathbb{R}^{n_{\mathrm{y}}(i-1)\times 2n_{\mathrm{m}}}$ that contains the first $n_{\mathrm{y}}(i-1)$ rows of **O** and the shifted Kalman filter sequence $\hat{\mathbf{Z}}_{i+1}$ according to:

$$\mathscr{P}_{i-1} = \underline{\mathbf{O}}\,\hat{\mathbf{Z}}_{i+1} \tag{3.60}$$

Subsequently, $\hat{\mathbf{Z}}_{i+1}$ can be obtained by solving the above equation in a LS sense, leading to the expression:

$$\hat{\mathbf{Z}}_{i+1} = \underline{\mathbf{O}}^{\dagger}\mathscr{P}_{i-1} \tag{3.61}$$

This enables the construction of the overdetermined set of linear equations that constitute an extension of Eqs. (3.17) and (3.18):

$$\begin{bmatrix}\hat{\mathbf{Z}}_{i+1}\\ \mathbf{Y}_{i|i}\end{bmatrix} = \begin{bmatrix}\mathbf{A}\\ \mathbf{G}\end{bmatrix}\hat{\mathbf{Z}}_i + \begin{bmatrix}\mathbf{e}_{\mathrm{w}}\\ \mathbf{e}_{\mathrm{v}}\end{bmatrix} \tag{3.62}$$

where $\mathbf{Y}_{i|i}$ is a one-block row Hankel matrix which can be readily calculated by making use of the already performed QR-factorisation from the following expression:

$$\mathbf{Y}_{i|i} = \begin{bmatrix}\tilde{\mathbf{R}}_{21} & \tilde{\mathbf{R}}_{22}\end{bmatrix}\begin{bmatrix}\tilde{\mathbf{Q}}_1^{\mathrm{T}}\\ \tilde{\mathbf{Q}}_2^{\mathrm{T}}\end{bmatrix} \in \mathbb{R}^{n_{\mathrm{y}}\times j} \tag{3.63}$$

Finally, knowledge of $\mathbf{Y}_{i|i}$ and the Kalman filter states sequence $\hat{\mathbf{Z}}_i$ enables the evaluation of the system matrices **A** and **G** through the solution of the LS problem described by Eq. (3.62):

$$\begin{bmatrix} \mathbf{A} \\ \mathbf{G} \end{bmatrix} = \begin{bmatrix} \hat{\mathbf{Z}}_{i+1} \\ \mathbf{Y}_{i|i} \end{bmatrix} \hat{\mathbf{Z}}_i^{\dagger} \tag{3.64}$$

3.3.5 Modal characteristics

Identification of the stochastic state-space model under consideration by means of matrices **A** and **G** is sufficient for the extraction of the modal properties. Namely, an eigenvalue decomposition of the matrix

$$\mathbf{A} = \sum_{k=1}^{2n_{\mathrm{m}}} \boldsymbol{\psi}_k \lambda_k \boldsymbol{\psi}_k \tag{3.65}$$

yields the discrete-time eigenvectors $\boldsymbol{\psi}_k$ and eigevalues λ_k. Considering that matrix **A** was obtained through the discretization of the continuous-time matrix $\mathbf{A}_{\mathrm{c}}$ with a sampling rate $1/\Delta t$:

$$\mathbf{A} = e^{\mathbf{A}_{\mathrm{c}} \Delta t} \tag{3.66}$$

the equivalent continuous-time eigenproperties can be retrieved by:

$$\boldsymbol{\psi}_{\mathrm{c}k} = \boldsymbol{\psi}_k, \qquad \lambda_{\mathrm{c}k} = \frac{\ln(\lambda_k)}{\Delta t} \tag{3.67}$$

Moreover, the eigenvalues of $\mathbf{A}_{\mathrm{c}}$ appear in complex conjugated pairs and can be written as:

$$\lambda_{\mathrm{c}k}, \lambda_{\mathrm{c}k}^{*} = -\xi_k \omega_k \pm \mathrm{j}\omega_k \sqrt{1-\xi_k^2} \tag{3.68}$$

with ξ_k and ω_k denoting the modal damping ratio and the eigenfrequency of mode k, respectively. The sought for natural frequencies f_k [Hz] and the damping ratios ξ_k (in % of critical) are then evaluated from :

$$f_k = \frac{|\lambda_{\mathrm{c}k}|}{2\pi} \tag{3.69}$$

$$\xi_k = -100 \frac{\mathrm{Re}(\lambda_{\mathrm{c}k})}{|\lambda_{\mathrm{c}k}|} \tag{3.70}$$

where $\mathrm{Re}(\bullet)$ represents the real part of a complex number. Finally, the mode shapes $\boldsymbol{\phi}_k$ in terms of the measured quantities can be obtained through the combination of the eigenvectors of **A** with matrix **G**:

$$\boldsymbol{\phi}_k = \mathbf{G}\boldsymbol{\psi}_k \tag{3.71}$$

It should be noticed at this point that due to the existence of these complex conjugate pairs, only the eigenvalues with positive imaginary part are selected for post-processing and therefore for a state-space model of order $2n_{\mathrm{m}}$ only n_{m} modal characteristics are identifiable.

3.3.6 Implementation and stabilization

In operational modal analysis, weight is not lent to the estimation of the state-space model as such, but rather to its modal properties. It is therefore of crucial importance that the order n_{m}

of the model is adequately determined, and the estimated modes represent the physical ones and not a set of numerical modes that only contributes to the modelling of noise.

It was shown that for both algorithms the order of the system is indicated by the number of non-zero singular values of matrices $\mathbf{L}_{1|i}$ and $\mathscr{P}_i$, for the SSI-Cov and SSI-Data algorithms respectively. Nonetheless, even the higher singular values that should be zero, in practice present some residual values due to the presence of noise in the system which is also reflected on the output measurements (Reynders et al., 2008). The existence of such noise is mainly due to:

- Modelling errors. Most systems present a non-linear behaviour which implies that the linear model described by Eqs. (3.17) - (3.18) cannot model the real structural response.
- Measurement noise introduced through the electronic devices of the sensor network.
- Computational noise caused by the finite computational precision.
- Finite number of data samples s, which implies that only an estimate of the system matrices can be obtained and not the real ones.

In such a case, one could determine the order n_{m} by detecting the maximum gap between two successive singular values. Even so, as underlined by Van Overschee and De Moore (1996), this gap may not be detectable in large and real structures, making hence difficult the decision of the system order.

The common practice to overcome this difficulty, is the use of the so-called stabilization diagram. The idea behind this diagram is to estimate models of varying orders within a predetermined interval and then separate the physical modes from the spurious ones. To this end, the SVD of either $\mathbf{L}_{1|i}$ or $\mathscr{P}_i$ is first determined and the maximum expected model order n_{x} is defined. Then, models starting from 2 up to n_{x} with successively increasing orders of 2 are estimated and the system matrices $\mathbf{A}$ and $\mathbf{G}$ are constructed by selecting the accordingly increased number of singular values and vectors of either $\mathbf{L}_{1|i}$ or $\mathscr{P}_i$, depending on the implemented algorithm.

The main idea behind this procedure is that the physical modes are expected to appear in most of these models with consistent frequency, mode shape and damping ratio while the numerical ones will only appear in some of them. The separation of physical and spurious modes is thus achieved by calculating the modal properties of a certain-order model and comparing them with the ones of a one-order-lower model. If then the frequency, mode shape and damping ratio differences are within preset limits, the mode is labelled as stable. These stability requirements may be expressed by the following equations:

$$\left| \frac{f_k - f_{k+1}}{f_k} \right| \leq 1\% \tag{3.72}$$

$$\left| \frac{\xi_k - \xi_{k+1}}{\xi_k} \right| \leq 5\% \tag{3.73}$$

$$\left(1 - \mathbf{MAC}_{k,k+1}\right) \leq 2\% \tag{3.74}$$

where k indicates the identified model order and **MAC** is the Modal Assurance Criterion (MAC),

which is a scalar constant that provides a measure of consistency between estimates of modal vectors $\boldsymbol{\phi}_k$ and $\boldsymbol{\phi}_{k+1}$, defined by:

$$\mathbf{MAC}_{k,k+1} = \frac{\left|\boldsymbol{\phi}_k^{\mathrm{H}}\,\boldsymbol{\phi}_{k+1}\right|^2}{\left(\boldsymbol{\phi}_k^{\mathrm{H}}\,\boldsymbol{\phi}_k\right)\left(\boldsymbol{\phi}_{k+1}^{\mathrm{H}}\,\boldsymbol{\phi}_{k+1}\right)} \tag{3.75}$$

with $(\bullet)^{\mathrm{H}}$ denoting the conjugate transpose or Hermitian transpose operator. By definition, the MAC takes on values from 0 - corresponding to a zero degree of consistency between the two vectors, to 1 - representing a consistent correspondence.

A graphical representation of this scheme is depicted in Fig. 3.3. It is shown that upon decomposition of the block Toeplitz matrix of output covariances, a varying even number of singular values ($2m_1 < 2m_2$) is successively chosen for the reconstruction of system matrices $\mathbf{A}_{2m_1}$, $\mathbf{G}_{2m_1}$ and $\mathbf{A}_{2m_2}$, $\mathbf{G}_{2m_2}$. Subsequently, each discrete-time system, of order $2m_1$ and $2m_2$, respectively, is used to extract the discrete time properties based on Eq. (3.65). These in turn yield the, m_1 and m_2 in number respectively, continuous-time eigenproperties on the basis of Eq. (3.68) and the corresponding natural frequencies, damping ratios and mode shapes through Eqs. (3.69)-(3.71). Thereafter, those properties satisfying the stability criteria described by Eqs. (3.72)-(3.74) are plotted in the stabilization diagram and the arising vertical alignments of stable poles are representing the physical modes of the model.

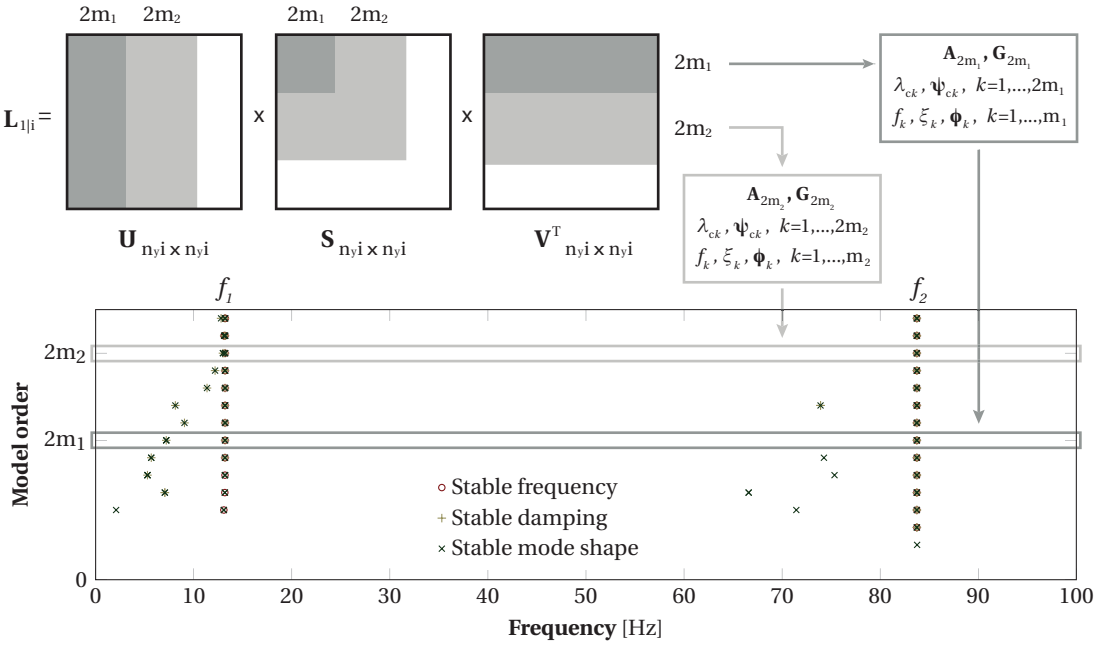

Figure 3.3: Construction of stabilization diagram

It should be mentioned that the stability limits described in Eqs. (3.72) - (3.74) are just denoting the adopted values and can be accordingly adjusted, depending on the quality of the measurement data and the noise level. The reasoning behind the chosen limits is that damping ratios are expected to have a high scatter, requiring larger tolerance, while frequencies and mode shapes are less sensitive and stabilization may be ensured with lower limits.

3.4 Cluster analysis

It was shown in this chapter that system identification using the SSI-Cov and SSI-Data algorithms may be performed through the use of stabilization diagrams. However, such a technique does not provide any automatic solution of the model identification problem at hand and it is merely furnishing a graphical output that demands some visual inspection for the extraction of the identified parameters. For instance, although it is evident from Fig. 3.3 that among the obtained natural frequencies for different model orders there are two frequencies appearing with a certain consistency in vertical alignments, namely f_1 and f_2, these frequencies are not given as a direct output but need to be graphically determined.

An innovative methodology to overcome this requirement for human intervention and to enable an automatic identification of the modal characteristics is the cluster analysis. This term denotes a set of techniques with the primary purpose of grouping objects into so-called clusters, based on their characteristics. The resulting clusters from such an analysis should present high external (between-cluster) heterogeneity as well as high internal (within-cluster) homogeneity (Hair et al., 1998). Within the present project, the aim of this methodology is to group the poles of the stabilization diagram that represent identical modes so that the identification process is automatically performed.

Among the numerous cluster formulations, hierarchical clustering is one of the most widely used methods, based on the hierarchy of a tree-like structure (Fig. 3.4). The implementation of hierarchical cluster-algorithms comprises three main steps: the measurement of similarity between the objects of the dataset, the linkage of the objects in a hierarchical structure and the definition of a cut-off rule for the interruption of the tree construction. Among others, the divisive and agglomerative approaches are the basic ones for generating hierarchical clustering, with the latter being the one that will be employed in this thesis.

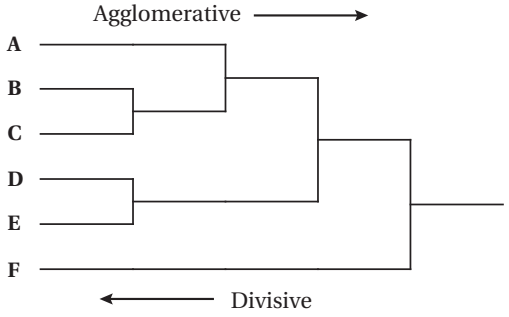

Figure 3.4: Representation of hierarchical clustering in dendrogram

Divisive hierarchical clustering, which is a "top-down" approach, starts with a single all-inclusive cluster and at successive steps a cluster is split until each object constitutes an individual cluster. On the other hand, agglomerative hierarchical clustering, which is by far the most common technique, begins with each object considered as an individual cluster. Then, at each subsequent step, the two closest clusters are merged into a new one, and the number of clusters is hence reduced by one in each step, until all objects are grouped into a large cluster. Within this context, various algorithms may be used, depending on the method for the calculation of proximity between clusters. These include single linkage, complete linkage, average linkage (Fig. 3.5), centroid method and Ward's method.

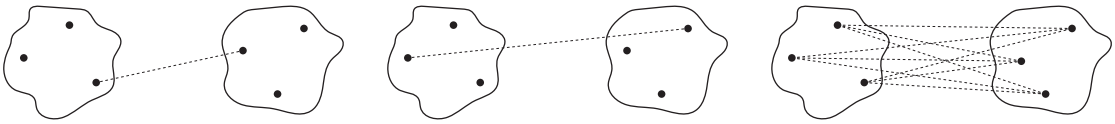

(a) Single linkage (b) Complete linkage (c) Average linkage

Figure 3.5: Criteria of cluster proximity

Conventionally, the similarity between objects or clusters is calculated by means of the Euclidean distance between the quantities to be grouped, with the values of the objects playing the role of coordinates. In the case of OMA, this proximity may be measured in terms of frequencies, mode shapes and damping ratios. Yet, given the high scatter of the latter and the possibility that two different modes may share the same damping ratio, it is more appropriate to exclude the damping ratio from the similarity rules.

Hence, in the present framework, the proximity criteria is based on the estimated values of the natural frequencies and mode shapes, so that the distance between two poles (j and k) is obtained from the following formula:

$$d_{jk} = \left| \frac{f_j - f_k}{f_k} \right| + \left(1 - \mathbf{MAC}_{j,k}\right) \tag{3.76}$$

in which f_j is the natural frequency estimate of mode j and $\mathbf{MAC}_{j,k}$ the modal assurance criterion between mode shapes j and k, calculated on the basis of Eq. (3.75). In this sense, when the proximity between two estimates is within a certain limit, both estimates are considered to represent the same physical mode and they are grouped in the same cluster.

Once the rule for measurement of similarity between different objects is determined, the next step is to define the distance between already formed clusters. As already underlined, and depicted in Fig. 3.5, there are various formulations of the hierarchical agglomerative clustering, depending on the calculation of this distance. The one used herein, which is based on the single-linkage criterion (Fig. 3.5(a)), assumes that the distance between two clusters is defined as the shortest distance from any object in the first cluster to any object in the second cluster.

Hereafter, the cut level of the hierarchical tree should be selected. Normally, this is determined by the number of expected clusters. This number however is unknown since it represents the number of modes to be identified. In this sense, for the interruption of clustering a rule is established whereby the distance from any object to its closest object of the same cluster is restricted to a certain maximum value. Following the limits for the construction of stabilization diagrams, indicated by Eqs. (3.72) - (3.74), the said maximum distance for the tree cut level is set to 0.03, as the sum of the limits for natural frequencies and mode shapes. Of course this value has a strong effect on the final number of clusters and its calibration depends on the quality of the measured data and specifically on the noise level.

4 Sensitivity Analysis

Before venturing into the damage identification process by means of vibration monitoring, a set of possible damaged states is necessary to be determined. Theoretically, this may comprise an infinite number of damage combinations. Within the framework of the present project, however, only a set of damaged states for which identifiability is ensured will be examined. In this sense, this chapter constitutes an attempt to distinguish a series of identifiable damage scenarios induced by corrosion and fatigue cracks. Such a task is accomplished by investigating the change of dynamic properties (natural frequencies, mode shapes and damping ratios) of the model under consideration in the presence of varying degrees of damage for each mechanism.

4.1 Reference model

As highlighted in Chapter 1, the notions of damage and degradation always involve a comparison between two distinct situations, one of which corresponds to the initial or undamaged condition. It is essential therefore to establish a starting point that will serve as the reference basis for the structural health assessment. To this end, a typical stiffened panel on an FPSO hull is considered, as illustrated in Fig. 4.1. The modal properties of this panel will be the reference point of the sensitivity analysis.

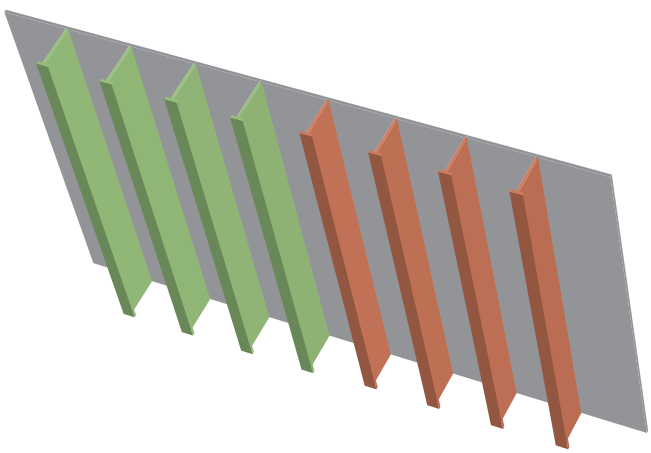

Figure 4.1: Schematic representation of the considered stiffened panel

The steel structure whose geometrical properties are described in Table 4.1, consists of

eight stiffeners divided into two groups of four, indicated with green and red colour respectively (Fig. 4.1). It is assumed to constitute a member of the side shell of a typical section of an FPSO, restricted to an area between two transverse webframes and two horizontal stringers, as depicted in Fig. 4.2. It is modelled with a parametric numerical model using the FE method. In this way the simulation of damage states is enabled by means of thickness reduction for the case of corrosion and through the inclusion of discontinuities for fatigue cracks.

Member	**Color**	**Dimensions** [mm]	**Young's Modulus** [GPa]	**Poisson ratio** [-]
Plate	Gray	8100×20	210	0.3
Stiffeners	Green	$600 \times 12 + 150 \times 20$		
Stiffeners	Red	$550 \times 11.5 + 150 \times 18$		

Table 4.1: Geometry and material properties of the stiffened panel

In order to allow for the detailed modelling of localized damage, the panel is modelled with solid elements. According to the regulations concerning the FE modelling of ship structures (DNV, 2014), iso-parametric 20-node elements with mid-side nodes at the edges are used. This option offers a displacement function that allows steep stress gradients as well as plate bending with linear stress distributions in the thickness direction, using one element in the said direction. The analytical formulation of the employed 20-node iso-parametric element is described in Chapter 2.

Conventionally, for the modelling of stiffened panels in maritime engineering, the boundary conditions on the plate edges are, in favour of safety, assumed to be simple supports (Paik and Kim, 2002). Such an approach provides however, some pessimistic results, given that all edges are surrounded by structural elements whose rigidities cannot be neglected. Considering thus the presence of the adjacent longitudinal stiffeners and transverse frames, one would deduce that there exists a degree of translational and rotational restraint on the edges of the plates which should be accounted for. Furthermore, these restraints are determined

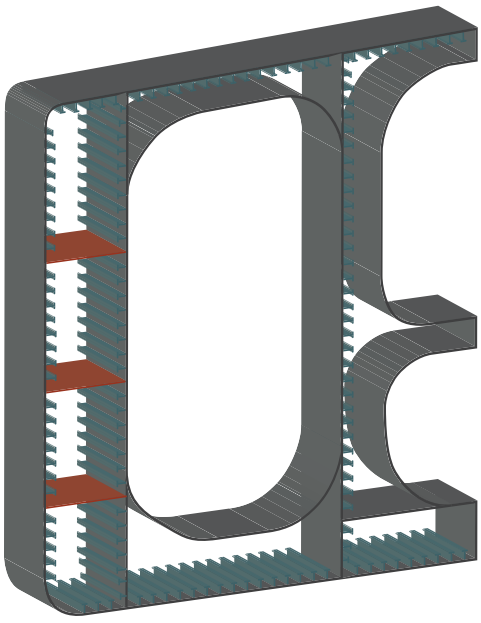

Figure 4.2: Typical section of FPSO

by the bending and torsional rigidities of the supporting members respectively, which are significantly larger than those of the plates themselves. Through this reasoning, the boundary conditions on the edges of the stiffened panel are considered to be fixed.

The dynamic behaviour of the reference stiffened panel and subsequently of the damaged ones is assumed to be represented by the first ten natural modes, shown in Fig. 4.3 along with their corresponding natural frequencies for the undamaged state. The choice of this modal basis relies on the requirement for observability of all structural locations on the dynamic response, so that damage is theoretically identifiable over the entire structure. Concretely, the modal basis is chosen such that all components, i.e. plate and stiffeners, are participating in the reduced-order dynamic representation of the panel.

It can be seen in Fig. 4.3 that the chosen modal basis for the representation of the dynamic behaviour of the panel may be divided into three classes. Considering first the fact that the panel consists of two groups of stiffeners, as illustrated in Fig. 4.1, the first two groups of mode shapes can each be related to one of these groups of stiffeners. The first four mode shapes, with frequencies ranging from 30.37 to 31.23 Hz, involve the vibration of the first group of stiffeners indicated in green in Fig. 4.1. Accordingly, mode shapes from 5 to 8, corresponding to frequencies between 31.67 and 32.60 Hz, refer to the vibration modes of the second group of stiffeners which is represented in red in Fig. 4.1.

It should be remarked that the relatively small difference between the frequency ranges of the two groups is justified by the different web heights of the two groups of stiffeners. The green group of stiffeners is namely of web height equal to 600 mm while for the red group the web height is 550 mm. It is thus reasonable that the more slender green group of stiffeners vibrate at lower frequencies than the more stiff group of red stiffeners.

Finally, the third group of mode shapes pertains to the vibration of the plate with participation of the stiffeners in a whole wave-length mode. The frequencies corresponding to these mode shapes range from 65.25 to 67.01 Hz as indicated in Fig. 4.3. The reasoning behind the higher frequency values of this last group compared to the previous ones lies in the participation of the plate with a double-waviness bending mode and the whole wave-length vibration of the stiffeners. This results in the contribution of all members with a high stiffness index which subsequently leads to larger stiffness to mass ratios and therefore larger natural frequencies.

It should be noted that the calculated modal basis does not account for the presence of water in the ballast tank but it merely represents the wet stiffened panel as an independent structure. This of course implies that the coupled motion between the panel and the water is not taken into account, neglecting thus the contribution of the additional vibrating mass of the liquid. Nonetheless, such an interaction between the fluid and the structure may have a significant contribution in both the mode shapes and the natural frequencies. With respect to the latter, it can be said that they will decrease due to the additional mass, hence getting closer to the usual frequency range of excitation under operational conditions.

The dynamic properties of Fig. 4.3 are obtained on the basis of the reduced-order undamped eigenvalue problem of Eq. (2.34) in order to achieve time-efficient computation. The full-order mass and stiffness matrices are first fully constructed and then reduced using Eqs. (2.26) and (2.27), upon utilization of the scheme of Section 2.2.2 for the selection of the degrees of freedom to be condensed. The final results of the reduced model are verified with those of the full model in terms of the first ten natural frequencies.

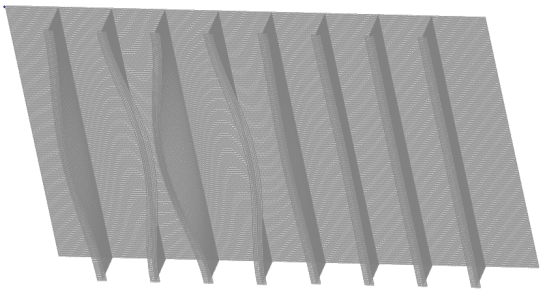

(a) Mode 1 - 30.37 Hz

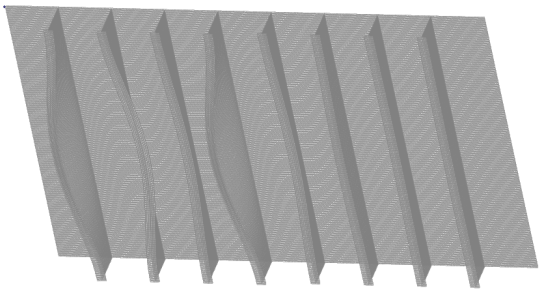

(b) Mode 2 - 30.76 Hz

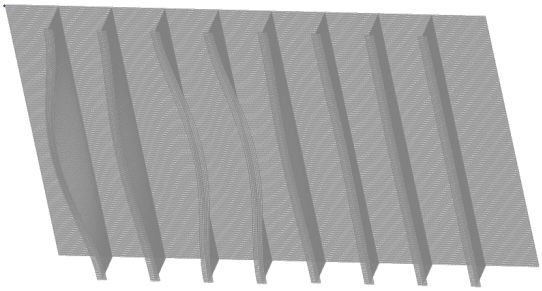

(c) Mode 3 - 31.07 Hz

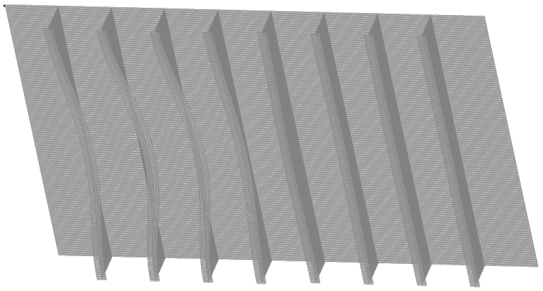

(d) Mode 4 - 31.23 Hz

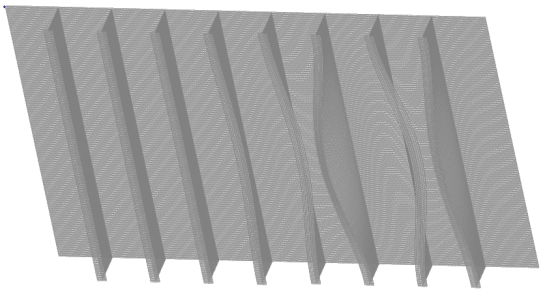

(e) Mode 5 - 31.67 Hz

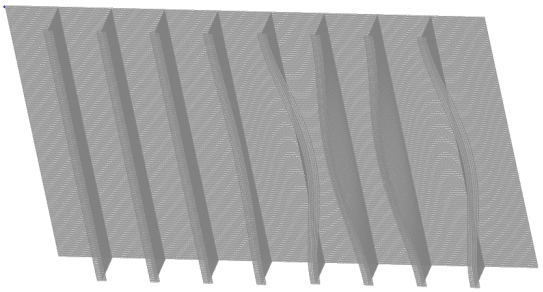

(f) Mode 6 - 32.12 Hz

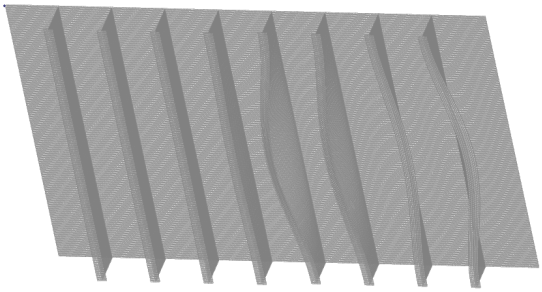

(g) Mode 7 - 32.44 Hz

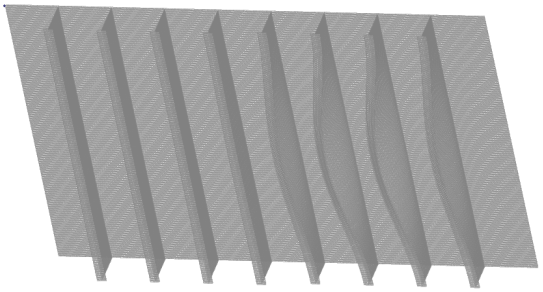

(h) Mode 8 - 32.60 Hz

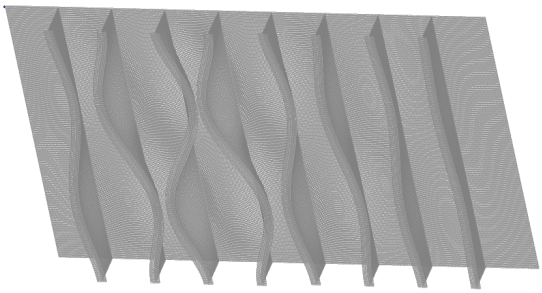

(i) Mode 9 - 65.25 Hz

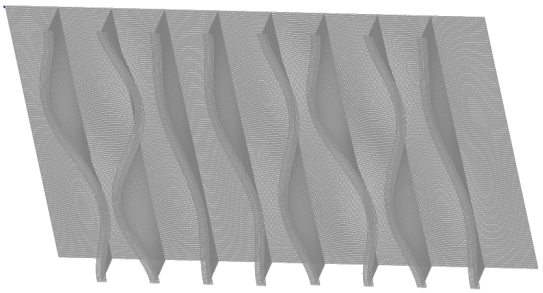

(j) Mode 10 - 67.01 Hz

Figure 4.3: Mode shapes and natural frequencies of the reference model

4.2 Corrosion

In studying the effect of corrosion on the structural properties of stiffened panels, the dominant types of uniform and pitting corrosion will be examined, following the recommendations provided by DNV (2013).

4.2.1 Uniform corrosion

The first damage condition to be considered, is general corrosion. It should be reminded that such a state assumes a uniform distribution of the degradation on the exposed surface, even though the corroded area exhibits a sort of waviness and roughness. In order to determine the sensitivity of each structural component to this particular degradation mechanism, the study is carried out by applying the uniform corrosion pattern to the plate and the stiffeners separately. The damage is applied by means of an equivalent thickness reduction on the corresponding structural member.

Plate

Fig. 4.4 illustrates the values of the first ten natural frequencies of the reference model in comparison with those of the corroded models. Five different degrees of damage are considered, ranging from 5 % to 25 % material wastage on the plate. The calculated values of each natural frequency for all ten modes of the corroded models are presented in Table 4.2. It should be mentioned at this point that the analysed degrees of damage are chosen on the basis of the maximum allowable thickness reduction on hull structures, which according to DNV (2013) may be up to 30 %.

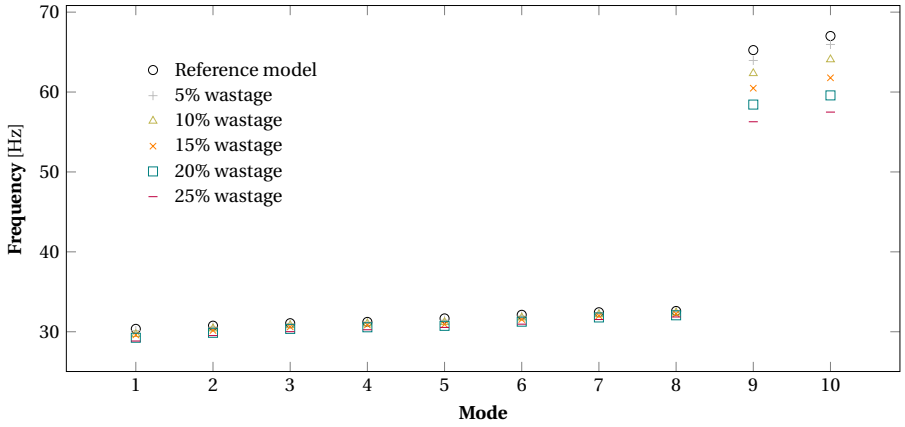

Figure 4.4: Natural frequencies of the stiffened panel with uniform corrosion on the plate

As expected, this corrosion pattern has an insignificant influence on the natural frequencies of the first eight modes, given that these are mainly referring to vibrational combinations of the stiffeners. For the most severely damaged case of 25% wastage, the average frequency change for modes 1 to 8 is only 1.5 Hz, corresponding to a 5 % reduction. On the other hand, modes 9 and 10 are the ones to be highly affected by corrosion on the plate with a frequency reduction of up to 15 Hz, which is translated to a more than 10 % difference. Such a reduction is of course due to the fact that material wastage on the plate implies a subsequent stiffness decrease which becomes more manifest in plate-modes and therefore leads to the corresponding reduction in natural frequencies.

Mode no.	f_k [Hz]					
	Reference model	**5% wastage**	**10% wastage**	**15% wastage**	**20% wastage**	**25% wastage**
1	30.37	30.15	29.90	29.60	29.25	28.84
2	30.76	30.59	30.40	30.16	29.87	29.52
3	31.07	30.95	30.80	30.62	30.37	30.01
4	31.23	31.14	31.03	30.86	30.56	30.26
5	31.67	31.44	31.19	30.93	30.74	30.54
6	32.12	31.96	31.77	31.54	31.27	30.95
7	32.44	32.32	32.17	32.00	31.79	31.54
8	32.61	32.51	32.39	32.24	32.06	31.85
9	65.25	63.94	62.34	60.48	58.44	56.28
10	67.01	65.97	64.07	61.78	59.58	57.50

Table 4.2: Natural frequencies of the stiffened panel with uniform corrosion on the plate

With regard to the corresponding mode shapes of the corroded models, it should be remarked that they remain unaffected for all five degrees of damage. This can be verified either visually or more accurately in terms of the MAC. Through the latter, the comparison between mode shapes of a corroded model and those of the initial model may be carried out by examining their **MAC** value, as introduced in Eq. (3.75). When two mode shapes are showing a consistent correspondence, their **MAC** value will be 1, while for independent mode shapes with null consistency their **MAC** value will be 0. In Fig. 4.5, a graphical representation of the **MAC** matrix between the mode shapes of the reference model and the corroded one with 25% wastage is presented. It is shown that, since all diagonal entries are equal to 1 and the off-diagonal terms do not present any consistency, the mode shapes of the two models are completely consistent and therefore it can be deduced that they are insensitive to the applied degradation pattern.

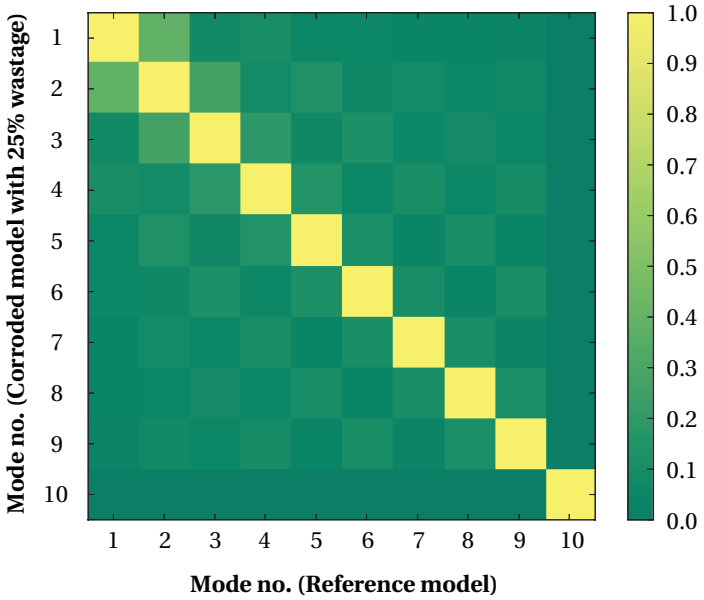

Figure 4.5: MAC matrix between mode shapes of reference model and 25%-corroded model

Stiffeners

In Fig. 4.6, the natural frequencies of the corroded models with uniform thickness reduction on the stiffeners are graphically depicted. Again, the degree of damage varies from 5 to 25 % of material wastage and the exact values of the natural frequencies are summarized in Table 4.3. Similarly, as in the previous scenario, the mode shapes were found to remain unaffected by all five degrees of damage.

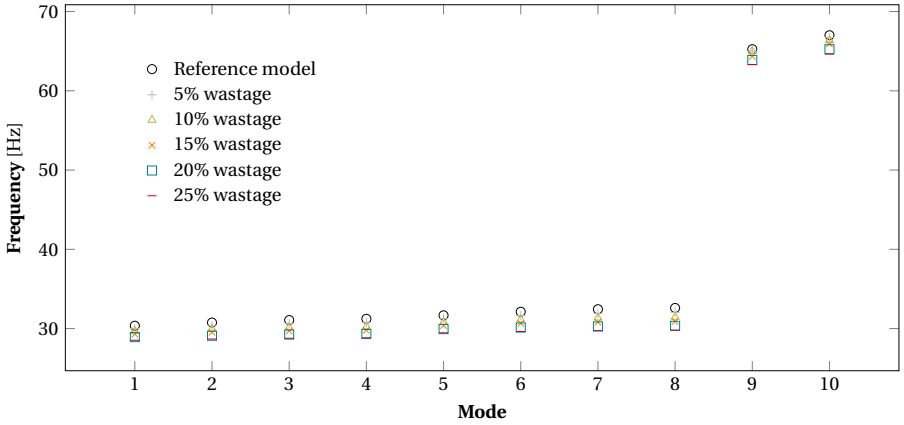

Figure 4.6: Natural frequencies of the stiffened panel with uniform corrosion on the stiffeners

Unlike the uniform corrosion pattern on the plate, the structure appears to be less sensitive to corrosion on the stiffeners. This can be readily observed by a close view of the mode shapes in Fig. 4.3. Since mode shapes 1 to 8 involve the lateral vibration of stiffeners, their natural frequencies are mainly dominated by the stiffness contribution of the width of the flanges. It is therefore reasonable that a thickness reduction on the flange and the web of the stiffeners has only a minor influence on the relevant stiffness and subsequently on the natural frequencies. The same reasoning applies for modes 9 and 10, to a lesser extend though since, apart from lateral vibration of stiffeners, their mode shapes involve bending of the plate which is much more influenced by thickness reduction of the web of stiffeners.

Mode no.	f_k [Hz]					
	Reference model	**5% wastage**	**10% wastage**	**15% wastage**	**20% wastage**	**25% wastage**
1	30.37	30.02	29.67	29.30	28.92	28.53
2	30.76	30.35	29.95	29.53	29.10	28.68
3	31.07	30.62	30.16	29.70	29.24	28.78
4	31.23	30.75	30.27	29.79	29.31	28.84
5	31.67	31.26	30.83	30.38	29.93	29.47
6	32.12	31.64	31.14	30.65	30.13	29.63
7	32.44	31.90	31.36	30.81	30.27	29.74
8	32.61	32.04	31.47	30.90	30.35	29.80
9	65.25	65.00	65.00	64.33	63.88	63.30
10	67.01	66.72	66.36	65.92	65.25	64.63

Table 4.3: Natural frequencies of the stiffened panel with uniform corrosion on the stiffeners

4.2.2 Pitting corrosion

The pitting corrosion pattern applied on the plate of the stiffened panel is based on available data from actual hull structures. Although the distribution of pits on the plate surface shows high scatter, it can be accurately assumed, according to Paik et al. (2003), that they are following a uniform distribution. Hence, a uniform distribution of pits over the surface of the plate is assumed in the present project as well, with a representative pattern of 20% Degree of Pitting (DOP) depicted in Fig. 4.7(a).

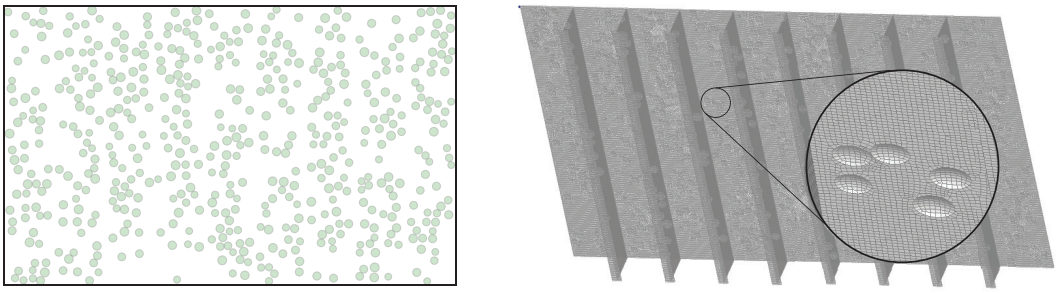

(a) Distribution of pits for 20% DOP

(b) Detail of FE model with corrosion pits

Figure 4.7: Properties of model with pitting corrosion

Based on actual observations (Nakai et al., 2004), the shape of corrosion pits on the surface of hulls is a part of a sphere, while their diameter to depth ratio is almost constant between 10:1 and 8:1. The maximum pit diameter varies between 25 and 80 mm (Daidola et al., 1997) and the maximum average of allowable thickness loss is equal to 50% of the initial thickness. Finally, the maximum allowable DOP, upon which replacement is required, is equal to 30% according to Paik and Thayamballi (2002). Based on the aforementioned properties, the pits are assumed to be spherically shaped with diameter normally distributed between 25 and 80mm and the diameter to depth ratio is chosen to be constant and equal to 10:1, leading to a normally distributed pit depth between 2.5 and 8 mm. A detail of the FE model with pitting corrosion on the plate is depicted in Fig. 4.7(a).

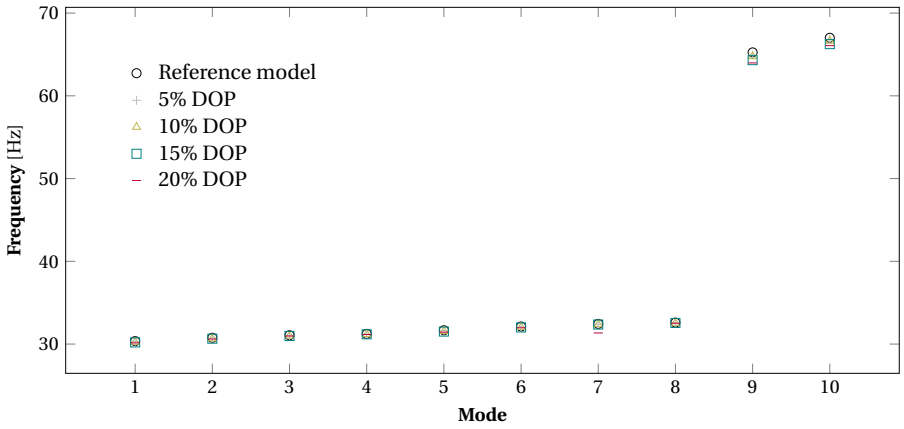

Figure 4.8: Natural frequencies of the stiffened panel with pitting corrosion on the plate

The results, in terms of natural frequencies, for four different DOP are graphically presented and cross-compared with the corresponding values of the reference model in Fig. 4.8,

while the exact values are summarized in Table 4.4. Due to the localized character of this damage state, it is seen that the global modal properties are hardly affected. Not only do the natural frequencies appear to be insensitive, with the most noticeable change in the order of only 1.5%, but also the corresponding mode shapes remain constant.

Mode no.	f_k [Hz]				
	Reference model	**5% DOP**	**10% DOP**	**15% DOP**	**20% DOP**
1	30.37	30.32	30.26	30.20	30.15
2	30.76	30.71	30.66	30.65	30.61
3	31.07	30.04	31.00	30.98	30.97
4	31.23	31.21	31.18	31.18	31.15
5	31.67	31.61	31.56	31.51	31.44
6	32.12	32.08	32.05	32.01	31.97
7	32.44	32.41	32.38	32.36	32.34
8	32.61	32.58	32.55	32.55	32.52
9	65.25	64.93	64.77	64.31	63.98
10	67.01	66.81	66.63	66.25	66.07

Table 4.4: Natural frequencies of the stiffened panel with pitting corrosion on the plate

It is worth mentioning at this point that localized changes in the structural properties of a model, i.e. stiffness and mass distribution, are mostly visible in higher order modes associated with local vibrations. However, the response of dynamic systems is usually dominated by the first few global modes and therefore changes in the modal properties of higher modes are very difficult to observe. In this sense, it is reasonable that the first ten modes of the stiffened panel are insensitive to pitting corrosion. Although this hurdle can be overcome by extending the modal basis with higher modes, it is unlikely that these will be excited under normal operational conditions, given their significantly high natural frequencies.

4.3 Fatigue cracks

Fatigue cracks constitute the second group of damage states to be examined. Within this context, cracks are introduced in the numerical model of the reference structure by means of discontinuities in the FE model. In Fig. 4.9, a close-up view of the FE model with a through thickness crack on the plate is presented. It should be noticed at this point that crack growth and propagation models are not taken into account within this study and cracks are merely considered as existing discontinuities with varying length, width and location over the structural model.

Apart from the identifiable damage states due to fatigue cracks, that constitute the ultimate aim of this section, it is of particular interest to underline a set of insensitive crack scenarios for which the modal properties remain constant. These pertain to through-thickness cracks on the plate of the stiffened panel with varying opening width and length. A representative case of these scenarios is depicted in Fig. 4.9 for which a crack between two stiffeners with an opening of 2.0 mm is assumed. Similar unresponsive scenarios comprise cracks perpendicular to the stiffeners either within the plate or at the edges of the plate, representing the connection with the adjacent members.

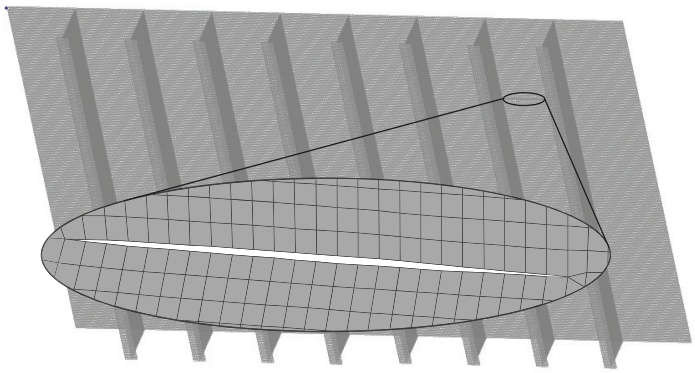

Figure 4.9: Detail of the FE model with fatigue through-thickness cracks on the plate

4.3.1 1st Scenario

The first group of identifiable crack scenarios to be examined pertains to damage on the stiffeners and specifically at their connection to the transverse frame. In order to approach a lower bound of these damage states, a severe scenario is first assumed. This comprises a fully cracked connection between a stiffener and the transverse frame. The natural frequencies obtained in this case are graphically presented in Fig. 4.10 along with those of the reference model.

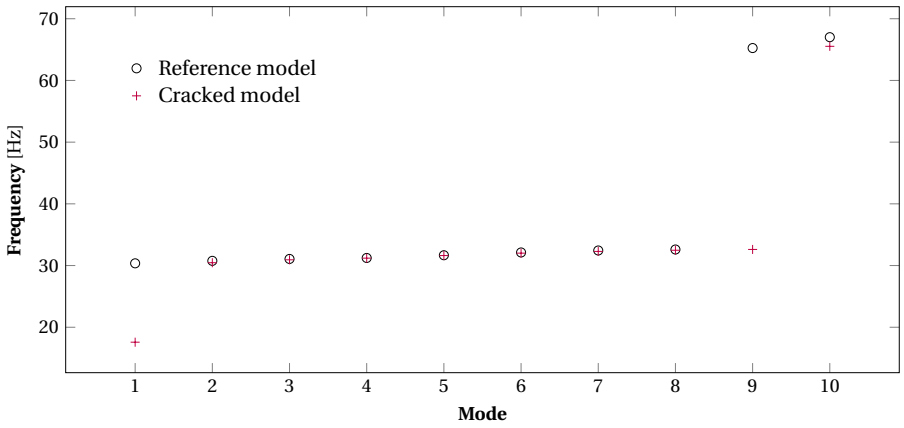

Figure 4.10: Natural frequencies of the cracked stiffened panel - 1st scenario

Apart from the first mode shape of the cracked model, which is illustrated in Fig. 4.11 along with the first mode shape of the reference model, the rest of the modes present very little difference with the reference model. The new mode of the cracked model involves lateral vibration of the stiffener whose connection is assumed to be destroyed. It is therefore evident that such a model may be readily identified either in terms of frequencies, given the high reduction of almost 50%, or in terms of mode shapes. It should additionally be underlined that the presence of mode 1 in the cracked model causes mode shapes 2 to 10 to appear in shifted order, corresponding thus to mode shapes 1 to 9 of the reference model.

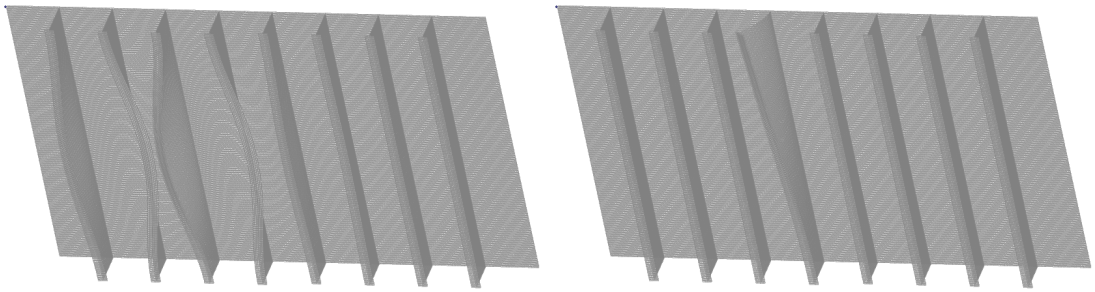

(a) Reference model - 30.37 Hz (b) Cracked model - 17.58 Hz

Figure 4.11: First mode shape of reference and cracked stiffened panel - 1st scenario

4.3.2 2nd Scenario

In the second scenario, the same weld between the stiffener and the transverse frame is assumed to be partially destroyed. Concretely, only the connection between the flange of the stiffener with the transverse frame is assumed to be cracked while the web is considered to be fully welded. In Fig. 4.12 the natural frequencies of the cracked model are compared with those of the reference model, while their values are presented in Table 4.5. For the sake of generality, it should be mentioned that equivalent results, in terms of sensitivity and therefore identifiability, are obtained by assuming any other stiffener-connection to be cracked.

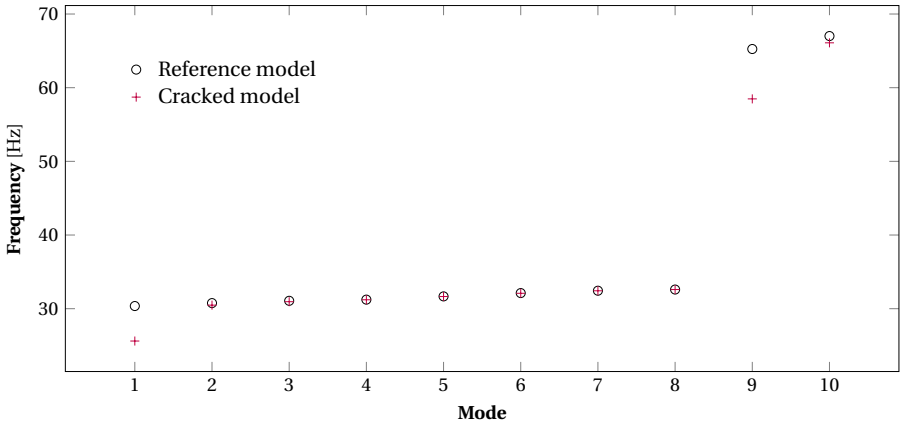

Figure 4.12: Natural frequencies of the cracked stiffened panel - 2nd scenario

Through Fig. 4.12, it can be readily deduced that modes 1 and 9 are highly affected in terms of frequencies by this crack scenario, creating thus an appropriate sensitive point for identification. However, it should be remarked that, unlike the previous scenario, in this case not only mode shape 1 shows inconsistency with the reference model but mode shape 9 as well. In Fig. 4.13 a comparison between the first mode shape of the reference and the cracked model is illustrated whereby it is shown that the latter is represented by a half wave-length vibration of the stiffener with cracked connection. Similarly, Fig. 4.14 provides the corresponding comparison between the ninth mode shapes of the two models. Although in the previous crack scenario the ninth mode was similar to that of the reference model, in this figure it is seen that it represents, as in the case of the first mode, a whole wave-length vibration pattern of the cracked stiffener.

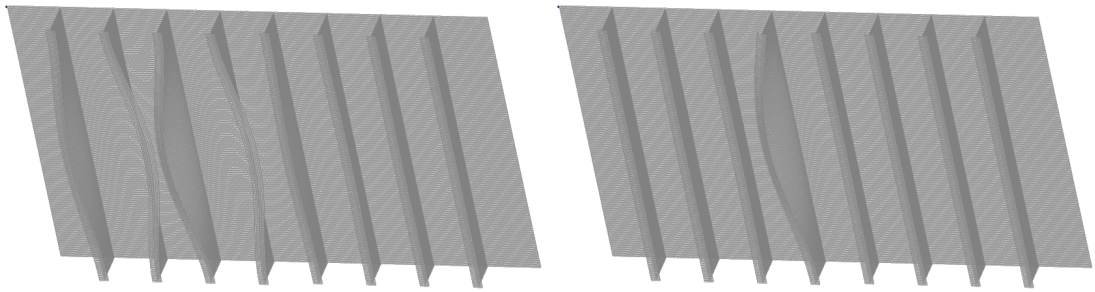

(a) Reference model - 30.37 Hz (b) Cracked model - 25.61 Hz

Figure 4.13: First mode shape of reference and cracked stiffened panel - 2nd scenario

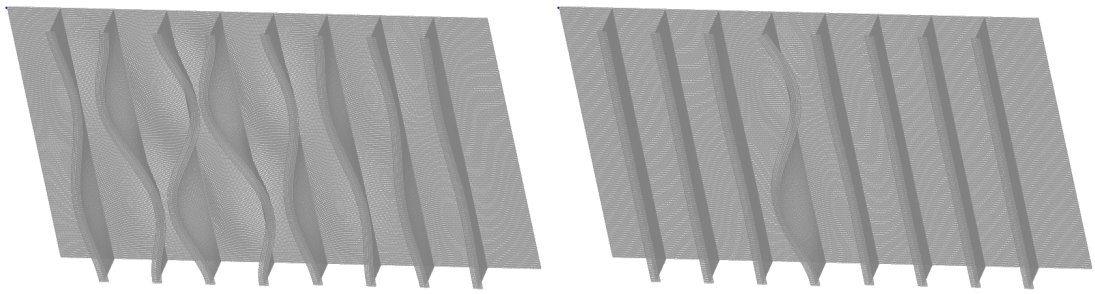

(a) Reference model - 65.25 Hz (b) Cracked model - 58.48 Hz

Figure 4.14: Ninth mode shape of reference and cracked stiffened panel - 2nd scenario

4.3.3 3rd Scenario

Finally, the third crack scenario refers to the same connection between the stiffener and the transverse frame, but with a smaller degree of damage. Specifically, the web of the stiffener is again assumed to be completely welded with the frame while the flange is assumed to be partially cracked, only through half of the thickness. The obtained natural frequencies for the cracked model are illustrated in Fig. 4.15 along with those of the reference model while the corresponding values are summarized in Table 4.5.

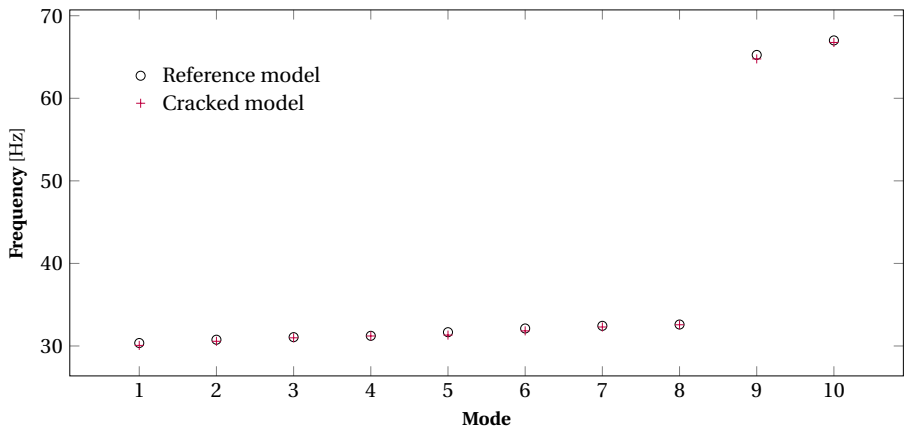

Figure 4.15: Natural frequencies of the cracked stiffened panel - 3rd scenario

Unlike the previous scenario, in which the fully cracked flange had a strong impact on both frequencies and mode shapes, in this case the natural frequencies are seen to be less sensitive. This can be verified through Fig. 4.15, in which frequencies 1 and 9 were expected to show a distinguishable discrepancy with those of the reference model while in reality this is only in the order of 1%. On the other hand, it can be seen that the assumed crack yields an identifiable first mode shape. In Fig. 4.16 a comparison of the first mode shape between the cracked and the reference model is shown. It can be seen that even though both modes are represented by closely spaced frequencies, their shapes do not show any correspondence, enabling thus the distinction between the two models.

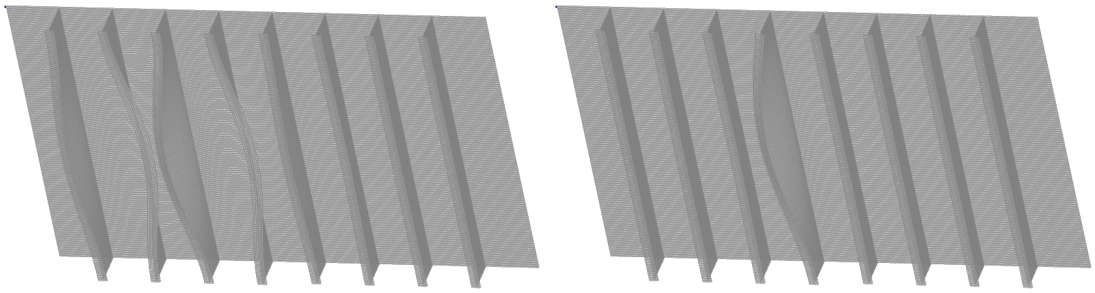

(a) Reference model - 30.37 Hz (b) Cracked model - 30.07 Hz

Figure 4.16: First mode shape of reference and cracked stiffened panel - 3rd scenario

As in the case of pitting corrosion, this fatigue crack scenario involves a localized change of the structural system. Although this change is visible in terms of mode shapes, the influence on the natural frequencies would be observable only in higher order modes which are unlikely to contribute to the global response. Consequently, even though it is possible to ensure identifiability by means of the forward problem, observability and subsequently damage detection will be always determined by the inverse process.

Mode no.	f_k [Hz]			
	Reference Model	**1st Scenario**	**2nd Scenario**	**3rd Scenario**
1	30.37	17.58	25.61	30.07
2	30.76	30.46	30.48	30.57
3	31.07	30.93	30.95	30.99
4	31.23	31.20	31.21	31.21
5	31.67	31.62	31.65	31.32
6	32.12	32.01	32.09	31.83
7	32.44	32.29	32.43	32.30
8	32.61	32.48	32.60	32.57
9	65.25	32.61	58.48	64.77
10	67.01	65.53	66.09	66.76

Table 4.5: Natural frequencies of the stiffened panel with fatigue cracks

The values of the natural frequencies for all three crack scenarios are summarized in Table 4.5 in comparison with those of the reference model. For the sake of a fair comparison, it

should be remarked that frequencies marked with gray represent new modes that do not exist in the reference model. Hence, modes 2 to 10 of the first and third scenarios are showing correspondence with modes 1 to 9 of the reference model. Accordingly, for the second scenario modes 2 to 8 correspond to modes 1 to 7 of the reference model while mode 10 is equivalent to mode 8 of the reference model.

5 Operational Modal Analysis

5.1 Operational response

For the implementation of the SSI algorithms, a set of synthetic measurements should be obtained for each one of the damage scenarios. Such a task is accomplished through the dynamic analysis of each model in the presence of environmental loads. Generally, the stiffened panel in ships, and particularly in FPSOs, may be subjected to a combination of lateral pressure and in-plane loads. Lateral pressure is due to water pressure which in turn is induced by waves or sloshing loads. On the other hand, in-plane loads comprise axial load and in-plane bending, which are principally induced by the overall hull bending. Setting aside the latter which is expected to have a minor contribution to the lateral vibrations of the panel, the focus will be on the wave and sloshing loads. Nonetheless, a stiffened panel may be located either below or above the waterline and it is therefore most likely that it will be excited by sloshing loads as part of the ballast tanks Fig. 5.1.

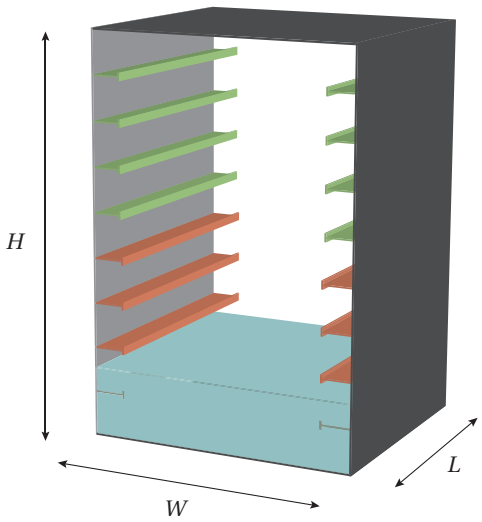

Figure 5.1: Ballast tank

It should be noted that despite the high scientific and industrial attention for the sloshing phenomenon, there is not yet an accurate and robust prediction approach for the sloshing-induced impact loads (Kim et al., 2013). It is for this reason that various classification societies,

among others the American Bureau of Shipping (2006), DNV (2006) and Lloyd's Register (2009), endorse the model test investigation for the sloshing assessment, in preference to computational or analytical approaches.

As underlined by Lloyd's Register (2004), for an oscillating tank, various sloshing waves will be generated as a function of the fill depth and the frequency content of the oscillations. These waves may comprise different modes of liquid motion whose dynamic pressure though can be classified into two types; namely non-impulsive and impulsive pressure. The latter, which is to be examined within the framework of this project, arises in tanks with low fill levels, between 0.1H and 0.3H where H denotes the height of the tank (Fig. 5.1), and is due to a rapid and continuous build-up of liquid and liquid pressure on the immersed surfaces. Typically, the duration δt of such an impact is in the order of 1/10 - 1/1000 of the sloshing wave period while its period T_{fn} coincides with that of the sloshing-induced wave. Fig. 5.1 gives a schematic representation of a sloshing-induced impulsive pressure normalised over the hydrostatic pressure $\rho_w g h$.

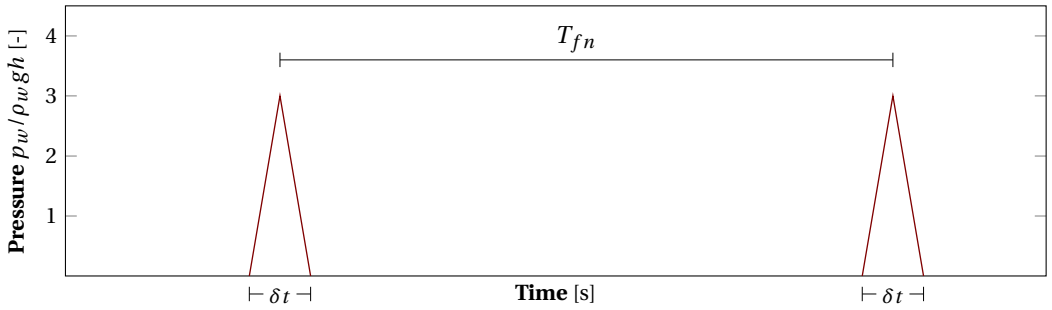

Figure 5.2: Typical sloshing-induced impulsive pressure

It is also possible that high impact pressures due to sloshing may not occur in the most severe environmental conditions (Lloyd's Register, 2009). Such a case is especially relevant for low filling levels with water heights between 0.10H and 0.30H. The reasoning behind this is that in harsh sea conditions the sloshing waves break due to their high steepness and hence the wave energy is dissipated before they reach the walls of the tank. On the other hand, in mild seastates, the sloshing waves are significantly less steep and may thus travel the entire distance of the tank before impacting the wall. Consequently, it can be deduced that sloshing-induced impacts in the ballast tanks (Fig. 5.3) are more likely to occur in less severe sea conditions.

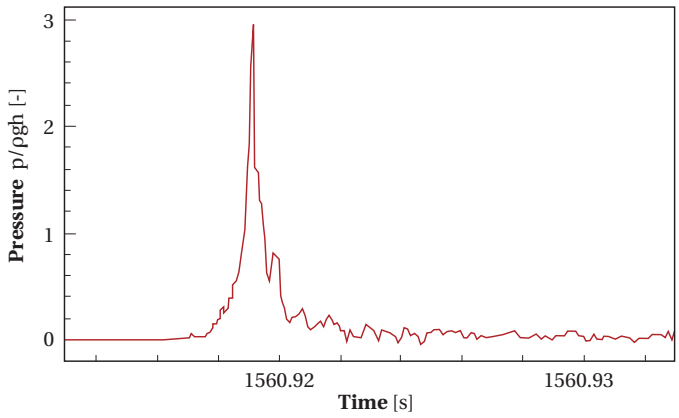

Figure 5.3: Pressure signal for low filling level h = 0.15H (Kim et al., 2013)

With the assumption of a low fill height equal to 0.15H = 1.20 m for the ballast tank whose stiffened panel is examined, the influence of stiffeners on the water motion may be neglected given that for this height the waterline is located between the level of the first and the second stiffener (Ibrahim, 2005). The tank may thus be simplistically considered as rectangular for the assessment of water motion and the fluid-free-surface natural frequency can be obtained by:

$$\omega_{fn} = \sqrt{(2n+1)\frac{\pi g}{\mathrm{W}}\tanh\left(\frac{(2n+1)\pi h}{\mathrm{W}}\right)} \tag{5.1}$$

where g denotes the gravitational acceleration, h represents the fill height and W = 5.5 m is the width of the tank. Fig. 5.4 illustrates the first two natural frequencies of the free surface with respect to the fill height as well as the values that correspond to the chosen fill level, equal to 1.85 and 4.05 rad/s respectively. Consequently, the corresponding natural periods are equal to $\mathrm{T_{f0}}$ = 3.40 s and $\mathrm{T_{f1}}$ = 1.55 s.

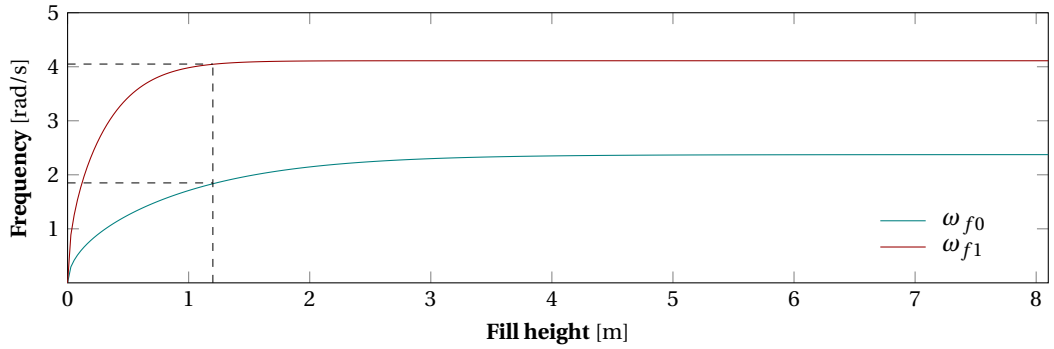

Figure 5.4: Natural frequencies of the free surface as function of the fill height

According to the above considerations, the input pressure that will yield the operational response of the stiffened panel is assumed to consist of a series of impacts with duration equal to $\delta t = 1/100\mathrm{T_{f0}}$ and period equal to the natural period of the fluid-free-surface $\mathrm{T_{f0}}$ = 3.40 s, based on the notation of Fig. 5.2. The pressure is considered to act on the plate of the stiffened panel on a band of width $0.2h$ around the waterline. Fig. 5.5 illustrates a time frame of 50 s for the signal of the adopted normalized pressure, whose magnitude is equal to three times the hydrostatic pressure.

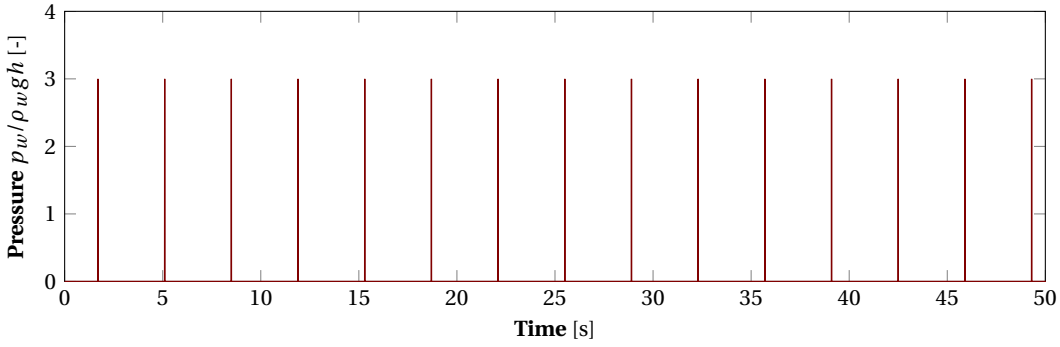

Figure 5.5: Time history of the input pressure with δt = 0.034 s and T_{f0} = 3.4 s

5.2 Sensor network

Before the sensor configuration is determined, it is essential to examine the identifiability conditions of the examined system. In order for the entire modal basis to participate in the structural response, the system must be *controllable*; all states thus should be controlled by the input or in terms of the modal characteristics, matrix $\mathbf{S}_p^T\mathbf{\Phi}$ should not contain any zero columns. In practice, this requirement is fulfilled by ensuring that none of the modal responses is zero and therefore all modes are contributing to the global dynamic response of the panel.

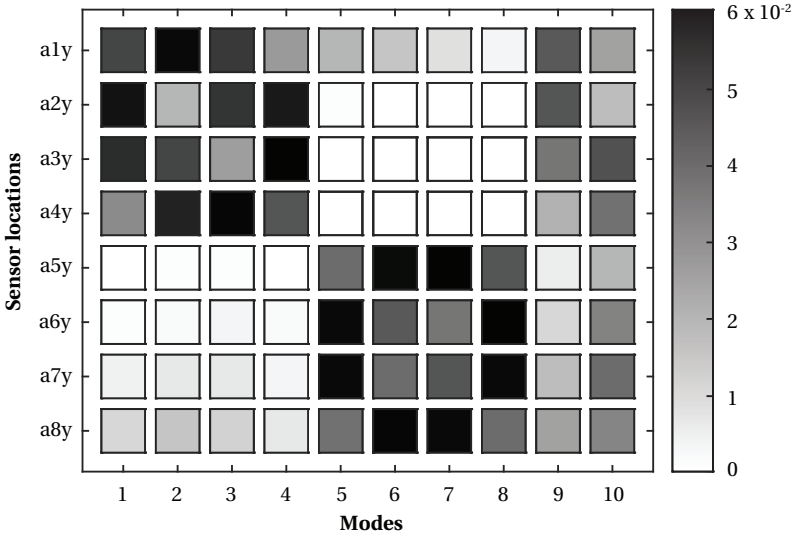

Figure 5.6: Graphical representation of the matrix $\mathbf{S}_y\mathbf{\Phi}$ - Observability condition

Similarly, in order for the structural modes to be identifiable, observability of the system should be ensured. This condition implies that all states are observable in the system output and is satisfied if and only if $\mathbf{S}_y\mathbf{\Phi}$ does not contain any zero columns. An examination of the modal basis, depicted in Fig. 4.3, is sufficient to deduce that the stiffeners are contributing to all vibration modes in the lateral direction (along the y-axis) while the plate is mainly participating in modes 9 and 10 (along the z-axis). In this sense, the initial candidate sensor

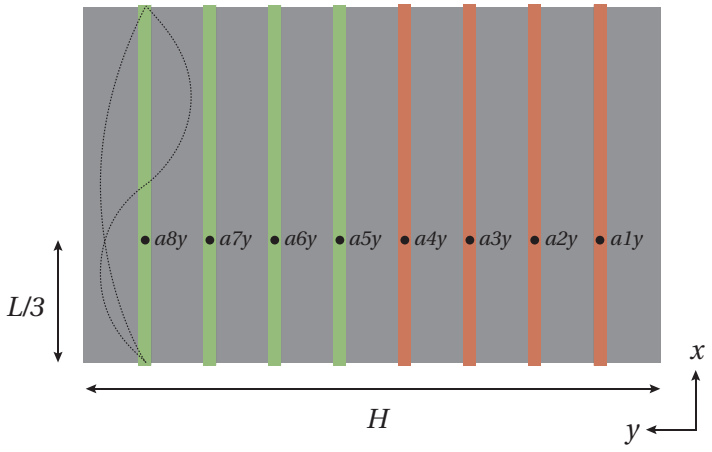

Figure 5.7: Sensor locations

configuration is assumed to consist of 8 accelerometers placed at the flanges of the stiffeners and denoted by aiy, with i referring to the number of the stiffener and y representing the measuring direction. Fig. 5.6 shows a graphical representation of the modal projections $\mathbf{S}_{\mathrm{y}}\boldsymbol{\Phi}$ to the considered sensor locations indicating the contribution of the modes to each of the outputs. In order to achieve observability of modes with both half and whole wave-length vibration of the stiffeners, the sensors are placed at a third of the length of the stiffeners.

Although it can be seen from Fig. 5.6 that observability may be ensured even with two accelerometers, one for each group of stiffeners (e.g. a1y and a5y), it will be shown in the following section that due to the closely spaced natural frequencies of the first eight modes, some of the frequencies are masked by the noise, leading thus to an underestimation of the model order. The minimum number of sensors in order to overcome this problem and ensure robustness of the identified properties for all model states is equal to 8, one on each stiffener (Fig. 5.7). Based on this considerations, the final measurement set-up to be used for the identification process consists of the 8 accelerometers of Fig. 5.7.

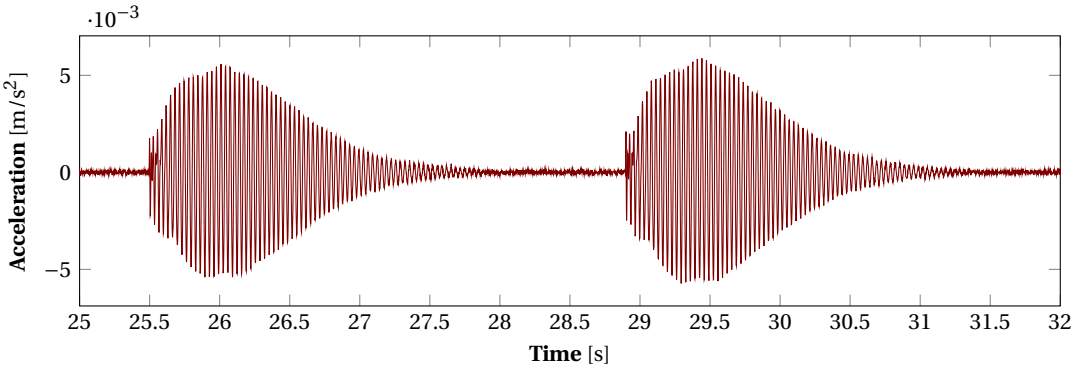

Figure 5.8: Time history of acceleration at sensor location a1y with 3% noise level

Application of the force time signals to the FE model produces the artificial measurement data at the these chosen sensor locations. Hereafter, the measurement data $\mathbf{y}_k$ are polluted with Gaussian white noise, generating thus the noisy output vector $\tilde{\mathbf{y}}_k \in \mathbb{R}^{n_{\mathrm{y}}}$ at each time step k, as a function of the standard deviation:

$$\tilde{\mathbf{y}}_k = \mathbf{y}_k + \delta\,\boldsymbol{\sigma}_{\mathrm{y}}\,\mathbf{r}_k \tag{5.2}$$

in which δ is the noise level, $\boldsymbol{\sigma}_{\mathrm{y}} \in \mathbb{R}^{n_{\mathrm{y}} \times n_{\mathrm{y}}}$ represents the standard deviation matrix which contains the standard deviations of the measurement signals as diagonal entries and $\mathbf{r}_k \in \mathbb{R}^{n_{\mathrm{y}}}$ is a vector containing random values drawn from the standard normal distribution. Fig. 5.8 illustrates a 10 sec time frame of the acceleration signal at sensor location a1y upon pollution with 3% noise.

5.3 Reference model

In order to investigate the feasibility of damage detection on the examined stiffened panel, a consistent comparison framework should be determined. The existence of inevitable discrepancies between the real structure and the numerical model, implies that employment of the latter as a reference model would introduce a certain bias in the results. To avoid this, the reference model , which in reality may not refer to an undamaged condition, should be

calibrated so that the in-situ dynamic properties are more accurately represented. In this sense, the reference basis which was previously numerically evaluated, is redetermined by means of the inverse process, using the SSI algorithms.

The initial model is thus subjected to the sloshing-induced impulsive pressure of Fig. 5.5 and its response is obtained using the first ten modes, as presented in Chapter 4. The time histories of the accelerations at the chosen sensor locations are then extracted and polluted with 3% white Gaussian noise according to Eq. (5.2).

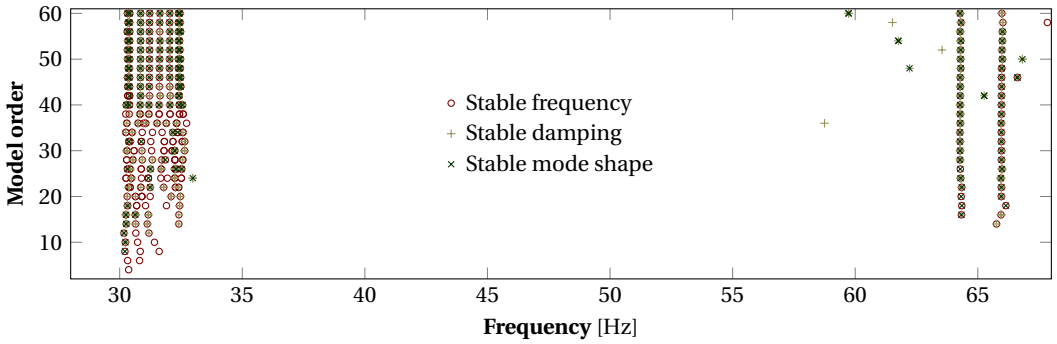

Figure 5.9: Stabilization diagram using the SSI-Cov algorithm

For both algorithms, the number of block rows i for the construction of the block Hankel matrix $\mathbf{Y}_{0|2i-1}$, is a parameter that has a strong effect on the quality of stabilization diagrams and it should therefore be properly adjusted. In the following analyses, its value is equal to 30 and the subsequent stabilization diagrams are constructed for model orders ranging from 2 to 60. Furthermore, the employed limits for the classification of the estimates, based on Eqs. (3.72)-(3.74), are: 1% for natural frequencies, 5% for damping ratios and 2% for mode shape estimates.

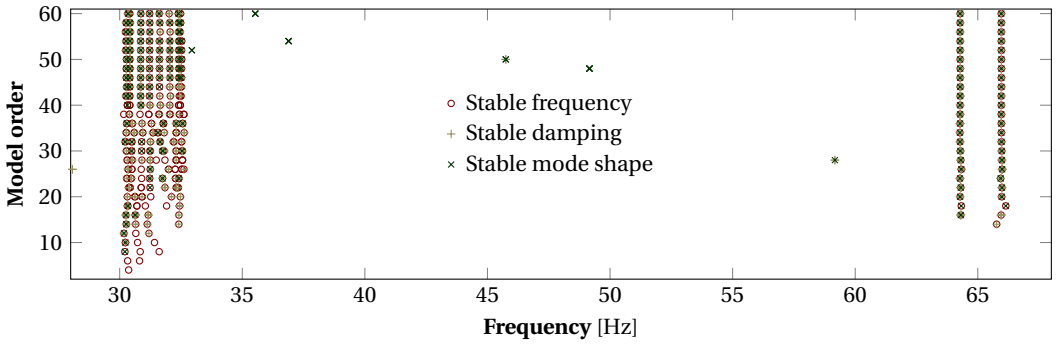

Figure 5.10: Stabilization diagram using the SSI-Data algorithm

The results obtained with the SSI-Cov and SSI-Data algorithms are presented in Figs. 5.9 and 5.10, respectively. The estimated natural frequencies and their errors resulting from each algorithm are summarized in Table 5.1 along with the corresponding true values, as calculated in Chapter 4. Although both algorithms furnish sufficiently accurate results, it should be remarked that the SSI-Cov algorithm is performing significantly faster, compared to the relatively slow QR-factorization required at the corresponding step of the SSI-Data algorithm. Namely, an average execution time of the SSI-Data algorithm with the present configuration is 12.7 seconds while the SSI-Cov algorithm needs only 5.6 seconds.

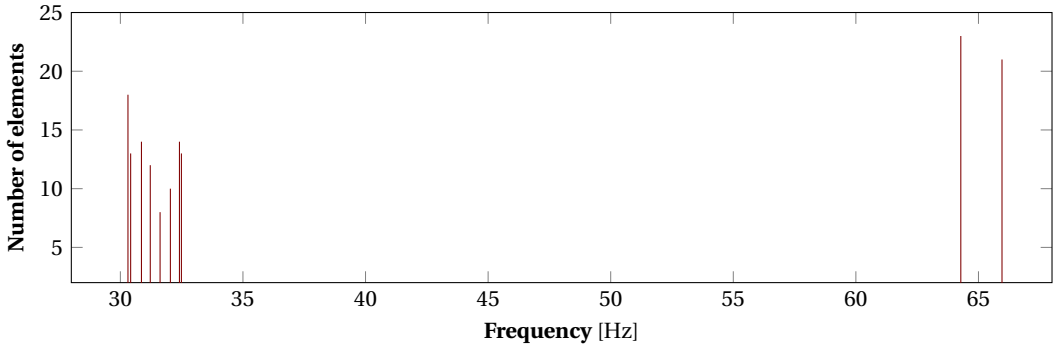

Figure 5.11: Number of elements of the clusters - using the SSI-Cov algorithm

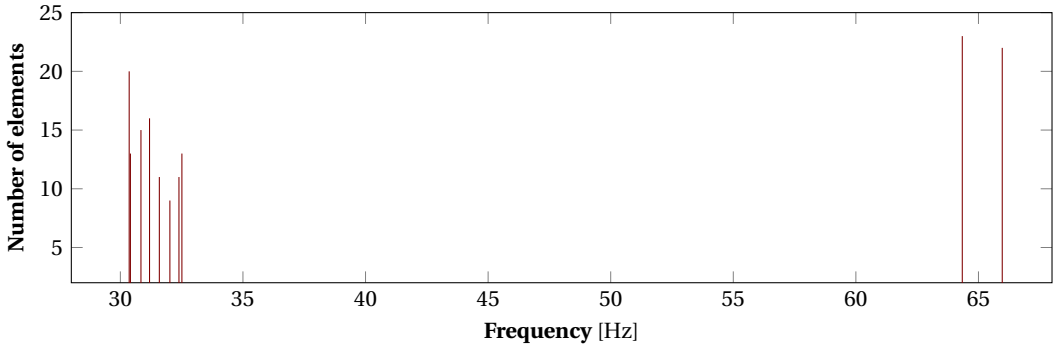

Figure 5.12: Number of elements of the clusters using the SSI-Data algorithm

An indicative view of the capabilities of the algorithms in terms of accuracy may be formed through Table 5.1. One can see that the obtained estimates of the natural frequencies using both algorithms present a maximum error of 1.57%. This implies that small changes in natural frequencies, (i.e. up to that percent) are impossible to be identified since they can reasonably be attributed to the existence of noise. Consequently, identifiability, that was ensured for a couple of scenarios in Chapter 4 through the forward problem, will finally be determined from the accuracy of the inverse process.

In order to extract the identified natural frequencies in an automatic way, the poles of

Mode no.	**True values**	**SSI-Cov**		**SSI-Data**	
	f_k [Hz]	$\hat{f}_k$ [Hz]	error [%]	f_k [Hz]	error [%]
1	30.37	30.31	0.20	30.36	0.03
2	30.76	30.42	1.10	30.41	1.14
3	31.07	30.86	0.67	30.84	0.74
4	31.23	31.22	0.03	31.19	0.13
5	31.67	31.62	0.16	31.59	0.25
6	32.12	32.04	0.25	32.02	0.31
7	32.44	32.41	0.09	32.39	0.15
8	32.60	32.49	0.34	32.51	0.28
9	65.25	64.28	1.49	64.34	1.39
10	67.01	65.96	1.57	65.97	1.55

Table 5.1: Frequency and damping ratio estimates of the reference model

the stabilization diagrams for both SSI-Cov and SSI-Data algorithms are processed by an agglomerative cluster analysis with a single linkage proximity rule between clusters and a maximum distance for the tree cut level, defined by Eq. 3.76, equal to 0.03. Once the clusters are formed, they can be filtered with respect to the number of elements in order to determine the physical poles which appear with certain consistency in the stabilization diagrams and discard the spurious ones which are gathered in cluster with only a few elements. The resulting clusters are graphically illustrated in Figs. 5.11 and 5.12 for each one of the algorithms respectively, with their average value on the horizontal axis and the number of elements in the vertical axis. The clusters with less than 5 elements are filtered out from the aforementioned figures and therefore the illustrated clusters represent only the physical modes.

5.3.1 Limitations

It should be noted at this point that due to the configuration of the considered structure, the implementation of the SSI algorithms is subject to certain restrictions. Namely, the fact that the first eight natural frequencies are closely spaced, may, under certain circumstances, render the algorithms incapable of separating the frequencies and lead to an underestimated model order and misleading natural frequencies. It is therefore essential to point out that such limitations would be visible only through the inverse process and as a result the use of any *a priori* knowledge with respect to the system is fundamental in order to tackle any masked effects.

One of these susceptible points, which can be adequately explained by means of the stabilization diagram, is the noise level in the output measurements. Considering an ideal, noiseless, model which could be accurately captured by the inverse process, would yield a stabilization diagram with exclusively stable points, aligned with the corresponding real values of the natural frequencies. On the other hand, pollution of the output measurements of the said system with noise, would introduce a certain drift of the estimated values around the real ones, ruining therefore their alignment. When the identified poles are closely spaced, the misaligned estimates are merged and the identification of the real parameters becomes impossible. This phenomenon is observed in Fig. 5.13, which presents the stabilization diagram for a noise level equal to 5%. It is seen that due to high noise, the closely spaced natural frequencies are blended in the stabilization diagram, becoming hence indistinguishable, while stabilization is achieved mainly in terms of frequencies.

The number of employed sensors is another factor that should be carefully considered. Again, due to the existence of closely spaced natural frequencies, the separation of the esti-

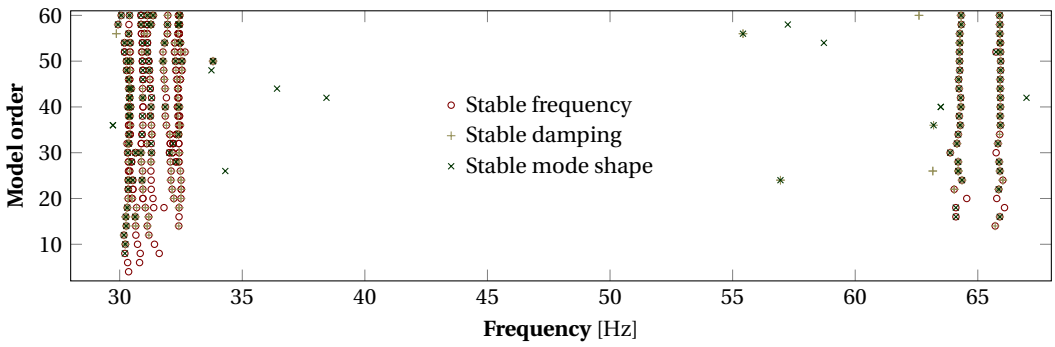

Figure 5.13: Stabilization diagram using the SSI-Cov algorithm with 5% noise

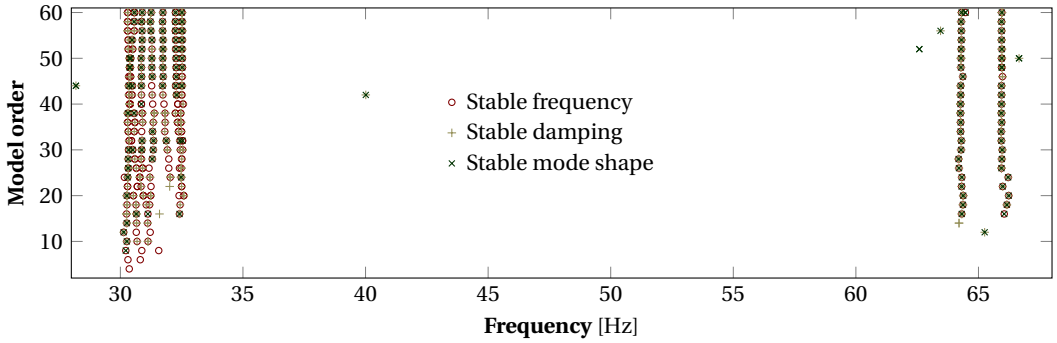

Figure 5.14: Stabilization diagram using the SSI-Cov algorithm with 7 sensors (excluding a5y)

mated values may become impossible with the reduction of the number of sensors. In Fig. 5.14, which depicts the stabilization diagram resulting from the use of 7 sensors upon removal of sensor a5y (Fig. 5.7), one can see that although the results are less sensitive to the reduction of the output measurements, the identified modal characteristics are erroneous. Namely, the modal estimates of the left-hand side appear to stabilize after a certain model order however, only 7 vertical alignments are presented, providing thus the information for only 7 natural frequencies.

5.3.2 Alternative configuration

Apart from the proposed sensor network configuration of Fig. 5.7, with 8 accelerometers at a third of the length of the stiffeners, the identification process for the reference model may be equally performed using strain gauges on the plate. Observing the mode shapes of the reference model (Fig. 4.3), one can deduce the that lateral vibration of two adjacent stiffeners is combined with bending of the intermediate plate. Therefore, the information contained in two accelerometers placed on the flanges of adjacent stiffeners is equivalent to that provided by one of the accelerometers and a strain gauge placed in the middle of the intermediate plate, measuring in the x-axis (Fig. 5.7).

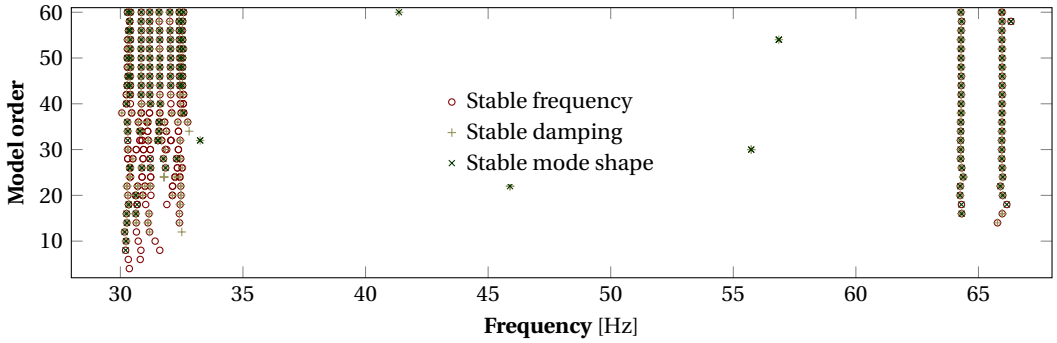

Figure 5.15: Stabilization diagram using the SSI-Cov algorithm with 7 accelerometers and 1 strain gauge

In Fig. 5.15, the stabilization diagram using the SSI-Cov algorithm with 7 accelerometers and 1 strain gauge is presented. Accelerometer a5y is now excluded and a strain gauge on the plate between a5y and a6y (Fig. 5.7) is employed instead. It is seen that a sufficiently accurate identification of the natural frequencies may be achieved with this configuration as well.

However, it should be remarked that with this alternative configuration the stiffener without accelerometer remains unobservable and if for instance a crack occurs on this stiffener, it will not be identifiable. It is therefore for this reason that the rest of the study is based on the initially proposed layout of Fig. 5.15.

5.4 Damage identification

As in the case of the reference model, all damaged models are subjected to the sloshing-induced impulsive pressure of Fig. 5.5 and their response is obtained using the first ten modes, as presented in Chapter 4. The time histories of the measurements at the chosen sensor locations (Fig. 5.7) are polluted with 3% white Gaussian noise and then processed with the SSI-Cov algorithm, whose number of block rows i is chosen equal to 30. Subsequently, the stabilization diagrams are constructed for each model and their data are further processed with a cluster analysis. The obtained clusters are filtered by removing the ones with less than 5 objects and the retained ones are those that represent the physical modes. The identified modal properties for each mode are finally given by the average values of each cluster.

5.4.1 Uniform corrosion

The structural degradation due to uniform corrosion is studied, as in the forward problem, separately due to corrosion on the plate and the stiffeners. The same damaged scenarios as those of Chapter 4 are now investigated through the inverse process.

Plate

Considering that the mode shapes of the stiffened panel with uniform corrosion on the plate remain constant, the identification is examined only in terms of frequencies. The identified change of the first and ninth natural frequency with respect to the five degrees of damage are presented in Fig. 5.16. It is seen that the degradation is well captured by both frequencies while it is more evident through the ninth (Fig. 5.16(b)) which refers to the vibration mode of the plate, on which the damage is applied. The identified natural frequencies of all ten modes for the five degrees of wastage are summarized in Table 5.2 with the numbers into parenthesis indicating the difference from the reference model.

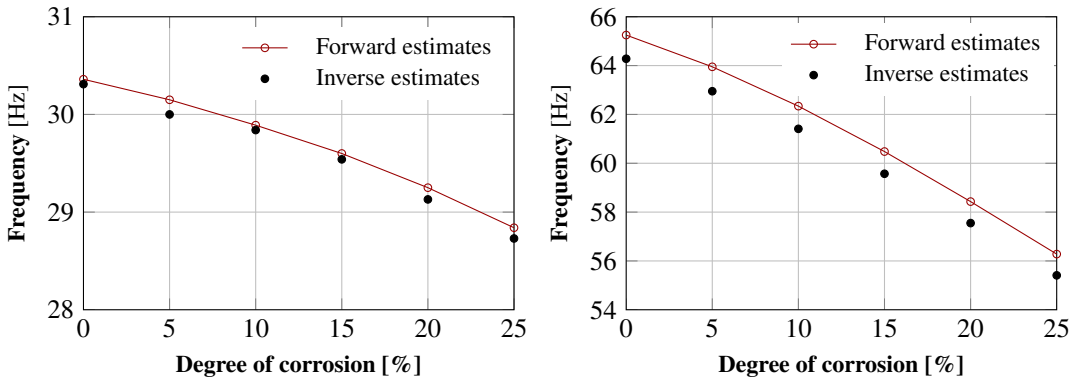

(a) First natural frequency

(b) Ninth natural frequency

Figure 5.16: Estimated natural frequencies for the model with uniform corrosion on the plate

Mode no.	$\hat{f}_k$ [Hz]					
	Reference model	5% wastage	10% wastage	15% wastage	20% wastage	25% wastage
1	30.31	30.00 (1.02)	29.84 (1.55)	29.54 (2.54)	29.13 (3.89)	28.73 (5.21)
2	30.42	30.49 (0.23)	29.99 (1.41)	30.03 (1.28)	29.77 (2.14)	29.45 (3.19)
3	30.86	30.84 (0.06)	30.48 (1.23)	30.16 (2.27)	30.27 (1.91)	29.93 (3.01)
4	31.22	31.11 (0.35)	30.87 (1.12)	30.62 (1.92)	30.30 (2.95)	29.97 (4.00)
5	31.62	31.17 (1.42)	31.29 (1.04)	30.93 (2.18)	30.62 (3.16)	30.36 (3.98)
6	32.04	31.77 (0.84)	31.81 (0.72)	31.45 (1.84)	31.13 (2.84)	30.81 (3.84)
7	32.41	32.20 (0.65)	32.14 (0.83)	31.94 (1.45)	31.66 (2.31)	31.39 (3.15)
8	32.49	32.42 (0.22)	32.22 (0.83)	32.26 (0.71)	31.97 (1.60)	31.72 (2.37)
9	64.28	62.95 (2.07)	61.41 (4.46)	59.57 (7.34)	57.55 (10.47)	55.41 (13.78)
10	65.96	64.95 (1.53)	63.07 (4.38)	60.81 (7.81)	58.65 (11.08)	56.61 (14.17)

Table 5.2: Natural frequency estimates of the stiffened panel with uniform corrosion on the plate

If one considers the accuracy of the identified frequencies of the reference model, which was found to be 1.57%, as the error margin of the SSI-Cov algorithm, then the feasibility of damage identification may be based on the relation between this accuracy and the estimated frequency change. An observation of the values of Table 5.2 reveals that for a small degree of damage (5%) the identified changes are quite close to the error margin and therefore nothing can be safely deduced about damage. It is however evident that a 10% material wastage may be readily identified through modes 9 and 10 for which the frequency change is larger than 4%. For more severe damage, the structural degradation can be detected by a larger part of the modal basis while it becomes fully observable through the entire modal basis for the severe state of 25% wastage.

Stiffeners

The same pattern, as in the previous case, occurs for the first and ninth natural frequency of the model with uniform corrosion on the stiffeners (Fig. 5.17). Although the frequencies are not that highly influenced by this type of corrosion, the degradation trend is quite well captured and the existence of damage can be safely deduced.

Following the same reasoning with respect to the error margin of the estimates, one can

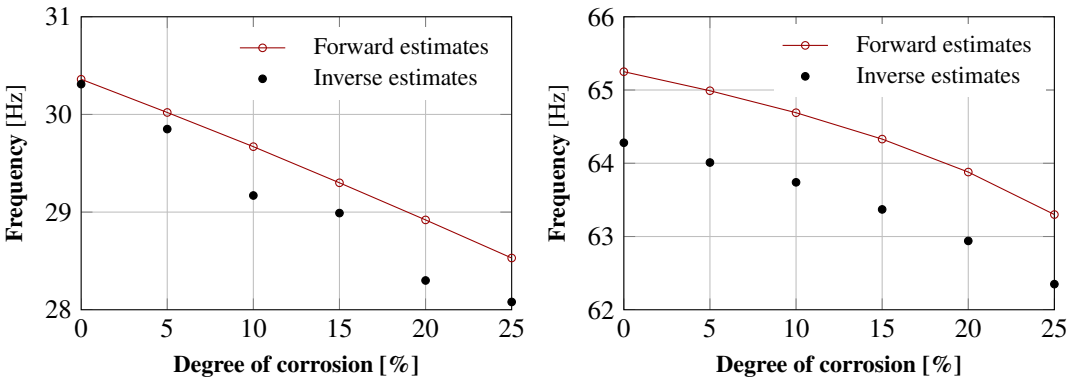

(a) First natural frequency

(b) Ninth natural frequency

Figure 5.17: Estimated natural frequencies for the model with uniform corrosion on the stiffeners

conclude again that a small degree of damage, equal to 5%, is not possible to be identified with certainty. It is shown however, that for larger degrees (10% and above) the existence of uniform corrosion on the stiffeners can be identified using all modes that refer to the vibration of the stiffeners, i.e modes 1 to 8. Again, for the most severely damaged scenario, degradation becomes identifiable through the entire modal basis with estimated frequency changes larger than 3%.

Mode no.	$\hat{f}_k$ [Hz]					
	Reference model	5% wastage	10% wastage	15% wastage	20% wastage	25% wastage
1	30.31	29.85 (1.52)	29.17 (3.76)	28.99 (4.35)	28.30 (6.63)	28.08 (7.36)
2	30.42	30.25 (0.56)	29.64 (2.56)	29.41 (3.32)	28.79 (5.36)	28.51 (6.28)
3	30.86	30.48 (1.23)	29.98 (2.85)	29.74 (3.63)	29.13 (5.61)	28.76 (6.80)
4	31.22	30.60 (1.99)	30.32 (2.88)	29.82 (4.48)	29.47 (5.61)	28.81 (7.72)
5	31.62	31.02 (1.89)	30.73 (2.81)	30.15 (4.65)	29.65 (6.23)	29.11 (7.93)
6	32.04	31.43 (1.90)	31.16 (2.74)	30.56 (4.62)	29.99 (6.40)	29.72 (7.24)
7	32.41	31.79 (1.91)	31.39 (3.15)	30.95 (4.50)	30.35 (6.36)	30.22 (6.75)
8	32.49	32.17 (0.98)	31.52 (2.98)	31.07 (4.37)	30.93 (4.80)	30.74 (5.39)
9	64.28	64.01 (0.42)	63.74 (0.84)	63.37 (1.41)	62.94 (2.08)	62.35 (3.01)
10	65.96	65.66 (0.45)	65.33 (0.95)	64.81 (1.74)	64.33 (2.47)	63.61 (3.56)

Table 5.3: Natural frequency estimates of the stiffened panel with uniform corrosion on the stiffeners

5.4.2 Pitting corrosion

In contrast to uniform corrosion, it was shown through the forward problem that degradation due to pitting corrosion has only a small influence on the natural frequencies of the panel. It was also remarked that for this reason it would be difficult to use vibration-based monitoring for the identification of pitting corrosion. This conclusion is herein proved through the following results of the inverse process.

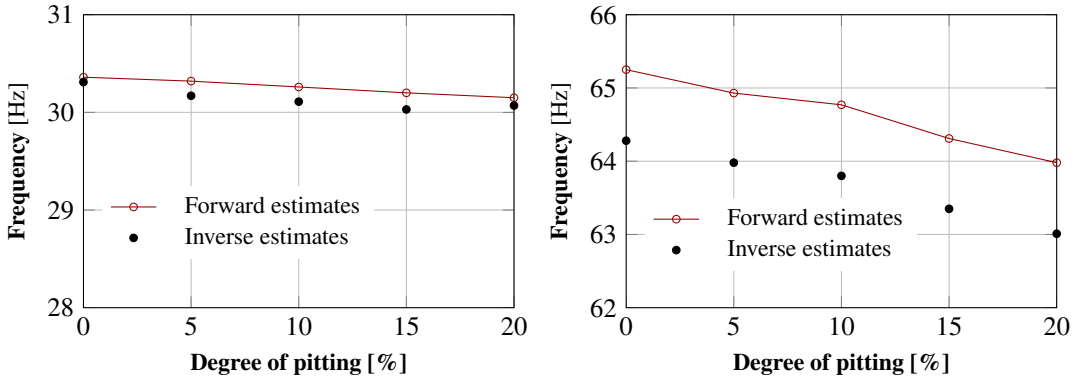

(a) First natural frequency

(b) Ninth natural frequency

Figure 5.18: Estimated natural frequencies with pitting corrosion on the plate

In Figs. 5.18(a) and 5.18(b) the change of the first and ninth natural frequency with respect to four degrees of pitting are presented. While for the first mode it is evident that the frequency reduction cannot be identified with certainty, the results regarding the ninth natural frequency seem to be slightly better. However, a closer view of the values of the identified

frequencies, which are summarized in Table 5.5, is sufficient to show that even the most influenced frequency of the ninth mode can be fairly identified. Considering that the accuracy of the implemented algorithm was estimated to be around 1.50% and the maximum identified frequency change is 1.98%, it can be deduced on one hand that pitting corrosion is impossible to be identified for DOP up to 15% while, on the other hand, it cannot be safely said that it is identifiable for 20% DOP.

Mode no.	$\hat{f}_k$ [Hz]							
	Reference model	5% DOP		10% DOP		15% DOP		20% DOP	
1	30.31	30.17	(0.46)	30.11	(0.66)	30.03	(0.92)	30.07	(0.79)
2	30.42	30.43	(0.03)	30.38	(0.13)	30.41	(0.03)	30.41	(0.03)
3	30.86	30.86	(0.00)	30.83	(0.10)	30.85	(0.03)	30.84	(0.03)
4	31.22	31.22	(0.00)	31.19	(0.10)	31.22	(0.00)	31.18	(0.13)
5	31.62	31.61	(0.03)	31.50	(0.38)	31.54	(0.25)	31.51	(0.35)
6	32.04	32.03	(0.03)	31.99	(0.16)	31.94	(0.31)	31.71	(1.03)
7	32.41	32.38	(0.09)	32.34	(0.22)	32.19	(0.68)	32.21	(0.62)
8	32.49	32.41	(0.25)	32.40	(0.28)	32.43	(0.18)	32.47	(0.06)
9	64.28	63.98	(0.47)	63.80	(0.75)	63.35	(1.45)	63.01	(1.98)
10	65.96	65.73	(0.35)	65.58	(0.58)	65.21	(1.14)	65.04	(1.39)

Table 5.4: Natural frequency estimates of the stiffened panel with pitting corrosion on the plate

As underlined in Chapter 4, the degradation due to pitting corrosion consists of localized changes in the structural properties of the panel which would be mostly visible in higher order modes. It is for this reason that the largest changes in the natural frequencies occur in modes 9 and 10. Although it would be possible to extend the modal basis with higher modes, so that identifiability is ensured, it is unlikely the these will be excited under real operational conditions, given their significantly high natural frequencies.

5.4.3 Fatigue cracks

Unlike the previous scenarios, where the mode shapes of the damaged models remained constant and the damage identification had to be performed only in terms of natural frequencies, the damaged scenarios with fatigue crack have the advantage of ”new” mode shapes. This

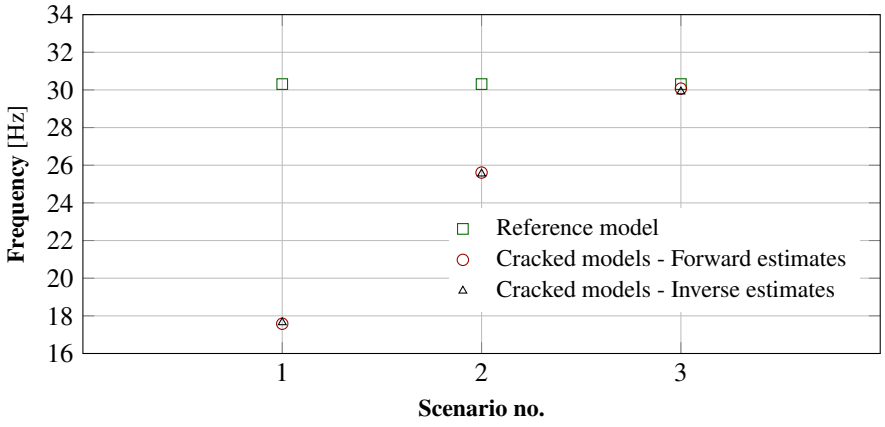

Figure 5.19: Estimated natural frequencies for the first mode of the cracked models

enables the identification in terms of mode shapes even if the changes in natural frequencies are smaller than the accuracy of the SSI algorithms. Considering that all three damaged models have a new first mode, the existence of cracks can be merely identified through this mode. The identified and calculated frequency of the first mode for each one of the models is plotted in Fig. 5.19 along with the corresponding frequency of the reference model.

Mode no.	$\hat{f}_k$ [Hz]			
	Reference model	1st Scenario	2nd Scenario	3rd Scenario
1	30.31	17.61	25.55	29.91
2	30.42	30.31	30.36	30.39
3	30.86	30.80	30.83	30.83
4	31.22	31.19	31.21	31.20
5	31.62	31.61	31.49	31.38
6	32.04	31.87	31.94	31.65
7	32.41	32.03	32.32	32.14
8	32.49	32.39	32.48	32.51
9	64.28	32.81	57.75	63.81
10	65.96	64.50	65.07	65.71

Table 5.5: Natural frequency estimates of the stiffened panel with fatigue cracks

The values of the identified frequencies are summarized in Table 5.5 for all three scenarios as well as for the reference model. The new modes are marked with gray and the values below them are shifted. Hence, the second frequency of the damaged models should be compared with the first frequency of the reference model and so forth. Although for the first and second scenario the frequency change of the first mode is evidently detected (Fig. 5.19), for the third scenario the corresponding change is not equally visible. Without knowing that the first frequency of the third crack scenario refers to a different mode than the first one of the reference model, one could easily attribute the small change of 1.32% (from 30.31 Hz to 29.91 Hz) to the margin of error of the SSI algorithm.

The existence of new modes in the models with fatigue crack may be identified using the MAC between the mode shapes of the reference model and those of the damaged ones, obtained from Eq. (3.75). Once the MAC matrix between two modal bases is constructed,

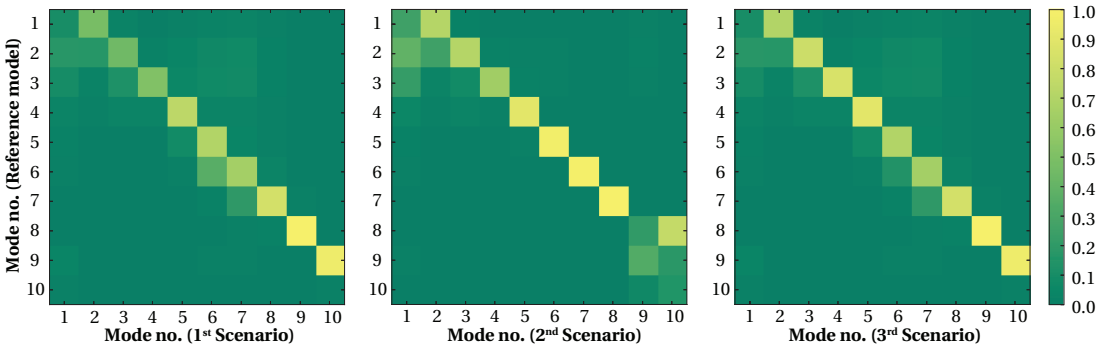

(a) 1st Scenario (b) 2nd Scenario (c) 3rd Scenario

Figure 5.20: MAC matrices between mode shapes of the reference model and the models with crack

one can easily examine the correspondence between different modes. When two modes are identical, the MAC between their mode shapes will be one while it will be zero for independent mode shapes. The MAC matrices between the mode shapes of the reference model and the models with crack are graphically presented in Fig. 5.20.

In Fig. 5.20(a) is seen that the first mode shape of the first cracked scenario does not show any correspondence with the identified mode shapes of the reference model and hence it represents a new mode. Although the remaining modes seem to be slightly influenced by the crack, all of them show a certain correspondence with those of the reference model. In Fig. 5.20(b), apart from the first mode, mode eight is also a new one since it does not seem to be strongly correlated with any of the others. Finally, the crack of the 3rd scenario that was not clearly identified through the frequency changes may be detected in terms of mode shapes. It is observed in Fig. 5.20(c) that there is not full correspondence between the two models since the first mode of the cracked model is a new one.

6 Conclusions and Future Work

In this Chapter, an overview of the work carried out within the framework of the present thesis is presented. This is accomplished through the evaluation of the addressed objectives, as cited in Chapter 1, in accordance with the results obtained in Chapters 4 and 5. Moreover, a critical assessment of the adopted formulation is presented with emphasis on recommendations for future work and enrichment of this study.

6.1 Conclusions

The work presented in this thesis may be divided into two parts, the so-called forward and inverse problems. In the former, the modelling of degradation mechanisms experienced by hull structures of FPSOs, namely uniform corrosion, pitting corrosion and fatigue cracks, was carried out. These mechanisms were introduced in the reference FE model of a typical stiffened panel and the sensitivity of its dynamic properties, i.e. natural frequencies, mode shapes and damping ratios, to these changes was investigated. In the second part, the stiffened panel was studied during normal operation, while excited by sloshing-induced impulsive loads. The response was measured by a fictitious monitoring system of accelerometers and the noisy signals were used for OMA with two different SSI algorithms. To enable automatic system identification, the entire scheme was enhanced with cluster analysis and the identified dynamic properties for each one of the damaged models were compared with those of the reference model. The conclusions drawn from these results may be summarized in the following points:

i. Applicability of OMA

   Even though the considered stiffened panel was studied locally as a small structural component of an entire vessel, it was shown that OMA for the identification of dynamic properties using SSI algorithms may yield sufficiently accurate results in terms of natural frequencies and mode shapes as well. Moreover, combination of the SSI schemes with a cluster analysis may serve as an efficient tool for automatic system identification.

ii. Weak points

   The implementation of SSI algorithms is subject to certain limitations. Although it was shown that the number of sensors and the noise level may be properly chosen in order to achieve robust results, this will not be feasible in real applications. Considering that any prior knowledge of both the noise level and the system as such is characterized by a

large degree of uncertainty, such limitations are usually masked in output-only systems and the OMA may become inefficient.

iii. Damage identification

It was shown that localized and low-degree degradation mechanisms are impossible to be identified since their influence on modal properties may be equally attributed either to the existence of noise or to the accuracy of the algorithms. These damage conditions are mainly reflected in high-order modes which usually do not contribute in the global response and therefore are not observable. On the other hand, it is seen that global damage states and long-term degradation patterns, that involve high degree of damage, can be identified through a small modal basis consisting of the first few modes. This of course implies that deterioration is not detectable from the very first moment but only after a sufficiently advanced stage.

6.2 Future research

The aforementioned conclusions with respect to the obtained results and the feasibility of vibration-based structural health monitoring on FPSOs are drawn on the basis of a set of assumptions. It should be therefore remarked that the present study does not only constitute a first approach on the damage detection monitoring on FPSO hull-structures but it also gives rise to further investigation topics, which may possibly mask the sought for damage identification, towards a more integrated study. Hence, the proposed research directions according to the adopted framework of assumptions can be summarized in the following points:

Boundary conditions

Within the current formulation, the examined stiffened panel was considered to be fully clamped at the edges with fixed boundary conditions applied in the FE model. A detailed explanation of this choice is provided in Chapter 4 where it is also underlined that such an assumption does not reflect the real boundary conditions since the panel is simulated as a standalone part. Taking into account that the assumed conditions at the boundaries have a significant impact on the dynamic properties of the model and subsequently on the sensitivity analysis as well as on the operational modal analysis, it is of crucial importance that further investigation is carried out in this direction. To this end, a more accurate representation of the boundaries may be obtained by the integration of the panel into the numerical model of the entire FPSO or even by the simulation of a broader hull-structure area so that contribution of the adjacent structural members is properly accounted for. Alternatively, the boundary conditions of the already modelled panel may be calibrated through the use of appropriately chosen measurements on existing stiffened panels, in order to yield a more accurate approximation.

Added mass effect

The entire study in terms of both the forward and the inverse problem was based on the dynamic properties of the stiffened panel neglecting the presence of water in the ballast tank. This of course implies that the coupled motion between the panel and the water is not accounted for and therefore the participation of the additional vibrating mass of the liquid is ignored. However, such an effect may have a significant contribution in the modal properties of the structure by substantially reducing the natural frequencies

and changing the vibration modes. Moreover, the said contribution will result in a time-varying system since the dynamic characteristics will be dependent on the amount of water mass and subsequently on the fill level of the ballast tank. In this sense, with increasing amount of added mass, the natural frequencies of the coupled system will decrease, thus getting closer to the operational frequency range of excitation.

Sloshing-induced loads

A special case of environmental sloshing-induced excitation was examined in the framework of the OMA. It was namely assumed that impulsive pressure was applied on the walls of the panel, which appears for low fill level of ballast tanks. Such a loading case though constitutes an ideal scenario given that the calculated dry natural frequencies are significantly higher than the usual frequency range of environmental loads. In this sense, the assumed impact loads are used in favour of the identification process providing excitation of all modes, which may not be the case in real operational conditions. It is therefore of high prominence to enhance the proposed methodology with a more sophisticated modelling of sloshing loads towards a higher reliability level of the monitoring scheme. Moreover, it should be underlined that in operational conditions, ballast tanks are usually filled at high levels and therefore, excitation by low-frequency harmonics should be examined in combination with wet modal properties, as indicated in the previous point.

Global hull loads

The last but not least parameter that will play a major role in a more profound study on the vibration-based monitoring of FPSO is the influence of the global hull loads on the dynamic properties of stiffened panels. In the present project, the possible in-plane loads on the stiffened panel due to the global hull response of the structure were not taken into account. However, depending on the position of the panel along the height of the FPSO and the operational conditions, the structure will be subject to an in-plane tensile or compressive stress state as well. This tension, or compression, will in turn increase, or accordingly decrease, the natural frequencies of the panel and will thus violate the assumption of a time-invariant system. It is hence of critical importance that such an effect is appropriately considered within a real monitoring scheme, not only due to the global static loads but also with regard to the global dynamic behaviour.

Bibliography

Aalberts, P., van der Cammen, J., and Kaminski, M. L. (2010). The MonitAS system for the *Glas Dowr* FPSO. In *Offshore Technology Conference*.

Akpan, U. O., Koko, T. S., Ayyub, B., and Dunbar, T. E. (2002). Risk assessment of aging ship hull structures in the presence of corrosion and fatigue. *Marine Structures*, 15:211–231.

Alinia, M. M., Hosseinzadech, S. A. A., and Habashi, H. R. (2007). Numerical modelling for buckling analysis of cracked shear panels. *Thin-Walled Structures*, 45:1058–1067.

American Bureau of Shipping (2006). Strength assessment of membrane-type LNG carriers. *Guidance Notes*.

ANSYS (2013). *ANSYS Workbench Verification Manual*. ANSYS.

Bathe, K. J. (1996). *Finite Element Procedures in Engineering Analysis*. Prentice Hall.

Boller, C., Chang, F. K., and Fujino, Y. (2009). *Encyclopedia of structural health monitoring*. John Wiley and Sons.

Brincker, R., Zhang, L., and Andersen, P. (2001). Modal identification of output-only systems using frequency domain decomposition. *Smart Materials and Structures*, 10:441–445.

Chopra, A. K. (2012). *Dynamics of structures - Theory and applications to earthquake engineering*. Prentice Hall.

Daidola, J. C., Parente, J., Orisamolu, I. R., and Ma, K. T. (1997). Residual strength assessment of pitted plate panels. Technical report, Ship Structure Committee Report SSC-394.

DNV (2006). Sloshing analysis of LNG membrane tanks. *Classification Notes - No. 30.9*.

DNV (2013). Allowable thickness diminution for hull structure. *Classification Notes - No. 72.1*.

DNV (2014). Fatigue assessment of ship structures. *Classification Notes - No. 30.7*.

Dunbar, T. E., Pegg, N., Taheri, F., and Jiang, L. (2004). A computational investigation of the effects of localized corrosion on plates and stiffened panels. *Marine Structures*, 17:385–402.

Gardiner, C. P. and Melchers, R. E. (2003). Corrosion analysis of bulk carriers, Part 1: operational parameters influencing corrosion rates. *Marine Structures*, 16:547–566.

Hageman, R., Aalberts, P., Shaik, M., and van den Boom, H. (2013). Development of an advisory hull fatigue monitoring system. Technical report, MARIN.

Hair, J., Anderson, R., Tatham, R., and Black, W. (1998). *Multivariate Data Analysis*. Prentice Hall.

Hostis, D. L., van der Cammen, J., Hageman, R., and Aalberts, P. (2013). Overview of the MonitAS II project. In *Proceedings of the 23rd International Offshore and Polar Engineering*.

Howarth, D. J. (2011). Corrosion: its impact on modern shipping with particular reference to crude oil tankers. *Lloyd's Register Technology Days*.

Huang, Y., Zhang, Y., Liu, G., and Zhang, Q. (2010). Ultimate strength assessment of hull structural plate with pitting corrosion damnification under biaxial compression. *Ocean Engineering*, 37:1503–1512.

Ibrahim, R. A. (2005). *Liquid Sloshing Dynamics - Theory and Applications*. Cambridge University Press.

ISSC (2009). Report of Specialist Committee III.1 Ultimate strength. *Proceedings of the 17th International Ship and Offshore Structures Congress*, pages 375–474.

Kim, S. Y., Ahm, Y., Kim, K. H., and Kim, Y. (2013). Experimental studies on sloshing in a STX independence type-B tank. In *Proceedings of the Twenty-third International Offshore and Polar Engineering*.

Lloyd's Register (2004). Sloshing Loads and Scantling Assessment. *Prodedures Manual*.

Lloyd's Register (2009). Sloshing assessment for membrane tank LNG operations. *Guidance Document*.

Magalhaes, F. and Cunha, A. (2011). Explaining operational modal analysis with data from an arch bridge. *Mechanical Systems and Signal Processing*, 25:1431–1450.

Melchers, R. E. (2005). The effect of corrosion on the structural reliability of steel offshore structures. *Corrosion Science*, 47:2391–2410.

Nakai, T., Matsushita, H., Yamamoto, N., and Arai, H. (2004). Effect of pitting corrosion on local strength of hold frames of bulk carriers. *Marine Structures*, 17:403–432.

Okawa, T., Sumi, Y., and Mohri, M. (2006). Simulation-based fatigue crack management of ship structural details applied to longitudinal and transverse connections. *Marine Structures*, 19:217–240.

Paik, J. K. and Kim, B. J. (2002). Ultimate strength formulations for stiffened panels under combined axial load, in-plane bending and lateral pressure: a benchmark study. *Thin Walled Structures*, 40:45–83.

Paik, J. K., Kumar, Y. V. S., and Lee, J. M. (2005). Ultimate strength of cracked plate elements under axial compression or tension. *Thin-Walled Structures*, 43:237–272.

Paik, J. K., Lee, J. M., and Ko, M. J. (2003). Ultimate compressive strength of plate elements with pit corrosion wastage. *Journal Engineering for the Maritime Environment*, 217:185–200.

Paik, J. K. and Thayamballi, A. K. (2002). Ultimate strength of ageing ships. *Journal Engineering for the Maritime Environment*, 216:57–7.

Peeters, B. (2000). *System identification and damage detection in civil engineering*. PhD thesis, Katholieke Universiteit Leuven, Belgium.

Qian, G. L., Gu, S. N., and Jiang, J. S. (1991). A finite element model of cracked plates and application to vibration problems. *Computers & Structures*, 39:483–487.

Qin, H., W., Z., and Zhang, S. (2015). Bayesian inferences of generation and growth of corrosion defects on energy pipelines based on imperfect inspection data. *Reliability Engineering and System Safety*, 144:334–342.

Qin, S. and Cui, W. (2003). Effect of corrosion models on the time dependent reliability of steel plated elements. *Marine Structures*, 16:15–34.

Qu, Z. Q. (2004). *Model order reduction techniques with applications in finite element analysis*. Springer.

Reynders, E., Pintelon, R., and De Roeck, G. (2008). Uncertainty bounds on modal parameters obtained from stochastic subspace identification. *Mechanical Systems and Signal Processing*, 22:948–969.

Silva, J. E., Garbatov, Y., and Soares, C. G. (2014). Reliability assessment of a steel plate subject to distributed and localized corrosion wastage. *Engineering Structures*, 59:13–20.

Stahl, B. and Keer, L. M. (1972). Vibration and stability of cracked rectangular plates. *International Journal of Solids and Structures*, 8:69–91.

Sultana, S., Wang, Y., Sobey, A. J., Wharton, J. A., and Shenoi, R. A. (2015). Influence of corrosion on the ultimate compressive strength of steel plates. *Thin-Walled Structures*, 96:95–104.

Tran, L. V., Ly, H. A., Lee, J., Wahab, M. A., and Nguyen-Xuan, H. (2015). Vibration analysis of cracked FMG plates using higher-order shear deformation theory and extended isogeometric approach. *International Journal of Mechanical Sciences*, 96-97:65–78.

Vafai, A. and Estekanchi, H. E. (1999). A parametric finite element study of cracked plates and shells. *Thin-Walled Structures*, 33:211–229.

Van Overschee, P. and De Moore, B. (1996). *Subspace Identification for Linear Systems: Theory - Implementation - Applications*. Dordrecht, Netherlands: Kluwer Academic Publishers.

Wang, F., Paik, J. K., Kim, B., Cui, W., and Hayat, T. (2015a). Ultimate shear strength of intact and cracked stiffened stiffened panels. *Thin-Walled Structures*, 88:48–57.

Wang, M. L., Lynch, J. P., and Sohn, H. (2014a). *Sensor Technologies for Civil Infrastructures*, volume 1: Sensing Hardware and Data Collection Methods for Performance Assessment. Woodhead Publishing.

Wang, M. L., Lynch, J. P., and Sohn, H. (2014b). *Sensor Technologies for Civil Infrastructures*, volume 2: Applications in Structural Health Monitoring. Woodhead Publishing.

Wang, Y., Wharton, J. A., and Shenoi, R. A. (2014c). Ultimate strength analysis of aged steel-plated structures exposed to marine corrosion damage: A review. *Corrosion Science*, 86:42–60.

Wang, Y., Wharton, J. A., and Shenoi, R. A. (2015b). Ultimate strength assessment of steel stiffened plate structures with grooving corrosion damage. *Engineering Structures*, 94:29–42.

Yamamoto, N. and Ikegami, K. (1998). A study on the degradation of coating and corrosion of ship's hull based on the probabilistic approach. *Journal of Offshore Mechanics and Arctic Engineering*, 120:121–128.

Yang, L. (2008). *Techniques for corrosion monitoring*. Woodhead Publishing.

Zhang, L., Brincker, R., and Andersen, P. (2005). An overview of operational modal analysis: Major developments and issues. *Proceedings of the 1st International Operational Modal Analysis Conference,*, pages 179–190.